Engineering Non-Precious Group Metal Electrode for PEMFCs with Enhanced Mass Transport via the Electrospraying Technique

by

Yongwook Kim

A thesis

presented to the University of Waterloo

in fulfillment of the

thesis requirement for the degree of

Doctor of Philosophy

in

Chemical Engineering

Waterloo, Ontario, Canada, 2020

Examining Committee Membership

The following served on the Examining Committee Membership for this thesis. The decision of the Examining Committee is by majority vote.

External Examiner	Prof. Andy (Xueliang) Sun Department of Mechanical and Materials Engineering, Western University
Supervisor	Prof. Jeff T. Gostick Department of Chemical Engineering, University of Waterloo
Internal Member	Prof. Marios Ioannidis Department of Chemical Engineering, University of Waterloo
Internal Member	Prof. Aiping Yu Department of Chemical Engineering, University of Waterloo
Internal-external Member	Prof. Eric Prouzet Department of Chemistry, University of Waterloo

Author's Declaration

This thesis consists of material all of which I authored or co-authored: see Statement of Contributions included in the thesis. This is a true copy of the thesis, including any required final revisions, as accepted by my examiners.

I understand that my thesis may be made electronically available to the public.

Statement of Contributions

The body of this thesis is based upon a combination of manuscripts prepared for publication. Various chapters are adapted from the following list of publications or manuscripts.

Chapter 3 of this thesis consists of the following manuscript in preparation.

> Kim, Y., Secanell, M., Gostick, J.T., "Numerical Simulation of PEMFC Performance to Determine Optimal Composition for Non-PGM Catalyst Layers"

Y. Kim designed the parametric study for electrode optimization. Y. Kim performed the entire simulation as well as the analysis of the simulated data. The first draft was prepared by Y. Kim. M. Secanell provided significant help in running the simulation as well as analyzing the data. J. T. Gostick provided aid in planning the research and oversaw the project. All authors participated in reviewing the results and editing the manuscript.

Chapter 4 of this thesis consists of the following published work, which was authored by myself and my supervisor, J. T. Gostick.

> Kim, Y., Gostick, J.T., "Measuring Effective Diffusivity in Porous Media with a Gasket-free Radial Arrangement" *Int. J. Heat Mass Transf.* 129 (2019) 1023-1030

The entire work was done by Y. Kim from designing and building the radial diffusion apparatus to collecting and analyzing the experimental data under the supervision of J. T. Gostick. The draft of the manuscript was prepared by Y. Kim. J. T. Gostick reviewed the results and edited the manuscript.

Chapter 5 of this thesis consists of the following collaborative work submitted for publication.

Kim, Y., Asset, T., Wei, F., Atanassov, P., Secanell, M., Barralet, J., Gostick, J.T., "Fabrication of PGM-free Catalyst Layer with Enhanced Mass Transport Characteristics via Electrospraying Technique" *Under Review*

Y. Kim designed, built and established protocols for the electrospray apparatus used in this work. Y. Kim planned the experiment and prepared the entire non-PGM electrode samples. Y. Kim also performed all characterizations except the porosimetry. The data analysis was also performed by Y. Kim. The draft of the manuscript was prepared by Y. Kim. T. Asset synthesized the non-PGM catalyst used in this work and provided significant help in understanding the nature of the non-PGM catalyst. F. Wei performed the porosimetry on all samples as well as the data smoothing of the capillary pressure curves and the pore size distributions. J. T. Gostick, M. Secanell, P. Atanassov, and J. Barralet provided aid in planning the research and oversaw the project. All authors participated in reviewing the results and editing the manuscript.

J. T. Gostick was the principal investigator of all the research projects presented in the thesis, and he was involved in every aspect of all works.

Abstract

Ever since the concept of "Hydrogen Economy" emerged, fuel cell technology has been regarded as the key component of the clean, sustainable energy future. Thanks to great successes in the development of fuel cell technology in recent years, they are now transitioning from R&D stage to the commercial stage. Some of the major automotive companies such as Toyota and Honda have already commercialized the fuel cell vehicles. Recently fuel cell technology has emerged as an appealing technology in heavy-duty automotive industry due to its high-power output, fast fuel charge, long driving range and light weight. Currently, most commercialized fuel cell stacks either use Pt/C or Pt-alloy catalysts which makes up as much as 40% of the stack production cost. It is clear that for further market penetration the stack cost needs to be reduced by using less or no platinum.

Recent advances in non-Precious Group Metal (non-PGM) catalysts have provided hopes to completely remove the expensive Pt from the stack. There has been great progress in the development of non-PGM catalysts, but they are still less catalytically active than Pt, and to compensate for low catalytic activity, higher catalyst loading is required resulting in much thicker electrodes. Thicker electrodes suffer from increased transport resistances, so careful design of the electrode is required to further improve the performance of the non-PGM materials. This thesis aims to address this issue by providing insights on how to engineer the non-PGM electrode. The work was carried out in three stages. First, the optimal composition of the non-PGM cathode was investigated using a single-phase, non-isothermal model. A comprehensive parametric study of catalyst loading, Nafion™ loading and thickness was carried out under realistic fuel cell operating conditions. This study revealed that the optimum catalyst loading was about $3.0 - 4.0\ \mathrm{mg/cm^2}$ whereas 70% Nafion™ was found to be the optimum.

In the second stage, due to lack of available tool to characterize the mass transport characteristics of thin porous materials, such as the catalyst layers, a novel method was developed which requires no gasket making it appealing to thin catalyst layers. The method was thoroughly validated with open air and some of the traditional porous media. In the final stage, the non-PGM catalyst layers were fabricated, and their structural properties were analyzed. Properties such as pore size distribution, specific surface area and porosity were determined as well as the tortuosity using the novel method developed herein. Generally, electrosprayed non-PGM catalyst layers showed vastly improved mass transport characteristics owing to high porosity as well as increased average pore size. An empirical tortuosity-porosity relationship was also derived for electrosprayed non-PGM catalysts which would be valuable in the future modeling studies.

Acknowledgements

I must first thank my supervisor Prof. Jeff Gostick. He has provided me with a great deal of support over the past 4 years. He has given me a complete freedom and autonomy on how I carried out my work and helped me shape my own style of research. He never forgot to visit the lab every now and then to cheer me up and to buy me drinks when things weren't going very smoothly. I hope to inherit your management style one day. I should also thank him for introducing me to the world of porous media. I am truly grateful to have been working in the field and I really love it! I hope I have made some contribution to your ambition of building an empire of porous media. Jeff has also helped me and my family personally, making sure that the transition from the other side of the world to Montréal, then to Waterloo went smoothly. Driving back and forth between Montréal and Waterloo a few times was actually fun. He also made a personal visit to my place when my first child, Liam, was born. It meant a lot to us and we are truly grateful for that.

At first, I was a little unsure of moving from Montréal to Waterloo, but it turned out to be a great choice, being introduced to many great people. First, I must thank Prof. Marc Secanell for pretty much acting as a co-supervisor in the final year of my Ph.D. His inputs to my work have been invaluable and his unlimited knowledge in fuel cell have helped me shape my thesis. I also must thank Prof. Plamen Atanassov for providing me his catalyst without which I literally could not have written this thesis.

I greatly appreciate the efforts of my committee members Prof. Marios Ioannidis, Prof. Aiping Yu, Prof. Eric Prouzet and Prof. Andy Sun, who offered their valuable time to criticize my work and helped me produce the best possible results.

I am also very thankful to my collaborators Tristan Asset and Fei Wei. Tristan has been a great collaborator providing me with catalysts on a timely manner even when he was busy moving from New Mexico to California at the end of the year. He has also offered me with prompt responses to the questions I had about his catalyst. I thank Fei for providing me with his expertise in mercury porosimetry which is very hard to get these days. I have maybe performed a handful of Hg porosimetry and I know how annoying it can be to do just one test, dealing with greasy hydraulic oil and toxic Hg. I really appreciate your hard work.

I would also like to thank my past and present lab/officemates for occasional chats and treats –

Tom Tranter, Guobin Wen, Shashi Yadav, Awais Murtaza, Zohaib Khan, Mehrez Agnaou, Zak Brookshaw, Niloo Misaghian, Kyu-min Lee and Ellsworth Bell. I would like to especially thank Ellsworth for providing help in my lab work and making the lab work enjoyable. It was a lonely lab for a long time, and he was pretty much the first one in my Ph.D. to stay in the lab for longer period.

I greatly appreciate my friends outside of the lab Moongyu Park, Jungeun Um, Seyoung Kim and Kernho Park. Talking to you in my native language during lunch/coffee break was a stress-reliever.

I would also like to thank my parents who believed in me and supported me financially and psychologically during my Ph.D. I know I spent too much time in the post-secondary education, but it's finally near the end!

I also wish to thank my little ones, Liam and Lielle, for making my Ph.D. so much harder, yet happier. Liam, you came to us as a surprise while we were still in Montreal. We were mentally, physically and financially not prepared to be parents at all, but you have grown up so well over the past 3 years. I am so proud of you. Lielle, you came to us a little earlier than we expected, and I am really sorry I couldn't provide more care for you as I am swamped with preparing this thesis. Your innocent baby smile makes all of my stress go away. You guys are crying and bothering me even as I'm writing this thesis, but I still love you guys. You guys are the second greatest thing that happened to me.

Last but foremost, I cannot thank my wife, Gyu-mi, enough who married me and came to Canada with me so I can pursue my degree. It must have been a hard decision to quit high paying job as a materials scientist to come to a foreign country where she had a very little to no knowledge of. Yet, she said "yes" without any hesitation. To me, you are the largest contributor to all the works I have done. I could not have finished my Ph.D. without your support and your sacrifice. Thank you for believing in me. I owe you my life and you own everything I will accomplish in the future.

사랑하는 나의 가족 규미, 리엄, 리엘에게…

To my lovely family, Gyu-mi, Liam and Lielle

Table of Contents

Examining Committee Membership .... **ii**
Author's Declaration .... **iii**
Statement of Contributions .... **iv**
Abstract .... **vi**
Acknowledgements .... **viii**
List of Figures .... **xiv**
List of Tables .... **xix**
List of Abbreviations .... **xx**
List of Symbols .... **xxii**
Chapter 1 Introduction **1**
- 1.1. Motivation 1
- 1.2. Outline of the Thesis 4

Chapter 2 Background and Literature Review **5**
- 2.1. Overview of Fuel Cell 5
  - 2.1.1. Fuel Cell Operation 5
  - 2.1.2. Fuel Cell Performance 7
- 2.2. Catalyst Layers 11
  - 2.2.1. Overview of Non-PGM Catalyst Layer Developments 13
  - 2.2.2. Mass Transport in Fuel Cell Catalyst Layers 16
- 2.3. Electrospraying 26
  - 2.3.1. Physics of Electrospraying 26
  - 2.3.2. Application in Fuel Cell Catalyst Layers 29

Chapter 3 Numerical Simulation of PEMFC Performance to Determine Optimal Composition for Non-PGM Catalyst Layers **32**
- 3.1. Preface 32
- 3.2. Abstract 32
- 3.3. Introduction 33
- 3.4. Model Description 36

3.4.1. Assumptions 37
3.4.2. Governing equations 38
3.4.3. Boundary conditions and model parameters 41
3.4.4. Parametric study 42
3.5. Results and Discussion 44
3.5.1. Case Study 1: Constant V_{FeNC} 44
3.5.2. Case Study 2: Variable V_{FeNC} 51
3.6. Conclusion 58

Chapter 4 Measuring Effective Diffusivity in Porous Media with a Gasket-free Radial Arrangement 60

4.1. Preface 60
4.2. Abstract 60
4.3. Introduction 61
4.4. Experimental Methods 63
4.4.1. Diffusion Pedestals 64
4.4.2. System Setup and Test Procedure 65
4.4.3. Data Analysis 66
4.4.4. Sample Preparation 68
4.4.5. Porosity Measurement 70
4.4.6. Validation with Open Air 71
4.5. Results and Discussion 74
4.6. Conclusion 78

Chapter 5 Fabrication of PGM-free Catalyst Layer with Enhanced Mass Transport Characteristics via Electrospraying Technique 81

5.1. Preface 81
5.2. Abstract 81
5.3. Introduction 82
5.4. Experimental 85
5.4.1. Material Production 85
5.4.2. Electrode Characterization 88
5.5. Results and Analysis 92

- 5.5.1. Morphology, Thickness and Porosity 92
- 5.5.2. Pore Size Distribution 97
- 5.5.3. Specific Surface Area 99
- 5.5.4. Effective Diffusivity 100
- 5.5.5. Tortuosity 102

5.6. Conclusion 106

Chapter 6 Concluding Remarks 108

6.1. Summary 108

6.2. Future works 110

- 6.2.1. Through-plane Effective Diffusivity/Tortuosity 110
- 6.2.2. Measurement of Other Effective Properties 110
- 6.2.3. Hydrophobic Non-PGM Electrode 111
- 6.2.4. Non-PGM Performance Test under Lower Relative Humidity 111

References 112

Appendix 125

List of Figures

Figure 1-1 “Hydrogen Economy” described by H2@Scale concept.[2] 1

Figure 2-1 (a) Galvanic cell representation of PEMFC and a brief description of the transport processes occurring inside (b) Typical components of a gas diffusion electrode (GDE) and their images 6

Figure 2-2 A summary of major losses in fuel cell performance. From left to right: theoretical reversible voltage, activation overpotential, ohmic overpotential, concentration overpotential and finally the net polarization curve 8

Figure 2-3 Typical catalyst layer structure and transport challenges. Note, for conventional Pt/C catalyst, active site = platinum and catalyst body = carbon black. 11

Figure 2-4 Comparison of performances between 0.1 $\mathrm{mg_{pt}/cm^2}$ loading Pt/C catalyst layer (black) and non-PGM catalyst layers at 4 $\mathrm{mg_{cat}/cm^2}$ loading with two different Nafion™ loadings – 35% (blue) and 50% (red). All tests performed under air.[28] 14

Figure 2-5 Illustration of different species interaction mechanisms. (a) particle-particle (molecular) interaction (b) particle-wall (Knudsen) interaction 17

Figure 2-6 Tortuous diffusion pathway adds resistance to transport of a gas molecule 21

Figure 2-7 Several forces acting on liquid jet at cone-jet mode 27

Figure 2-8 Electrospraying mechanism (assuming positive potential at the needle tip). 28

Figure 3-1 Schematic of the model domain and relevant species transport (a) 3D isometric view (b) 2D cross-sectional view 36

Figure 3-2 Case 1: constant V_{FeNC} – linear increase in the catalyst loading with the increasing thickness 43

Figure 3-3 Case 2: variable V_{FeNC} – exponentially increasing catalyst loading per unit volume with decreasing thickness at the same catalyst loading per unit area..................................44

Figure 3-4 Power density at various catalyst and Nafion™ loadings at $V_{cell} = 0.76$ V (a) 2-D visualization (b) effect of Nafion™ loading on the performance (c) effect of catalyst loading on the performance..45

Figure 3-5 Power density at various catalyst and Nafion™ loadings at $V_{cell} = 0.60$ V (a) 2-D visualization (b) effect of Nafion™ loading on the performance (c) effect of catalyst loading on the performance..47

Figure 3-6 Polarization curves at various ink compositions: (a) Catalyst loading fixed at $4.0\ \mathrm{mg/cm^2}$. Nafion™ loading varied from 0.20 to 0.75 (b) Catalyst loading varied from 3.0 to $5.0\ \mathrm{mg/cm^2}$. Nafion™ loading fixed at 0.70. The dashed lines represent where the maximum relative humidity is > 100% 50

Figure 3-7 2-D visualization of power density with respect to the CL thickness and Nafion™ loading at fixed catalyst loading per unit volume at 0.76 V. Black pixels at low thickness region represents the area where the porosity drops below 0. 52

Figure 3-8 Maximum power density at each catalyst loading (0.76 V)....................................53

Figure 3-9 2-D visualization of power density with respect to the CL thickness and Nafion™ loading at fixed catalyst loading per unit volume at 0.60 V. Black pixels at low thickness region represents the area where the porosity drops below 0. 54

Figure 3-10 Maximum power density at each catalyst loading (0.60 V)..................................55

Figure 3-11 Scatter plot of power density with respect to porosity and ionomer volume fraction (a) at 0.76 V and (b) at 0.60 V. 56

Figure 3-12 Power densities plotted against (a) porosity at 0.76 V, (b) Nafion™ volume fraction at 0.76 V (c) porosity at 0.60 V and (d) Nafion™ volume fraction at 0.60 V. Dashed lines were placed near the maximum power density for each plot...57

Figure 4-1 (left) Pedestal design for radial diffusivity apparatus (right) Radial diffusivity apparatus system setup 64

Figure 4-2 The analytical solution of Fick’s second law fitted to transient oxygen concentration profile of an open air 67

Figure 4-3 SEM Images of (a) 0.1 mm glass beads, (b) 1 mm stainless steel balls, (c) 25 µm spherical SiO_2, (d) 3.5-15 µm Al_2O_3, (e) 0.3-0.8 µm Al_2O_3, (f) quartz frits with pore size 200 – 300 µm, (g) quartz frits with pore size 40 – 90 µm, (h) quartz frits with pore size 4 – 15 µm..69

Figure 4-4 Diffusion coefficient of N_2-Air binary system measured with various gap distances (left) and various volumetric flow rates (right). The line indicates the prediction of the Chapman-Enskog equation given in Eq. [4-10]..72

Figure 4-5 Illustration on justification of the constant boundary condition................................74

Figure 4-6 Relative diffusivity (left) and tortuosity (right) of porous media and comparison to the theoretical correlations. (Each data point is an average of three measurements. Error bar omitted for clarity)..75

Figure 4-7 Comparison of the relative diffusivity (left) and the tortuosity (right) between Currie[153] and the present study (m = 1.5) 76

Figure 4-8 Pore size distributions of 0.3-0.8 µm Al_2O_3 packing (green) and 3.5-15 µm Al_2O_3 packing (red) 78

Figure 5-1 Schematic diagram of electrospraying setup. The setup includes 1) a syringe pump, 2) high voltage power supply and 3) XY moving stage...86

Figure 5-2 SEM images of electrosprayed non-PGM catalyst layers (a) Q50D30 (b) Q50D50 (c)

Q50D70 (d) Q75D30 (e) Q75D50 (f) Q75D70 (g) Q100D30 (h) Q100D50 (i) Q100D70...92

Figure 5-3 Thicknesses of non-PGM catalyst layers electrosprayed at various operating conditions. d is the needle-collector distance and Q is the flow rate of the catalyst ink (NOTE: The total thickness was normalized by the catalyst loading to eliminate the loading effect from the analysis) 93

Figure 5-4 Comparison of electrospraying technique and other deposition methods.................94

Figure 5-5 Porosities of non-PGM catalyst layer electrosprayed at various operating conditions 95

Figure 5-6 Comparison of porosity obtained by two different methods (Buoyancy and composition-based). $\rho_{Naf} = 2.0\ \mathrm{g/cm^3}$ used for the orange bars. 1.5 and $2.5\ \mathrm{g/cm^3}$ are used for lower and upper error bars, respectively. 96

Figure 5-7 Capillary pressure curves (a – c) and pore size distributions (d – f) of non-PGM catalyst layers electrosprayed under various operating conditions; (a), (d) d = 3.0 cm and Q = 0.50, 0.75, 1.0 mL/hr; (b), (e) d = 5.0 cm and Q = 0.50, 0.75, 1.0 mL/hr; (c), (f) d = 7.0 cm and Q = 0.50, 0.75, 1.0 mL/hr 97

Figure 5-8 Left: Pore size distribution of catalyst particles obtained with BJH theory. Right: Proposed structure of the electrosprayed PGM-free catalyst layer based on MIP and BJH pore size distributions. 98

Figure 5-9 Specific surface area of electrosprayed PGM-free catalyst layers (a) per active area and (b) per active volume 99

Figure 5-10 Effective diffusivities of the electrosprayed PGM-free catalyst layers at various operating conditions 100

Figure 5-11 Comparison of conventional inkjet printed Pt/C catalyst layer and the electrosprayed PGM-free catalyst layer – Black: Inkjet printed Pt/C (Vulcan) catalyst layer, Red: Inkjet printed Pt/C (Ketjenblack) catalyst layer and Blue: Electrosprayed PGM-free catalyst layer. 102

Figure 5-12 Tortuosity-Porosity plot of the electrosprayed PGM-free catalyst layers. (Lines indicate the power-law fit whereas the markers are the experimental data). *Note: The observed tortuosity from the work of Yu et al.[161] was calculated based on the information given. Others are plotted as given in the work..104

List of Tables

Table 3-1 Fuel cell operating conditions and geometric dimensions..37

Table 3-2 Solution domain..38

Table 3-3 Governing Equations and solved parameters...39

Table 3-4 Source terms and modeled domain 40

Table 3-5 Boundary conditions...41

Table 3-6 Optimum thickness and Nafion™ loading at each catalyst loading (0.76 V) 53

Table 3-7 Optimum thickness and Nafion™ loading at each catalyst loading (0.60 V) 55

Table 4-1 Summary of Porous Samples Tested for Diffusivity Measurement...........................69

Table 5-1 A summary of electrospray operating parameters and the catalyst loadings..............88

Table 5-2 Average pore diameter, Knudsen number, molecular diffusivity and Knudsen diffusivity of electrosprayed non-PGM catalyst layers...103

Table A-1 Model parameters for gas diffusion layers (SGL25BC)...125

Table A-2 Model parameters for microporous layers (SGL25BC) 126

Table A-3 Model parameters for polymer electrolyte membrane (NR-211) 126

Table A-4 Model parameters for catalyst layer (anode = Pt/C, cathode = non-PGM).............127

List of Abbreviations

BEG	A mixture of butylacetate, ethanol and glycol
BET	Brunauer-Emmett-Teller
CL	Catalyst layer
DOE	Department of Energy
ECSA	Electrochemical available surface area
EIS	Electrochemical impedance spectroscopy
ES	Electrospray
FC	Fuel cell
FIB	Focused ion beam
GDE	Gas diffusion electrode
GDL	Gas diffusion layer
HOR	Hydrogen oxidation reaction
I/C	Ionomer to Carbon ratio
IPA	Isopropyl alcohol
ITO	Indium-Tin-Oxide
PET	Polyethylene terephthalate
LHS	Left hand side
MIP	Mercury intrusion porosimetry
MOF	Metal organic framework
MPL	Microporous layer
ORR	Oxygen reduction reaction

PAN	Polyacrylonitrile
PEM	Polymer electrolyte (or proton exchange) membrane
PEMFC	Polymer electrolyte (or proton exchange) membrane fuel cell
PGM	Precious group metal (or Platinum group metal)
Pt	Platinum
Pt/C	Platinum supported on carbon
PTFE	Polytetrafluoroethylene
RH	Relative humidity
RHS	Right hand side
SEM	Scanning electron microscopy
SSM	Sacrificial support method
TPI	Tri-1,10-phenanthroline iron (II) perchlorate
W-K	Wicke-Kallenbach
ZIF	Zeolitic imidazolate framework

List of Symbols

Symbols	
a	Thermodynamic activity
a_w	Water activity
A_0	Specific surface area of the catalyst
A_v	Volumetric specific surface area
c_0	Concentration around the perimeter of the sample
c_0^{ref}	Reference concentration
c_b	Bulk concentration of species i
c_s	Surface concentration at the reaction site
c_t	Concentration of total gas mixture
$c(t)$	Time-dependent concentration
c_1	Initial concentration within the sample
d	Needle-to-collector distance in electrospray
d_g	Kinetic diameter of gas molecule
d_i	Diameter of pore i
$\vec{d}_i$	Driving force for mass transport of species i
d_{pore}	Average pore diameter
D_i	Bulk diffusion coefficient
$D_{i,j}$	Binary molecular diffusion coefficient
$D_{i,k}$	Knudsen diffusion coefficient
D^{eff}	Effective diffusion coefficient

D^T	Thermal diffusion coefficient
D_T^{eff}	Effective thermal-osmosis diffusion coefficient
D_λ	Back diffusion coefficient of water
e^-	electron
E	Thermodynamic potential at non-standard state
E^0	Thermodynamic potential at standard state
F	Faraday’s constant
$\vec{F}$	External force
$\vec{F}_{d,i}$	Net drag frictional force
$\vec{F}_{w,i}$	Knudsen frictional force
H^+	Proton
$\overline{H}$	Molar enthalpy
$H_{O_2,N}$	Henry’s law constant for oxygen through Nafion™
i	Volumetric current density
i_0^{ref}	Exchange current density
i_L	Limiting current density
j_{0T}, j_{0H}	Dual-path kinetics parameters
$J_n(r)$	Bessel function of n^{th} order
k_B	Boltzmann constant
k^{eff}	Effective thermal conductivity
Kn	Knudsen number
m_{FeNC}	Catalyst (Fe-N/C) loading per unit area

M_i	Molecular weight of species i
n	Number of electrons transferred in the electrochemical reaction
n_d	Drag coefficient in electro-osmosis
N_i	Mass flux of species i
p	Pressure
p_c	Capillary pressure
Q	Flow rate of catalyst ink in electrospray
r	Spatial coordinate in cylindrical coordinate system
r_{pore}	Pore radius
R	Gas constant
S	Source term
t	Time
T	temperature
T_0	Standard temperature $(25\ ℃)$
T_{cell}	Cell temperature
V_{cell}	Cell voltage
V_{FeNC}	Catalyst loading per unit volume
V_i	Pore volume of pore size d_i
V_T	Total pore volume
$\bar{V}_i$	Partial molar volume of species i
x_i	Mole fraction of species i
X_i	Normalized pore volume of pore size d_i

Greek Letters

α	Charge transfer coefficient / percolation network constant
α_n	n^{th} root of $J_0(r)$
γ	Reaction order / surface tension
δ	Thickness of samples
$\Delta\hat{g}_{rxn}^{0}$	Gibbs free energy change at standard state
$\Delta\hat{s}$	Entropy change
ε or ε_v	Porosity
ε_n	Ionomer phase fraction
ε_p	Percolation threshold
ε_s	Solid (catalyst) phase fraction
η	overpotential
θ	Contact angle
λ	Mean free path of gas species / water content in polymer electrolyte
λ_{eq}	Equilibrium water content in polymer electrolyte
μ_i	Chemical potential of species i
ρ_i	Density of species i
σ_{ij}	Collision diameter in Lennard-Jones potential
σ_m	Bulk proton conductivity
σ_s	Bulk electrical conductivity
σ_m^{eff}	Effect proton conductivity

σ_s^{eff}	Effect electrical conductivity
τ	tortuosity
ϕ_m	Electrolyte potential
ϕ_s	Electrical potential
ω_i	Mass fraction of species i
Ω	Collision integral Lennard-Jones potential

Chapter 1 Introduction

1.1. Motivation

The ongoing issues with climate change have led the mankind to search for sustainable energy future. "Hydrogen Economy", the term coined by John Bockris[1], and H2@Scale, a concept expanded from hydrogen economy for wide-scale hydrogen production and utilization[2], provide details on how this might be achieved (Figure 1-1). In the description of H2@Scale, electricity is produced by renewable means such as wind, solar and nuclear and stored in energy storage systems like batteries for later use. The electricity generated can be used to convert water into hydrogen and oxygen. Hydrogen then can be either directly used as a low carbon fuel for automotive vehicles, used in metal refining or ammonia production. Hydrogen can also be converted back to electricity, effectively creating a sustainable energy loop.

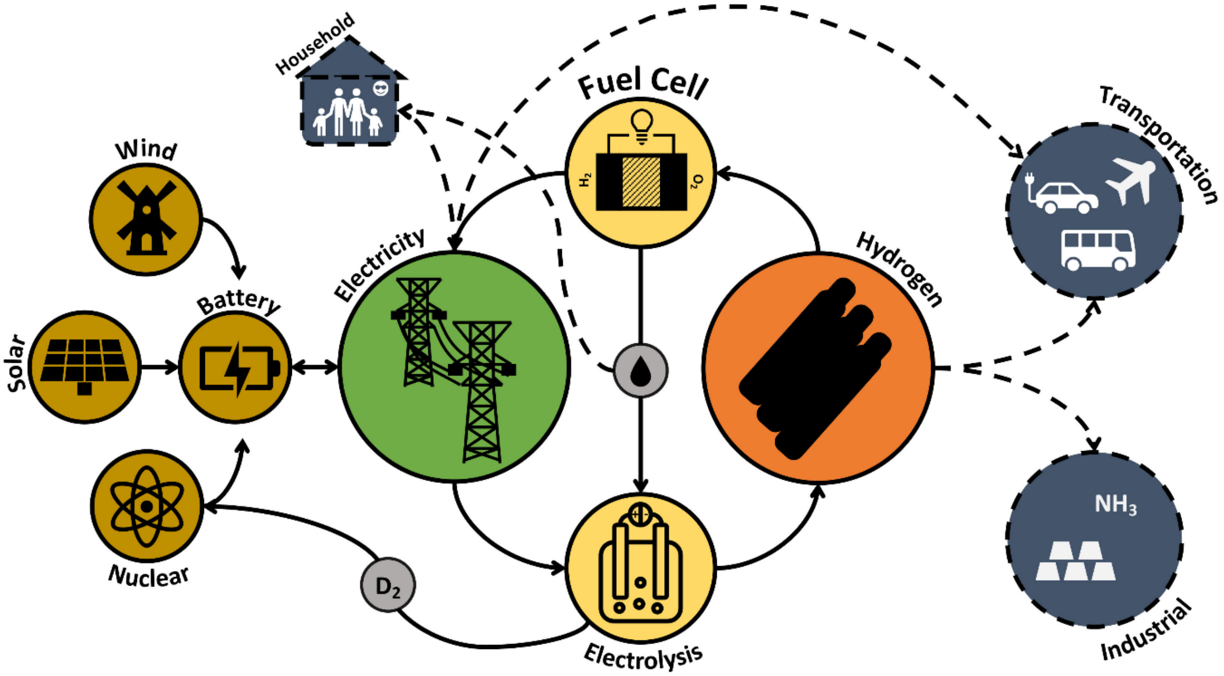

Figure 1-1 "Hydrogen Economy" described by H2@Scale concept.[2]

Fuel cell (FC) technology is arguably the most important component of the hydrogen economy since it acts as a bridge between electricity (power) and hydrogen (fuel). The main advantage of the FC is that it produces electricity from hydrogen with only water and heat as by-products, making it an environmentally benign energy technology, assuming the hydrogen is renewably generated. FC technology is particularly appealing in the transportation sector because it has the potential to replace its counterpart in the old “Carbon Economy”, the internal combustion engine. In fact, FC vehicles have already been commercialized by major automotive companies in various parts of the world. Unfortunately, FC vehicles are currently shadowed by its strong competitor, battery electric vehicles, in the market. However, FC still has advantages over batteries such as high-power output, fast fuel charge, long driving range and light weight. These advantages are ideal for heavy duty vehicles such as logistic trucks, buses and trains and together with the growing consensus on the transition into zero-emission fleets have synergistically brought the FC technology up to the top in the zero-emission commercial trucking market.[3]

Although, FC technology has made great progress in the last decade and now at the stage of transitioning from R&D to commercialization, there are still ongoing efforts on increasing the performance of the FC while keeping the cost down. Reducing the cost has been a particularly important target for broad commercialization. The price of Toyota Mirai 2020 base model is 58,550 USD while the price of other Toyota mid-sized sedans are from 24,000 to 28,000 USD.[4] Virtually all efforts to reduce these costs have been aimed at reducing the amount platinum (Pt) catalyst used, since it is the largest contributor to the high FC stack cost. Reducing the amount of Pt can essentially be accomplished in two ways: (1) use less Pt or (2) develop a Pt-free catalyst.

The former approach can further be divided into two categories. The first category requires compensating the lower Pt loading by increasing the accessibility and utilization of the active sites.[5–7] Typical conventional catalyst layers (CLs) are composed of Pt supported on carbon and ionomer. The reaction can only occur at or near the so-called triple phase boundary where all three phases meet. The ionomer is generally present in the form of thin film around the catalyst which adds to the oxygen transport resistance and reduces the Pt effectiveness. This has been shown to be even more significant for low Pt loading, therefore, designing improved CL microstructure is important. The second approach is to develop alternative Pt-based electrocatalysts such as Pt-alloy[8–11], core-shell[12–19], shape controlled nanocrystals[20–22] and nanoframes.[23–25] Despite great success in decreasing the Pt loading by fabricating novel CL microstructure and developing highly active Pt-base electrocatalysts, Pt loading must still be further reduced for FC technology to be economically competitive.[26]

The long-term and more economically viable strategy would be approach (2), to completely remove Pt. This has shown to be a promising alternative with the recent developments in non-precious group metal (non-PGM), particularly Fe-N/C, catalysts. However, non-PGM electrodes are generally fabricated at higher catalyst loading to make up for lower catalytic activity[27–29] and they inevitably become thick, usually 10 times thicker than the conventional Pt/C electrodes.[30] Thicker layers mean that the non-PGM CL suffer more from transport resistances of all species (gas, ions, and electrons) and careful engineering of the CL microstructure is even more important for non-PGM electrodes.

Currently, most work on non-PGM focuses on developing increasingly more active non-PGM catalysts that can match the performance of the Pt/C catalysts and less attention has been paid to the electrode structure. With the catalytic activity of non-PGM catalysts slowly approaching its target[27,28,31], the time has come to start looking into better electrode architecture and that is the broad focus of the present thesis.

1.2. Outline of the Thesis

This thesis aims to provide a strategy for producing rationally designed non-PGM catalyst layers. As part of this effort, a continuum-based modeling was implemented to search for an optimal structure of the non-PGM CLs. Then, a novel ex-situ characterization technique for measuring effective diffusivity in thin porous media has been developed, which was a missing tool for the analysis of CLs. Finally, non-PGM catalyst layers with a range of morphologies were fabricated via electrospraying apparatus built in-house and their transport and structural properties were extensively characterized experimentally.

This thesis is organized into six chapters. Chapter 1 provides a general background on current energy problems and motivation of the work. Chapter 2 presents an overview of the fuel cell and mass transport occurring in the catalyst layer as well as the available characterization techniques for effective diffusivity in the catalyst layer. The physics and known applications of electrospraying in catalyst layer fabrication is also discussed. Chapter 3 presents implementation of a continuum-based model for optimizing the non-PGM CL structure. An open-source FEM-based fuel cell simulation framework, OpenFCST, was used extensively in this work. Chapter 4 presents the novel characterization technique developed for measuring effective diffusivity in thin porous materials. Chapter 5 focuses on manufacturing the non-PGM catalyst layers and characterizing their structures. Chapter 6 sums up the thesis by summarizing key results from the thesis and presents some recommendations for future work.

Chapter 2 Background and Literature Review

2.1. Overview of Fuel Cell

2.1.1. Fuel Cell Operation

A fuel cell is a type of galvanic cell that produces electricity from flowing gases. The most common is the hydrogen fuel cell, also known as the polymer electrolyte membrane fuel cell (PEMFC)[1]. In a PEMFC the hydrogen oxidation reaction (HOR) and oxygen reduction reaction (ORR) occur as shown below.

$$\begin{cases} \text{HOR:} & \mathrm{H_2 \rightarrow 2H^+ + 2}e^- & \text{(Anode reaction)} \\ \text{ORR:} & \mathrm{\frac{1}{2}O_2 + 2H^+ + 2}e^- \mathrm{\rightarrow H_2O} & \text{(Cathode reaction)} \\ \text{Overall:} & \mathrm{H_2 + \frac{1}{2}O_2 \rightarrow H_2O} & \end{cases} \qquad [2\text{-}1]$$

It is analogous to the conventional combustion engine in a sense that a “fuel” is combusted (oxidized) to produce power, and the oxidant is air. In a combustion engine, a hydrocarbon is burned to produce heat and the heat is eventually converted to mechanical power whereas in fuel cell, hydrogen is burned to produce electrical power.

---

[1] The acronym PEM also sometimes means “proton exchange membrane”, which is another name for a polymer electrolyte membrane.

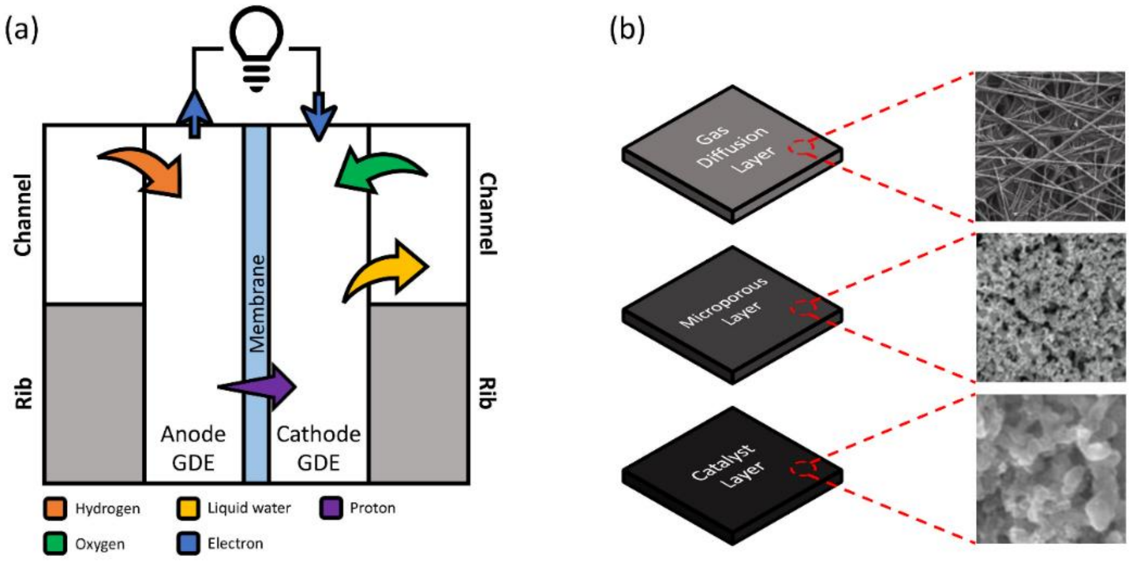

Figure 2-1 (a) Galvanic cell representation of PEMFC and a brief description of the transport processes occurring inside (b) Typical components of a gas diffusion electrode (GDE) and their images

Figure 2-1(a) shows a galvanic cell representation of a PEMFC. Hydrogen and air (containing oxygen) are fed to the anode and the cathode, respectively and the gaseous reactants transport through a composite porous layer called gas diffusion electrode (GDE) until they finally arrive at the reaction site. A typical GDE is composed of three layers: gas diffusion layer (GDL), microporous layer (MPL) and catalyst layer (CL) as shown in Figure 2-1(b). GDL is a carbon fiber matrix responsible for reactant transport, electron transport, water removal and mechanical support. The MPL has a similar role to the GDL, but also works as an intermediate layer between GDL and CL. The CL, which will be discussed more in-depth later, is the heart of the PEMFC where all electrochemical reactions occur. Generally, CLs are composed of nano-sized catalyst particles, ionomer and pore space, responsible for electron transfer, proton transfer and reactant transfer, respectively. As suggested by Eq. [2-1], the electrochemical reaction can only occur where reactants, electrons and protons meet. Engineering the structure to deliver all reactant species to these sites is the main challenge.

Once hydrogen arrives at the catalyst surface in the anode it is split into protons and electrons. Protons travel through the polymer electrolyte membrane (PEM), but because PEM is electrically insulating, electrons flow through the electrode to an external circuit to provide current. Protons and electrons finally meet at the reaction site in the cathode where they combine with oxygen to form water.

2.1.2. Fuel Cell Performance

The performance of a fuel cell can be represented by its current-voltage plot, also referred to as a polarization curve. When no current is drawn, the cell can theoretically output a maximum voltage stated by the Nernst equation (specifically for fuel cell reaction):

$$E = E^0 + \frac{\Delta \hat{s}}{nF}(T - T_0) - \frac{RT}{nF}\ln\left(\frac{a_{H_2O}}{a_{H_2}a_{O_2}^{1/2}}\right) \qquad [2\text{-}2]$$

where $E^0 = -\Delta\hat{g}^0_{rxn}/nF$ is the reversible potential at the standard state, $\Delta\hat{g}^0_{rxn}$ is the Gibbs free energy change at standard state, $\Delta\hat{s}$ is the entropy change, n is the number of electrons transferred in the reaction, R is the gas constant, T is the temperature, T_0 is the standard temperature $(25\ ℃)$ and a_{H_2O}, a_{H_2} and a_{O_2} are thermodynamic activity of $\mathrm{H_2O}$, $\mathrm{H_2}$ and $\mathrm{O_2}$, respectively. The first term on the right-hand side (RHS) is the theoretical voltage at standard conditions (25ºC, 1 atm), the second and the third terms are the temperature and pressure dependence of the theoretical voltage, respectively. Eq. [2-2] states, at standard state, the theoretical cell voltage would be about 1.23 V. At typical fuel cell operating conditions (i.e., 80ºC, 2 atm for both $\mathrm{H_2}$ and air), the theoretical voltage would be approximately 1.20 V, assuming only liquid water is produced ($a_{H_2O} = 1$ and $a_{H_2}, a_{O_2} = p_{H_2}, p_{O_2}$).

When the current is drawn from the cell, several irreversible losses are incurred depending on how much current is drawn. As higher current is drawn from the cell, the irreversible losses are more severe. There are three major types of irreversible losses (or overpotentials). They are activation losses (η_{act}) due to inefficiencies in the electrochemical reactions, ohmic losses (η_{ohm}) due to resistances in proton and electron conduction and concentration losses (η_{conc}) due to limited reactant concentration at high current density. The actual cell voltage (V_{cell}) then is the maximum reversible voltage minus the voltage drops incurred by various losses. The shape of the polarization curves of overpotentials as well as the net polarization curve is illustrated in Figure 2-2.

$$V_{cell} = E - \eta_{act} - \eta_{ohm} - \eta_{conc} \quad [2\text{-}3]$$

As evident in Figure 2-2, the activation losses are most significant at lower current, whereas at intermediate and higher current, ohmic losses and concentration losses dominate, respectively.

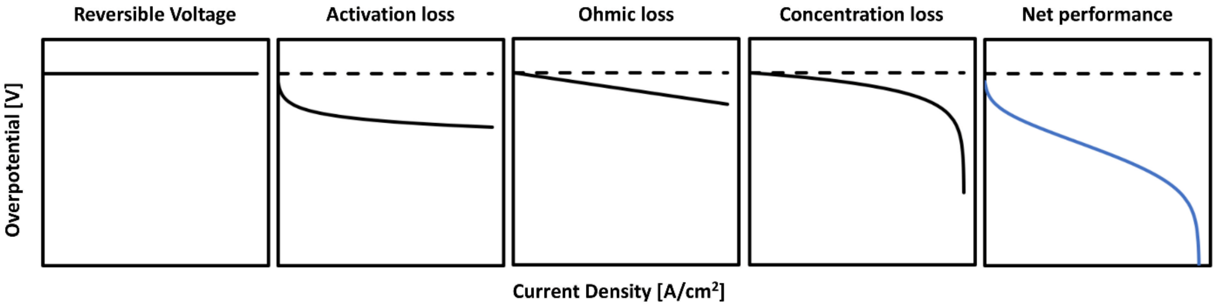

Figure 2-2 A summary of major losses in fuel cell performance. From left to right: theoretical reversible voltage, activation overpotential, ohmic overpotential, concentration overpotential and finally the net polarization curve

The activation loss essentially comes from an activation energy needed to instigate the electrochemical reaction. The activation barrier is the result of a series of more fundamental reaction steps such as formation of intermediates and transfer, adsorption and desorption of reacting species. The relationship between the activation overpotential and the current production is usually given by the Butler-Volmer equation:

$$i = A_v i_0^{ref} \left(\frac{c_i}{c_0^{ref}} \right)^{\gamma} \left[\exp\left(\frac{n\alpha_a F}{RT} \eta_{act} \right) - \exp\left(-\frac{n\alpha_c F}{RT} \eta_{act} \right) \right] \qquad [2\text{-}4]$$

where i is the volumetric current density, i_0^{ref} is the exchange current density, c_i is the concentration of reactant species at the reaction site, c_0^{ref} is the reference concentration, n is the number of electrons transferred in the reaction, γ is a reaction order, α is the charge transfer coefficient, R, T and F are gas constant, temperature and Faraday's constant, respectively. The subscripts a and c in the charge transfer coefficient denote anodic and cathodic reactions, respectively.

Typically for sluggish ORR, Butler-Volmer is not necessary and simple Tafel kinetics is deemed sufficient:

$$i = A_v i_0^{ref} \left(\frac{c_i}{c_0^{ref}} \right)^{\gamma} \exp\left(\frac{n\alpha F}{RT} \eta_{act} \right) \qquad [2\text{-}5]$$

There are more sophisticated reaction kinetic models such as dual-path kinetics[32] for HOR and double-trap kinetics for ORR[33,34] as well.

Ohmic losses come from the resistance to proton transport through the electrolyte, electron conduction through the solid phase as well as the contact resistances at layer interfaces. Generally, since the carbon components have a vastly higher conductivity than the polymeric membrane materials, ohmic losses caused by electron transport are regarded as small compared to that of protons. Therefore, most work focuses on developing thinner and more conductive electrolyte in an effort to reduce ohmic losses by proton transport. Contact resistances can be improved by compressing the FC stack. The overall ohmic resistance can be obtained by imagining each source of resistance is in series:

$$\eta_{ohm} = i \cdot (R_{H^+} + R_{e^-} + R_{contact}) \qquad [2\text{-}6]$$

The concentration losses are incurred by the kinetics as described by the Butler-Volmer equation. (Eq. [2-4]). Since, for concentration losses, the high current density region is the primary interest, the Butler-Volmer can be simplified to (Note: i below is the current density per unit area rather than the volumetric current density):

$$i = i_0^{ref}\left(\frac{c_i}{c_0^{ref}}\right)^{\gamma}\exp\left(\frac{n\alpha F}{RT}\eta_{act}\right) \qquad [2\text{-}7]$$

Or, written in terms of the activation losses (γ is usually close to 1):

$$\eta_{act} = \frac{RT}{n\alpha F}\ln\left(\frac{ic_0^{ref}}{i_0^{ref}c_i}\right) \qquad [2\text{-}8]$$

If the reactant concentration were to drop from a bulk concentration (c_b) to some lower concentration (c_s) at the reaction site due to mass transport limitation, the concentration overpotential caused by the kinetics would be:

$$\eta_{conc} = \frac{RT}{n\alpha F}\ln\frac{ic_0^{ref}}{i_0^{ref}c_s} - \frac{RT}{n\alpha F}\ln\frac{ic_0^{ref}}{i_0^{ref}c_b} = \frac{RT}{n\alpha F}\ln\frac{c_b}{c_s} \qquad [2\text{-}9]$$

Another interesting case in evaluating the performance of the fuel cell is when the reactant concentration drops to zero at high current. This current is the maximum theoretical current density that a fuel cell can achieve, also known as the limiting current density (i_L). i_L can be determined from the Faraday's law:

$$i = nFN_i \qquad [2\text{-}10]$$

where N_i is the mass flux of the reactant. Typically, for fuel cell, the mass flux can be safely assumed to be purely diffusive meaning $N_i = -D^{eff}(c_b - c_s)/\delta$ for porous electrodes with δ thickness. Since at the limiting current, $c_s = 0$, Eq. [2-10] becomes, after solving for i:

$$i = i_L = nFD^{eff}\frac{c_b}{\delta} \qquad [2\text{-}11]$$

2.2. Catalyst Layers

CLs are porous structures generally composed of catalyst, ionomer and void space where multiple competing processes are occurring simultaneously. For instance, high loading of catalysts would increase the kinetics, but at the same time it would also increase all transport resistances since the resulting layer would be thicker. Another example is that packing more catalyst into a given volume would increase the kinetics and the electrical conductivity of the CL, but because there is less porosity, it would hurt the overall mass transport characteristics. In general, designing CL is a classic engineering trade-off where "you can't win them all" and careful engineering is required to find the optimal structure. Figure 2-3 summarizes the transport challenges involved with catalyst layer design at multiple scales.

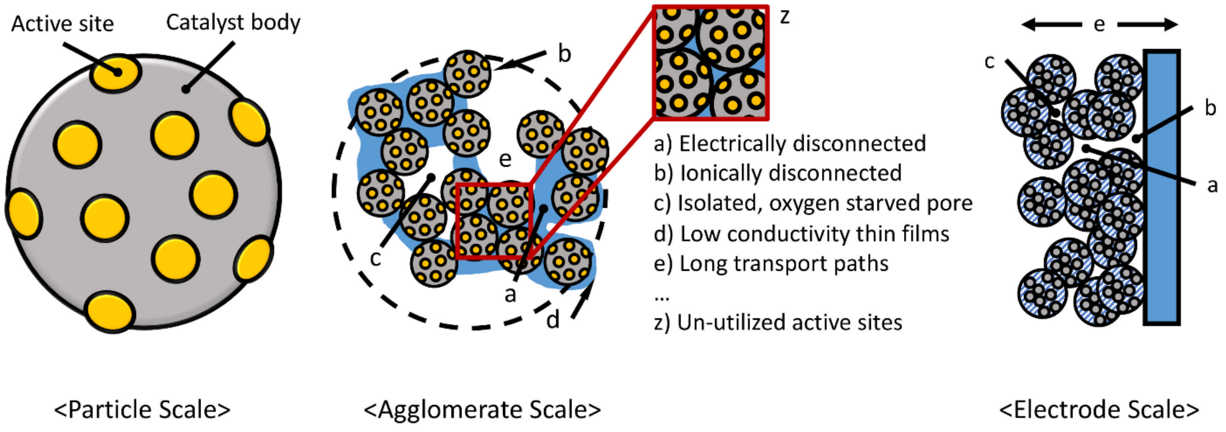

Figure 2-3 Typical catalyst layer structure and transport challenges. Note, for conventional Pt/C catalyst, active site = platinum and catalyst body = carbon black.

Historically, the catalyst layers were composed of unsupported Pt particles mixed with polytetrafluoroethylene (PTFE or Teflon®) which was hot pressed on to the membrane. The state-of-the-art Pt loading at the time was around $4\ \mathrm{mg_{Pt}/cm^2}$.[35] The major breakthrough came when Srinivasan et al. demonstrated that by incorporating of proton conducting ionomer into the catalyst layer with carbon supported Pt (Pt/C) achieved a similar performance as the high loading CL $(4\ \mathrm{mg_{Pt}/cm^2})$ with less than a tenth of the Pt loading $(0.35\ \mathrm{mg_{Pt}/cm^2})$.[35] This order-of-magnitude reduction in Pt usage moved fuel cells to within economic viability. In the 30 years since this groundbreaking work, the composition of the CL has not changed much, and the CLs composed of Pt/C and ionomer have now become the new convention. However, as mentioned in Chapter 1, Pt catalysts are scarcely available at limited locations and therefore expensive. Many efforts have been made to further reduce the amount of Pt required. Development of Pt alloy[8–11], core-shell catalysts[12–19] with Pt as the shell and shape-controlled highly active Pt catalysts[20–25] are just few examples. However, aforementioned catalysts still use Pt and for FC technology to be economically viable, further reduction in Pt is required.[26] Recent advances in non-Precious Group Metal (non-PGM) catalysts, which completely removes Pt from the fuel have shown some promising results[27,36,31,28] and Ballard Power Systems Inc., a global leader in FC technology, has even announced the first commercialization of non-PGM FC stack as an emergency backup power in 2017.[30] However, for more demanding applications such as automotive, further improvements in catalyst and catalyst layer designs are required. In the following subsections, some of the key advances in the performance of the non-PGM catalysts are highlighted. Also, since this thesis focuses primarily on producing CL with optimized transport, theoretical background on the transport processes occurring in CLs are discussed with a particular focus on the gas-phase diffusive mass transport. Available characterization techniques for the transport properties as well as their limitations are discussed.

2.2.1. Overview of Non-PGM Catalyst Layer Developments

There are many classes of non-PGM catalysts, but carbon supported transition metal nitrogen (M-N/C) materials (where M can be Co, Fe, Ni, Mn, etc.) are one of the most promising types of non-PGM catalysts. In particular, Fe-N/C catalyst has been gaining much attention. This thesis focuses on Fe-N/C and the term “non-PGM” and “Fe-N/C” are used interchangeably. The focus of this thesis is to design non-PGM electrode, not to design novel non-PGM catalyst, therefore this subsection is not meant to be an exhaustive review of non-PGM catalysts, but an attempt to highlight the notable advances in development of the non-PGM catalyst with cell performances. M-N/C catalyst dates back to 1964 when Jasinski[37] discovered that cobalt phthalocyanine has the ability to reduce oxygen. However, this experiment was carried out in an alkaline environment and it was found that, in acidic environment, cobalt phthalocyanine showed much lower activity and stability. The next breakthrough in non-PGM catalyst was made by Jahnke et al.[38] where they discovered heat treatment of transition metal macrocycles with high surface area carbon booted up the catalytic activity as well as the stability in acidic environment. However, direct heat treatment of macrocycle compound was too expensive to compete with Pt-based catalysts. The breakthrough made by Gupta el al.[39], where they synthesized a PGM-free ORR catalyst by heat treating a mixture of metal salts (i.e., Co(II) or Fe(II)), polyacrylonitrile (PAN) and high surface area carbon, gave researchers much more flexibility in designing the novel non-PGM catalysts.[40,27,36,41,29]

Currently, the state-of-the-art Fe-N/C catalysts give performance comparable to conventional Pt/C catalyst layers (0.2 – 0.4 $\mathrm{mg_{pt}/cm^2}$ loading) tested under air at the loading around 2 – 4 $\mathrm{mg_{cat}/cm^2}$ when tested under pure oxygen.[42] As a reference, a comparison between Pt/C catalyst with 0.1 $\mathrm{mg_{pt}/cm^2}$ loading and non-PGM catalyst layers with 4 $\mathrm{mg_{cat}/cm^2}$ is shown

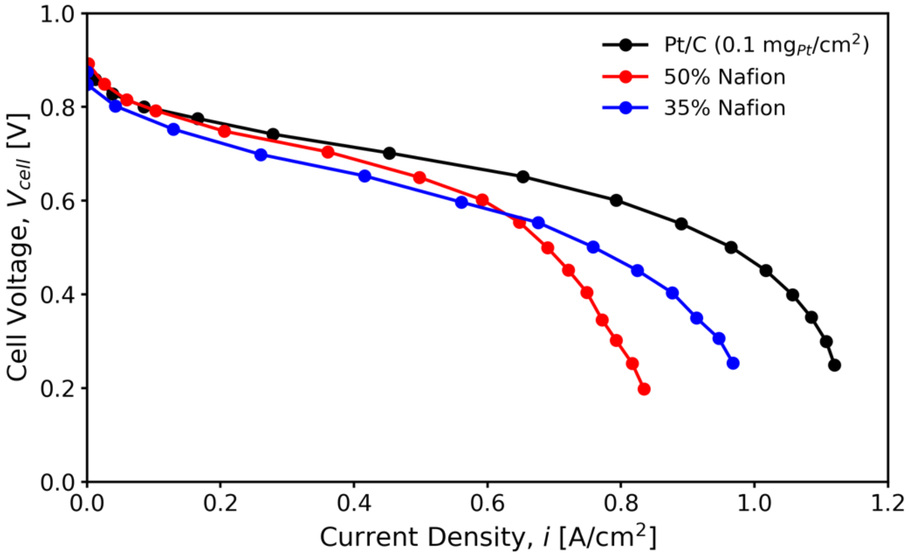

Figure 2-4 Comparison of performances between 0.1 $\mathrm{mg_{pt}/cm^2}$ loading Pt/C catalyst layer (black) and non-PGM catalyst layers at 4 $\mathrm{mg_{cat}/cm^2}$ loading with two different Nafion™ loadings – 35% (blue) and 50% (red). All tests performed under air.[28]

From Figure 2-4, it is clear that current densities for both Pt/C and non-PGM catalyst layers are nearly the same in the kinetic region (i.e., $V_{cell} > 0.8$) under identical conditions suggesting that the activity of non-PGM catalyst is as high as that of Pt/C. The performance of non-PGM catalyst layers at higher current density is lower due to the required thickness of non-PGM catalyst layer to make it as active as Pt/C catalyst layers. In their seminal work, Proietti et al.[27] achieved a peak power density of $0.91\ \mathrm{W/cm^2}$ after careful optimization of the synthesis conditions for iron acetate/phenanthroline/zeolitic imidazolate framework (ZIF-8)-derived catalyst. Shui et al.[31] also achieved a similar power density, i.e., around $0.9\ \mathrm{W/cm^2}$, with carbon-fiber based Fe-N/CF catalyst prepared via electrospinning with Tri-1,10-phenanthroline iron(II) perchlorate (TPI) and ZIFs, a subgroup of metal-organic-framework (MOF). Cyanamide-Polyaniline based Fe-N/C catalyst prepared by Chung et al.[28] exhibited peak power density of around $0.94\ \mathrm{W/cm^2}$. Deng et al.[43] have prepared MOF-derived carbon catalyst doped with single atom Fe. They were able to synthesize catalyst with high density Fe-site and high surface area by trapping ferrocene vapor, a volatile Fe compound, into ZIF-8. They reported polarization curves for various catalyst loadings from 0.5 to $5\ \mathrm{mg/cm^2}$ and $1\ \mathrm{mg/cm^2}$ catalyst layer showed the best performance with peak power density slightly less than $0.8\ \mathrm{W/cm^2}$. The fact that optimum catalyst loading was low at $1\ \mathrm{mg/cm^2}$ showed that the catalyst had high active site density. Zhan et al.[44] have prepared MOF-based highly dispersed non-PGM catalyst by ball-milling a mixture of Fe-containing MOF (NH_2-MIL-88B) and MOF-based carbon source (ZIF-8) with subsequent heat-treatments. After optimizing heat-treatments, the max peak power density of $\sim 0.7\ \mathrm{W/cm^2}$ was obtained with catalyst loading of $4\ \mathrm{mg/cm^2}$. Recently, Uddin et al.[45] reported a record high peak power density with $1.14\ \mathrm{W/cm^2}$ by optimizing the primary particle size of the MOF-derived Fe-N/C catalyst. The optimization of the primary particle size allowed improvement in the quality of the ionomer infiltration which enhanced the proton and reactant transport. All of the above tests, however, were done under pure oxygen to minimize the mass transport loss to make a direct comparison with Pt/C CLs. The peak power density under air is reported to be much lower, ranging from 0.2 to $0.6\ \mathrm{W/cm^2}$.[41,29,46–50] This indicates that non-PGM electrodes suffer severely from mass transport limitations due to the excessive thickness required to obtain a sufficient catalyst loading. Also, in real FC applications, using fully humidified O_2 as the reactant is not practical as it is more expensive and dangerous than operating under air. Also, high relative humidity can cause increase in the production cost due to installation of additional equipment on-board vehicles such as vapor exchange units. For future adoption of non-PGM catalysts into the industry, more insights on air operation and transport behavior inside the non-PGM electrodes under practical operating condition are necessary.

2.2.2. Mass Transport in Fuel Cell Catalyst Layers

This subsection deals with the general theory of mass transport in porous media in the context of catalyst layers. Also, some of the available experimental methods for characterizing mass transport properties in CLs are reviewed.

The most generalized form of the driving force for mass transport is provided by Taylor and Krishna[51]:

$$\vec{d}_i = \frac{1}{c_t RT}\left[c_i \nabla_{T,P}\mu_i + (c_i\bar{V}_i - \omega_i)\nabla p - \rho_i\left(\vec{F}_i - \sum_{j=1}^{n}\omega_j\vec{F}_j\right) + \sum_{j=1, j\neq i}^{n}\left(\frac{x_i x_j}{D_{i,j}}\right)\left(\frac{D_i^T}{\rho_i} - \frac{D_j^T}{\rho_j}\right)\nabla \ln T\right] \quad [2\text{-}12]$$

where $\vec{d}_i$ is the driving force for the mass transport, μ_i is the chemical potential of species i, ω_i is the mass fraction, c_i and c_t are the concentrations of species i and the total gas mixture, respectively, $\bar{V}_i$ is the partial molar volume, p is the total pressure, ρ_i is the density of species i, $\vec{F}$ is the external force, $D_{i,j}$ is the Maxwell-Stefan diffusion coefficient, D^T is the thermal diffusion coefficient and $x_{i\ (or\ j)}$are mole fraction of species i (or j). The various driving forces on the RHS represent chemical potential (composition) gradient, pressure gradient, external force such as electrical force and magnetic force, and finally thermal diffusion by temperature gradient.

In typical fuel cell settings, the mass transport driven by the temperature gradient can be neglected because the temperature gradient is usually small and the fact that the temperature term is inside the logarithmic term makes the contribution of thermal diffusion even smaller. Also, the reactant species in fuel cells are electrically neutral, therefore the external force term is not necessary. Finally, the pressure gradient within the porous layers of fuel cells is generally negligible since inert nitrogen is present to balance the pressure, leaving the concentration gradient as the primary driving force for reactants (H_2, O_2) as well as the product (water vapor) transport. Assuming ideal gas behavior, the driving force for mass transport simplifies to:

$$\vec{d}_i = \nabla x_i \qquad [2\text{-}13]$$

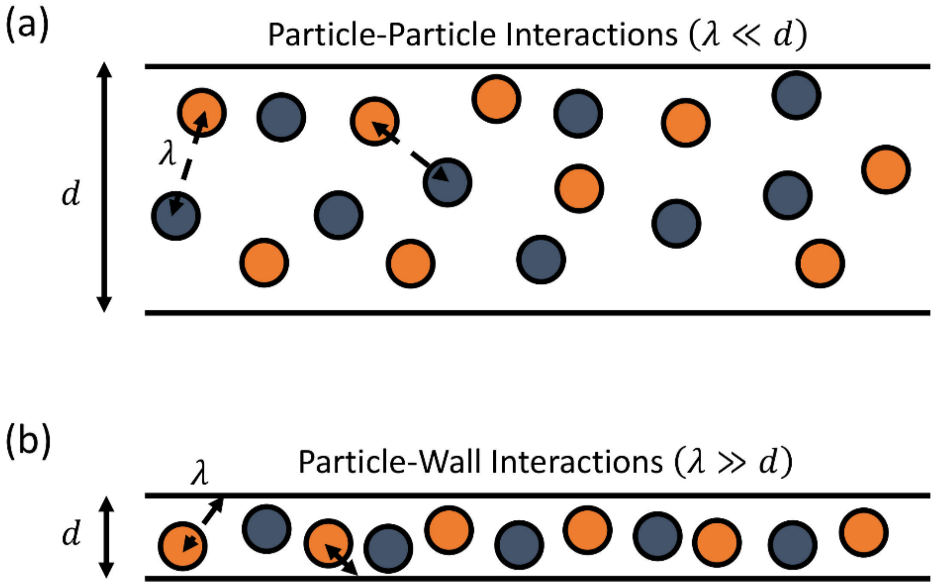

Figure 2-5 Illustration of different species interaction mechanisms. (a) particle-particle (molecular) interaction (b) particle-wall (Knudsen) interaction

In a mass transport system, this driving force is countered by the net frictional forces balancing out the overall system. In a sufficiently large open space, this frictional force mainly comes from particle-particle interactions as shown in Figure 2-5(a). The net drag frictional force $(\vec{F}_{d,i})$ is given by Krishna and Wesselingh[52]:

$$\vec{F}_{d,i} = \sum_{j=1,j\neq i}^{n} \frac{x_i \vec{N}_j - x_j \vec{N}_i}{c_t D_{i,j}} \qquad [2\text{-}14]$$

where x and $\vec{N}$ are mole fractions and molar fluxes of species i and j.

Equating Eqs. [2-13] and [2-14] yields:

$$\vec{F}_{d,i} = \vec{d}_i \Rightarrow \sum_{j=1,j\neq i}^{n} \frac{x_i\vec{N}_j - x_j\vec{N}_i}{c_t D_{i,j}} = \nabla x_i \qquad [2\text{-}15]$$

Eq. [2-15] is the well-known Maxwell-Stefan equation for multicomponent diffusion. For equimolar counter-diffusion $\left(\vec{N}_j = -\vec{N}_i\right)$ of binary mixtures $\left(x_j = 1 - x_i\right)$, the Maxwell-Stefan equation simplifies to Fick's law[53]:

$$\nabla x_i = -\frac{\vec{N}_i}{c_t D_{i,j}} \Rightarrow \vec{N}_i = -c_t D_{i,j} \nabla x_i \qquad [2\text{-}16]$$

In a special case of dilute mixtures ($x_i \ll 1$ and $x_j \approx 1$), Eq. [2-15] also simplifies to Fick's law. Technically speaking, the reactant mixture in the cathode side of the fuel cell is a multicomponent system consisting of N_2, O_2 and water vapor and Maxwell-Stefan equation is typically used. However, by making a simplifying assumption that the air is a dilute mixture consisting of mainly N_2, Fick's law can also be used for the reactant transport at the cathode.

For mass transport in a confined space such as within the pores of a porous material, the mean free path (λ) of the gas species is much longer than the diffusion path and the frictional force is mainly governed by the particle-wall interactions rather than particle-particle interactions as illustrated in Figure 2-5(b). This is known as the Knudsen friction and it is given as[54]:

$$\vec{F}_{w,i} = -\frac{\vec{N}_i}{c_t D_{i,k}} \qquad [2\text{-}17]$$

where $\vec{F}_{w,i}$ refers to Knudsen friction and $D_{i,k}$ is the Knudsen diffusion coefficient.

To maximize the kinetics, catalysts in fuel cells are inevitably nano-sized particles and as a result the catalyst layers contain pores in a nanometer range. To determine which mass transport regime the catalyst layers falls under, the Knudsen number (Kn) can be estimated using the order of magnitude analysis:

$$\text{Kn} = \frac{\lambda}{d_{pore}} \tag{2-18}$$

where d_{pore} is the average pore diameter of the catalyst layer and the mean free path of gas species (λ) is defined as:

$$\lambda = \frac{k_B T}{\sqrt{2} p \pi d_g^2} \tag{2-19}$$

where k_B is the Boltzmann constant and d_g is the effective molecular diameter of the gas species.

For fuel cell cathodes, $T \sim 10^2$ [K], $p \sim 10^5$ [Pa]. Also, $k_B \sim 10^{-23}$ $[\mathrm{m^2 \cdot kg/(s^2 \cdot K)}]$, $\pi \sim 10$ and $d_g \sim 10^{-10}$ [m] for oxygen. The order of magnitude of λ is around 10^{-8} [m]. $d_{pore} \sim 10^{-7}$ [m] is a good estimate for catalyst layers, yielding a Knudsen number of approximately, $\text{Kn} \approx 0.1$. The order of magnitude for the parameters are intentionally underestimated and Kn for catalyst layers will typically be greater than 0.1. For Kn between 0.1 and 10, both particle-particle and particle-wall interactions govern the mass transport. Combining Eqs. [2-13], [2-14] and [2-17]:

$$\vec{F}_{d,i} + \vec{F}_{w,i} = \vec{d}_i \Longrightarrow \sum_{j=1, j\neq i}^{n} \frac{x_i \vec{N}_j - x_j \vec{N}_i}{c_t D_{i,j}} - \frac{\vec{N}_i}{c_t D_{i,k}} = \nabla x_i \tag{2-20}$$

Again, making the simplifying assumption of air being a dilute mixture, Eq. [2-20] becomes:

$$-\frac{\vec{N}_i}{c_t D_{i,j}} - \frac{\vec{N}_i}{c_t D_{i,k}} = \nabla x_i \tag{2-21}$$

Or, solving for $\vec{N}_i$:

$$\vec{N}_i = -c_t \left(\frac{1}{D_{i,j}} + \frac{1}{D_{i,k}} \right) \nabla x_i \tag{2-22}$$

Eq. [2-22] can be put into a form similar to Fick's law by defining the bulk diffusivity (D_i)

as:

$$\frac{1}{D_i} = \frac{1}{D_{i,j}} + \frac{1}{D_{i,k}} \quad [2\text{-}23]$$

Eq. [2-23] is known as the Bosanquet approximation which combines both molecular and Knudsen diffusivity in a simple way and this approximation has been used extensively in catalyst layer modeling.[55,50,56–59]

There is also a third type of frictional force caused by the bulk movement of the molecules known as the viscous friction force. A boundary layer formed near the wall will reduce the net driving force and the viscous friction force is typically derived from the Darcy's law.[60] There are more sophisticated models combining all three mechanisms such as Binary Friction Model[61,62], Modified Binary Friction Model[63] and controversial Dusty-Gas Model.[54] However, these models are considered overly complicated for species transport in fuel cells. As it was mentioned before, because the primary mechanism for mass transport in catalyst layers is diffusion, Eq. [2-22] is the most widely used.

In open space, the molecular $(D_{i,j})$ and Knudsen $(D_{i,k})$ diffusion coefficients can be obtained using available correlations. For the molecular diffusivity, the Chapman-Enskog equation is commonly used:

$$D_{i,j} = \frac{0.00186 \cdot T^{3/2}}{P \cdot \sigma_{ij}^2 \cdot \Omega} \left(\frac{1}{M_i} + \frac{1}{M_j} \right)^{1/2} \quad [2\text{-}24]$$

where D_{ij} is the binary diffusion coefficient of species i and j measured in cm^2/s, T is the temperature in Kelvin, P is the pressure in atmospheres, and M_i and M_j are the molecular weights of species i and j, respectively. σ_{ij} and Ω are Lennard-Jones potential parameters from the Chapman-Enskog theory where the values for various species are given elsewhere.[64]

For the Knudsen diffusivity, the following equation is available[54]:

$$D_{i,k} = \frac{d_{pore}}{3}\sqrt{\frac{8RT}{\pi M_i}} \qquad [2\text{-}25]$$

where R is the gas constant, and d_{pore} is the average pore diameter calculated from the capillary pressure curve data as the volume-averaged pore diameter[57]:

$$d_{pore} = \frac{1}{V_T}\sum_i V_i d_i \qquad [2\text{-}26]$$

where V_T is the total pore volume, V_i is the pore volume at the i^{th} intrusion step and d_i is the corresponding pore diameter.

However, in porous materials such as catalyst layers, the mass flux is reduced by the presence of solid matrix and the tortuous diffusion pathway. Classically, these two effects have been accounted for by defining the effective diffusivity (D^{eff}) of the porous material:

$$D_i^{eff} = \frac{\varepsilon}{\tau} D_i \qquad [2\text{-}27]$$

where ε and τ are porosity and tortuosity of a porous medium, respectively.

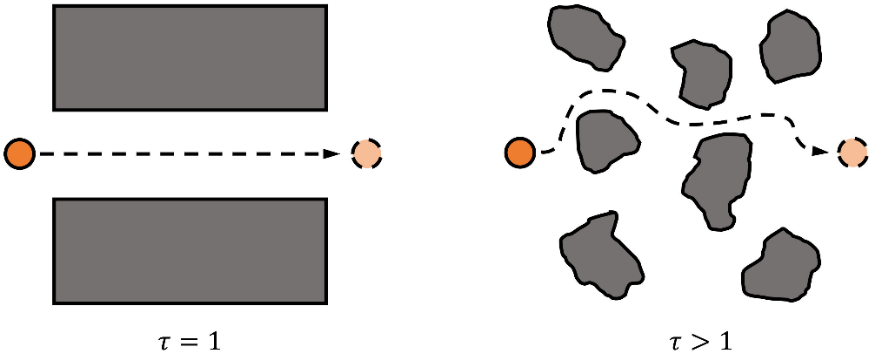

Figure 2-6 Tortuous diffusion pathway adds resistance to transport of a gas molecule

Tortuosity is generally thought to be a function of porosity. In general, tortuosity gets higher with lower porosity. There are several correlations to describe tortuosity or effective diffusivity as a function of porosity. The first correlation is the Bruggeman correlation which is as follows:

$$\tau = \varepsilon^{-0.5} \Rightarrow D_i^{eff}/D_i = \varepsilon^{1.5} \qquad [2\text{-}28]$$

The popularity of the Bruggeman equation presumably comes from its simplicity. In a recent study by Kim et al.[65] have shown that when Bruggeman's assumptions are satisfied (i.e., random, isotropic media with spherical particles), it predicts the effective diffusivity well. However, in most engineering cases, particles are not spherically shaped, limiting the usage of the Bruggeman correlation. This has been quickly realized by the fuel cell community[66–70] and alternative correlations are now more commonly used. Some works have used Archie's law which is a more generalized form of the Bruggeman correlation.[71,72] Archie's law uses the exponent in Eq. [2-28] as a fitting parameter, i.e., m in $D_i^{eff}/D_i = \varepsilon^m$. Another commonly used correlation is based on the percolation concept which states that the transport process cannot occur below a certain threshold:

$$D^{eff} = \left(\frac{\varepsilon - \varepsilon_p}{1 - \varepsilon_p}\right)^{\alpha} H(\varepsilon - \varepsilon_p) \qquad [2\text{-}29]$$

where ε is the porosity, ε_p is the percolation threshold and α is the percolation network constant usually fitted to experimental data, $H(\varepsilon - \varepsilon_p)$ is a Heaviside function to let D^{eff} go to zero below the percolation threshold. The percolation equation is typically used to estimate the effective properties of the fuel cell components made of granular materials (i.e., MPLs and CLs).[73,74]

From Fick's law, it can be inferred that higher D^{eff} would result in higher reactant flux to the reaction site therefore improving the performance of the fuel cell. It can be also said that, to rationally design the catalyst layer, it is crucial to be able to characterize the effective diffusion coefficient. However, probing the transport properties of thin, porous structure poses some challenge due to geometric constraints.

Nonetheless, there has been many efforts to characterize the effective diffusivity experimentally. Especially, there has been great progress on the gas diffusion layers. Kramer et al.[66] have developed a sophisticated approach called electrochemical diffusimetry to measure the through-plane and in-plane effective diffusivity using an electrochemical impedance spectroscopy (EIS) technique. In their study, GDLs were fully saturated with liquid electrolyte and the conductivity of the electrolyte was measured. The contribution from GDL and electrolyte were separated by impedance spectroscopy. In their subsequent study, Flückiger et al.[67] have applied electrochemical diffusimetry to investigate the anisotropy in various commercial GDLs. They found that Eq. [2-28] was inadequate for describing the diffusion coefficient in GDLs and the Bruggeman correlation substantially overpredicted the effective diffusivity. Baker et al.[75] developed a simple method to measure the effective diffusivity in GDLs by applying a gradient in water vapor on one side of the GDL. A water reservoir was placed on one side of the GDL and desiccant on the other side. They then measured the humidity to determine the vapor concentration gradient and weighed the desiccant to determine water flux. LaManna et al.[68] have developed a Wicke-Kallenbach type cell where GDL was placed between two channels and humidified gas was flowed in one channel and dry gas was flowed in the other channel. The method was tested with GDLs with various PTFE treatment. The obtained tortuosity ranged from about 2 to 6, depending on the amount of PTFE in GDL. Mangal et al.[76] have also developed a Wicke-Kallenbach type diffusion cell. They have developed the method so that simultaneous analysis of convection and diffusion was possible. Also, they used gas species for their analysis instead of water vapor. The diffusibility $\left(D_i^{eff}/D_i\right)$ of GDLs ranged from $0.248 - 0.086\ \mathrm{cm}^2/s$

which is in good agreement with other reported data. Zamel et al.[77,78] have developed a modified Loschmidt cell where GDL samples were placed between two compartment. One compartment was filled with nitrogen gas whereas the other compartment was filled with air. The GDL sample was placed between two compartments and oxygen was allowed to diffuse through GDL. The transient response of the oxygen concentration was measured and fitted to the analytical solution to obtain the effective diffusion coefficient. In their work, they found that all available correlations significantly overpredicted the diffusibility by 2 – 3 times. Rashapov et al.[69,70] developed a technique to measure the in-plane component of the effective diffusivity, which has relevance to the distribution of reactants under the ribs of the flow field. In their study, GDLs were clamped between two metal plates with metal spacers placed between the metal plates to control the level of compression. One pair of edges were sealed with putty and the other edges were left open for diffusion. They initially filled the sample with nitrogen gas and at the start of the experiment, the nitrogen flow was stopped, allowing oxygen gas to diffuse into the GDL microstructure. The transient response of the oxygen concentration was measured either at the center of the sample or at the end of the sample. The transient concentration profile was fitted with an analytical solution to obtain the effective diffusion coefficient at different compression. They made an attempt to fit the obtained diffusivity data to Tomadakis-Sotirchos correlation by fixing $\varepsilon_p = 0.11$ and only adjusting α. For Toray samples, α was found to be approximately 2.5. This method was subsequently used by Tranter et al.[79] to study the relative effective diffusivity in partially saturated GDLs.

There is less reported work on the effective diffusivity of MPLs and CLs due to the fact that they are not self-supporting making the experiments more challenging. Also, because their average pore sizes are in the nanometer range[59,80], some of the methods developed for GDL would not work. For example, if the methods developed by Baker et al.[75] and LaManna et al.[68] were to be applied to MPLs and CLs, water vapor would condense into the nano-pores due to Kelvin effect and therefore the mass flux obtained from the experiment would be misleading. Also, most commercial MPLs come sprayed on to GDLs making in-plane measurement impossible. For the through-plane measurement, the GDL and MPL contributions need to be separated. For catalyst layer, there is additional issue with their extreme thinness (< 10 um) where sealing the edges can get extremely difficult. Nonetheless, there have been some efforts on measuring the effective diffusivity of MPLs and CLs. Chan et al.[81] have used the modified Loschmidt cell developed by Zamel et al.[77,78] to determine the effective diffusivity of the MPLs. They first measure the overall effective diffusivity of the GDL coated with MPL. Then, they used resistors-in-series analogy to separate out the MPL contribution. They found the effective diffusivity of the MPL was about 7 times lower than the GDLs. Pant et al.[62] and Carrigy et al.[82] have used the same type of diffusion cell as Mangal et al.[76] to investigate the mass transport characteristics in microporous layers. Although, they were successful in obtaining the Knudsen contribution of the effective diffusivity, the molecular contribution was not reported. Shen et al.[83] used the modified Loschmidt cell to investigate the effect of CL thickness on the effective diffusivity. There were no apparent differences between the obtained diffusion coefficients at different thicknesses. They found that the effective diffusivity of CLs was about an order of magnitude lower than that of GDLs'. The modified Loschmidt cell was also used in other studies[84,85] to investigate the effect of catalyst layer composition on the effective diffusivity. Yu et al.[86] have developed a unique technique to directly measure the in-plane component of the effective diffusivity of CLs. CL samples were prepared on ETFE substrate and the samples were clamped between a plate with flow field and a blank plate. Air was flowed in the two outer channels and nitrogen gas was passed through the middle channel allowing oxygen to diffuse into the CL microstructure in in-plane direction. They measured the concentration of oxygen at the nitrogen outlet and calculated the effective diffusivity of different ionomer to carbon (I/C) ratio samples at various relative humidity (RH) based on Fick's first law. They found that at I/C = 0.5, decrease in the effective diffusivity was more significant at high RH whereas for I/C = 1.0 and 1.5, the decrease was insignificant.

Due to difficulty in experimental measurements of the effective diffusivity of CLs, there has also been some computational efforts to estimate the effective diffusivity of CLs. In the work of Inoue et al.[87], they have reconstructed CL microstructure from FIB-SEM slices and used random walk to determine the tortuosity of the catalyst layer. Their result was validated against experimental data where they measured the effective diffusivity of CL with diffusion cell similar to the one developed by Pant et al.[62]. Both computed and experimentally measured values were in good agreement. They found that the Archie's law exponent (i.e., m in $D_i^{eff}/D_i = \varepsilon^m$) was 6 with Knudsen effect and 4 without Knudsen effect. In a recent study by Babu et al.[50], they have used the nano-computed tomography to obtain various structural and transport properties of the non-PGM catalyst layers including the effective diffusion coefficient and the tortuosity. The Archie's law exponent ranged from 2.16 to 2.29 depending on the Nafion™ loading and the tortuosity ranged from 2.44 to 2.75.

2.3. Electrospraying

2.3.1. Physics of Electrospraying

The electrospraying (ES) technique is gaining popularity in preparing nanoparticles and thin films.[88] The electrospraying phenomena was first observed in 1917 by Zeleny when he photographed liquid droplet disintegrating at the tip of capillary tube at high potential. This phenomena was theoretically examined by Taylor[89] and the cone observed at the tip of the capillary needle became known as the Taylor cone. Cloupeau et al.[90] have extensively examined different modes in the electrospraying process experimentally. According to Cloupeau et al. there are three major modes in electrospraying process: 1) dripping mode where the large liquid droplet at the capillary tip is accelerated toward the substrate, but the potential is not high enough to disintegrate the large droplet. 2) Cone-jet mode where the liquid droplet at the capillary tip is elongated to form the Taylor cone followed by a single jet of liquid. This jet further breaks down into finer droplets until they hit the substrate. 3) Multi-jet mode where multiple jets are observed at the same time, usually at very high potential. In most cases, cone-jet mode is desirable because it is most predictable.

There are several forces acting on the Taylor cone as depicted in Figure 2-7.

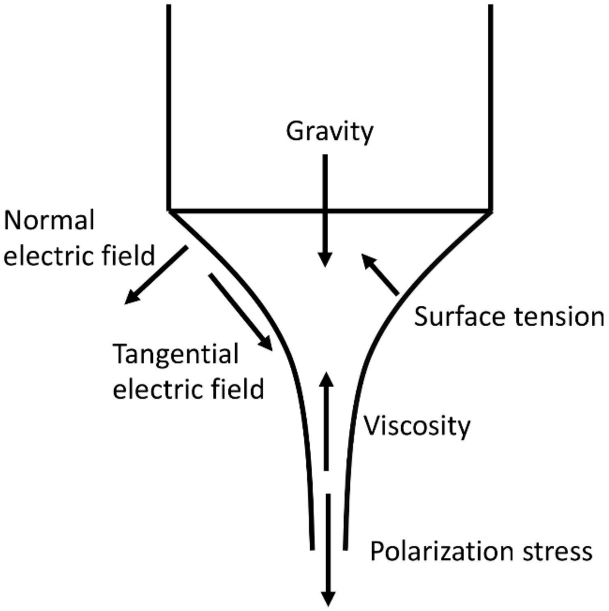

Figure 2-7 Several forces acting on liquid jet at cone-jet mode

From Figure 2-7, several parameters that has effect on the outcome of electrospraying deposition can be determined. Surface tension and viscosity are the characteristics of the liquid ink used in the process. Polarization stress and electric field are controlled by how much potential is applied between the capillary needle and the substrate. The conductivity of the liquid ink will also influence these properties. Another important operating parameter is the velocity of the jet which is determined by how fast the liquid is fed into the capillary needle. All these processing parameters expected to play part in determining the unique structure of the deposited nano-particle layer.

Figure 2-8 illustrates the mechanism of electrospraying deposition. When high potential is applied between the conductive capillary tip and the substrate, the liquid droplet is extended to form Taylor cone. The Taylor cone is further elongated to form a single stream of jet and initial droplets are detached from the jet. As initial droplets move toward the substrate, the solvent evaporates reducing the size of the droplet. At one point, the charges become compact within a single droplet and the repulsive force between the charges overcome the surface tension of the droplet. The critical limit is known as the Rayleigh limit and once the Rayleigh limit is reached, the droplet disintegrates into finer droplets. This process is repeated until they hit the substrate.

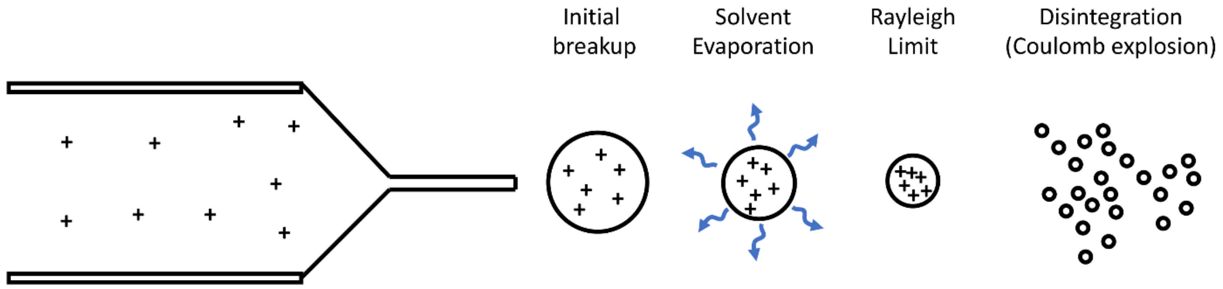

Figure 2-8 Electrospraying mechanism (assuming positive potential at the needle tip).

2.3.2. Application in Fuel Cell Catalyst Layers

Even though electrospraying allows for highly porous structure with simple adjustments to the processing parameters, it has never been used in fabricating non-PGM catalyst layers. The use of electrospraying in fabricating PEMFC catalyst layers was first demonstrated by Barturina et al.[91] with the conventional Pt/C catalyst. They deposited Pt/C catalyst on a membrane using the electrospraying technique and the polarization curve was measured to demonstrate that the electrospraying technique is suitable for fabricating the catalyst layer for fuel cell. No further analysis was performed. Benitez et al.[92] subsequently investigated the effect of deposition method on the performance. They fabricated Pt/C CL with four different techniques: impregnation, air spray, electrospray and commercial E-TEK CL. The CL fabricated by electrospraying technique outperformed all the other CLs and this was attributed to improved catalytic distribution with electrospraying technique. Chaparro et al.[93] have investigated the effect of solvent on the morphology of the electrosprayed CL. The solvent used in the study were isopropanol (IPA) and a mixture of butylacetate, ethanol and glycerol (BEG). Electrosprayed layers prepared with BEG showed a high mass specific area which was attributed to the low volatility of the solvent. In their subsequent study, Chaparro et al.[94] optimized the ionomer content and catalyst loading of the electrosprayed catalyst layer. An optimum Nafion™ loading was found to be at 15% which is much lower than that typically observed for catalyst layer prepared by standard methods such as air brush/spray. This was attributed to the improved ionomer coverage on the catalyst surface. Chaparro et al.[95] have published another work on electrosprayed CL, including characterization of the structural properties of the electrosprayed layers. They performed mercury porosimetry on the air brushed and electrosprayed CLs and found that the pore volume of the primary pores increased for the air brushed CLs whereas the pore volume decreased for the electrosprayed layers with respect to the catalyst powder. This was attributed to the fact that with electrospraying technique, the agglomerates can be disintegrated into a single aggregate allowing more homogeneous coverage of Nafion™ film. Martin et al.[96] have used the electrospraying technique to prepare ultra-low Pt loading catalyst layers. The catalyst loading ranged from $0.1\,\mathrm{mg_{Pt}/cm^2}$ down to $0.0125\,\mathrm{mg_{Pt}/cm^2}$. They observed that each catalyst loading had different optimum Nafion™ loading. For $0.1\ \mathrm{mg_{Pt}/cm^2}$, 30% Nafion™ was found to be the optimum whereas higher Nafion™ was required for lower loadings. The performance of the electrosprayed CLs were compared to the CL prepared by impregnation method with $1.0\,\mathrm{mg_{Pt}/cm^2}$ catalyst loading. Although, the CL prepared by impregnation outperformed the electrosprayed CLs, the Pt utilization was found to be substantially higher for the electrosprayed layer. In their subsequent study, Martin et al.[97] have investigate the effect of Nafon™ loading with ultra-low Pt loaded catalyst layer prepared by electrospraying technique. No apparent difference in the performance was observed between 30 – 50%, but sharp decrease in the performance was observed at Nafion™ loading higher than 50%. A high Pt utilization was again observed with the optimum Nafion™ loading. Chaparro et al.[98] have used the electrospraying technique to deposited Pt/C catalyst directly on the Nafion™ membrane. Different morphology was observed for the catalyst layer electrosprayed directly on the membrane with globular morphology whereas dendritic morphology was observed when electrosprayed on to GDL. The CL deposited on the membrane performed better than the one deposited on GDL due to better adherence. Takahashi et al.[99] have performed an optimization of various electrospraying conditions, i.e., needle-collector distance, the applied voltage and the nozzle diameter. The optimized electrosprayed CL showed improved ionomer coverage, increased electrochemically available surface area (ECSA) and more porous structure. Conde et al.[100] have investigated transport properties of the electrosprayed CLs using mass-transport-resistance measurements. The results revealed that the electrosprayed CLs showed low mass transport resistance compared to the conventional layers.

Based on the literature review, it can be summarized that the electrospraying technique improves the mass transport resistance by creating more porous structures as well as improves the ionomer coverage by disintegrating the catalyst agglomerate into aggregates. These characteristics of the electrospraying technique make electrospraying technique a prime target for fabricating non-PGM catalyst layers to compensate for resistances incurred by long transport paths.

Chapter 3 Numerical Simulation of PEMFC Performance to Determine Optimal Composition for Non-PGM Catalyst Layers

3.1. Preface

In this chapter, the optimal composition of non-PGM electrodes in terms of membrane electrode assembly (MEA) performance was investigated using a continuum-based model. A comprehensive parametric sweep over a wide range of catalyst loading and Nafion™ loading was performed.

3.2. Abstract

In the present study, the effect of catalyst layer composition on the performance of non-Precious Metal Group (non-PGM) cathode was investigated using a single-phase, non-isothermal continuum model under practical conditions (70% RH and air). The simulations were analyzed and compared at cell voltages 0.76 V and 0.60 V. 0.76 V is the rated voltage set by the United States Department of Energy (US DOE) whereas 0.60 V is the typically operating cell voltage in the automotive industry. Two cases were considered. For the first case, volumetric catalyst loading was held constant so that high loading corresponded to thicker layers. In this case, the optimum catalyst loading was found to be between 3.0 $\mathrm{mg/cm^2}$ and 4.0 $\mathrm{mg/cm^2}$.The optimum Nafion™ loading was found to be 70% which is higher than the reported values observed experimentally. This was attributed to the fact that most literature uses oxygen with 100% relative humidity (RH). At 100% RH, although proton conductivity is maximized, the porous layers are prone to water flooding, requiring more porosity than ionomer for better liquid water

transport. In the second case study, the thickness was allowed to vary at a fixed catalyst loading. Generally, thinner catalyst layers performed better at a fixed loading as expected due to the shorter transport lengths. The required amount of Nafion™ for optimal performance was somewhat reduced compared to the first case due to thinner electrode, ranging from 50 – 60%. There existed optimum porosity and ionomer volume fraction for each operating cell voltage. At 0.76 V, 20% porosity and 45% ionomer volume fraction were found to be optimal whereas at 0.60 V, 30% porosity and 35% ionomer volume fraction was the optimal pair. The modeling results suggest that a catalyst loading of $4.0\ \mathrm{mg/cm^2}$ and Nafion™ loading of 55% with the thickness of $50\ \mu\mathrm{m}$ will perform the best at the rated voltage set by the US DOE (i.e., 0.76 V), but slightly less Nafion™ loading (i.e., 50%) is better for practical operation at 0.60 V.

3.3. Introduction

Polymer electrolyte membrane fuel cells (PEMFCs) are slowly emerging into the market but lowering the high cost remains as the last piece of the puzzle for further market penetration. A promising option to reduce cost is to completely remove expensive Precious Group Metal (PGM) catalysts. Recently, Fe-N/C catalysts, one type of PGM-free catalysts, have shown promising results and a great number of Fe-N/C catalysts comparable to conventional Pt/C catalyst have been developed[27–29,31,41,49,101,102]. However, more work is required to further improve the performance of the non-PGM cathode.

To improve the performance of the non-PGM cathodes, essentially two approaches can be taken: (1) to improve the active site density of the catalyst and/or (2) to minimize the transport losses in the non-PGM electrodes to make up for the low catalytic activity. Approach (1) involves increasing the Fe-site density on the catalyst surface and a recent modeling study by Babu et al.[103] suggests that the active site density needs to be increased by 40 times or more for the non-PGM catalysts to meet the target proposed by the US Department of Energy (DOE). However, according to a study by Jaouen et al.[104], increasing the active site density above a certain limit would be quite challenging meaning the Fe-site density will remain as-is for a while. This leaves approach (2) which requires a thorough understanding of transport phenomena in the catalyst layer, and a careful optimization of the competing processes occurring in different phases present in the microstructure. With the state-of-the-art non-PGM catalysts approaching the performance of Pt/C catalyst, it is imperative to start investigating the relationship between the structure of the non-PGM cathode and the fuel cell performance for further improvement in the performance.

At the moment, there is a very limited number of published works on electrode architecture with respect to non-PGM catalyst. Most work has focused on increasing the catalytic activity of the non-PGM catalyst.[27,31,101,29,41,102] The reported peak power density ranges from about $0.5 - 1.4\ \mathrm{W/cm^2}$ under O_2 and $0.2 - 0.6\ \mathrm{W/cm^2}$ for air. These studies either optimized the catalyst synthesis process or developed a novel method to synthesize high surface area, high active site density catalysts.

Some works have looked into finding optimal Nafion™ loading or optimizing the integration of Nafion™ in the catalyst. Artyushkova et al.[105] made an effort to determine the optimal Nafion™ loading by fabricating non-PGM cathode with 4 different Nafion™ loadings (33, 50, 67 and 75%). The catalyst loading was fixed at $4\ \mathrm{mg/cm^2}$ and the optimal Nafion™ was determined to be at 50% when operated under O_2. Stariha et al.[47] made a similar attempt with three different Nafion™ loadings (25, 35 and 45%), but with various carbon additives incorporated in the catalyst ink to improve the electrical conductivity, and found that the optimal performance was achieve with 35% Nafion™ loading with no carbon additive. The catalyst loading was fixed at $4\ \mathrm{mg/cm^2}$. Chung et al.[28] synthesized non-PGM catalyst using two N precursors (cyanamide and polyaniline) which resulted in a hierarchical porous structure. They performed fuel cell tests under O_2 and air at catalyst loading of $4\ \mathrm{mg/cm^2}$ and at three different Nafion™ loadings (35, 50, 60%). The max peak power densities were $0.94\ \mathrm{W/cm^2}$ and $0.39\ \mathrm{W/cm^2}$ for O_2 and air, respectively, with 35% Nafion™ loading. Recently, Uddin et al.[45] fabricated a high power density non-PGM cathode by optimizing the ionomer integration into the catalyst and achieved $1.14\ \mathrm{W/cm^2}$ and $0.61\ \mathrm{W/cm^2}$ with O_2 and air, respectively.

To the best of authors' knowledge, only Banham et al.[42] looked into the effect of different catalyst loading. They fabricated non-PGM cathodes at catalyst loadings $1, 2.5$ and $4\ \mathrm{mg/cm^2}$ and tested them under both O_2 and air. When tested under air, the lowest kinetic overpotential was achieved at $4\ \mathrm{mg/cm^2}$ and the highest at $1\ \mathrm{mg/cm^2}$ as expected. No distinct difference in mass transport loss was observed between 1 and $2\ \mathrm{mg/cm^2}$, but $4\ \mathrm{mg/cm^2}$ cathode showed significant mass transport loss compared to the other two samples. When tested under O_2, a substantial performance increase was observed with $4\ \mathrm{mg/cm^2}$, but only a mild increase with 1 and $2\ \mathrm{mg_{cat}/cm^2}$ samples, showing that $4\ \mathrm{mg/cm^2}$ sample suffers the most from the mass transport loss. They also varied the Nafion™ content (35% and 40%) at $4\ \mathrm{mg/cm^2}$ loading to investigate whether less Nafion™ would improve the mass transport properties and indeed they observed improved mass transport and achieved $0.75\ \mathrm{W/cm^2}$ and $0.57\ \mathrm{W/cm^2}$ with O_2 and air, respectively. Overall, this study highlights the importance of rational catalyst layer design, but it also suggests that more comprehensive parametric study is required.

Although useful insights can be gleaned from the above-mentioned works, almost all testing was done with fully humidified oxygen gas presumably to minimize the ionic and mass transport resistance and to focus on the kinetics of the non-PGM. However, such condition is not practical because stack de-humidifiers incur additional cost, over-humidification creates other issues at the stack level such as channel flooding, and supplying pure oxygen is simply not feasible. In the present work, to investigate the optimal non-PGM electrode composition for conditions of practical relevance, a parametric study over a wide range of design variables (catalyst loading/thickness and Nafion™ loading) was carried out using a single-phase, non-isothermal model under a realistic fuel cell operating condition, for instance 70% RH inlet gas. The use of a single-phase model was justified because all practical fuel cell operation regimes avoid formation of liquid water, and the single-phase modeling is more theoretically sound.

3.4. Model Description

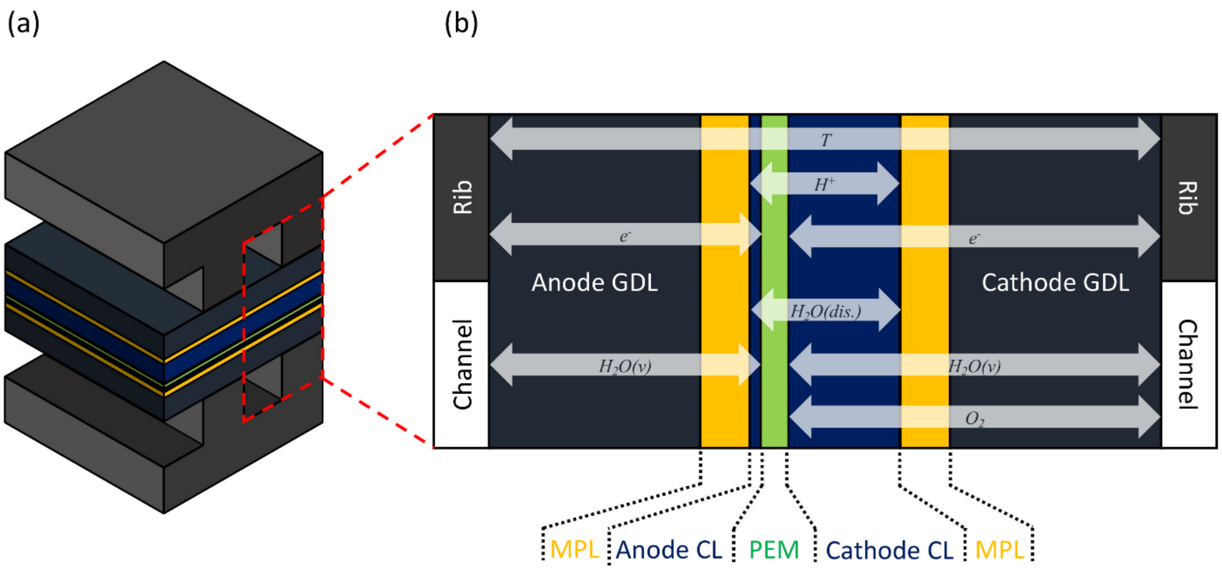

Figure 3-1 Schematic of the model domain and relevant species transport (a) 3D isometric view (b) 2D cross-sectional view

The membrane electrode assembly (MEA) was modeled as a simplified cross-the-channel two-dimensional geometry. Each electrode consists of a gas diffusion layer (GDL), a microporous layer (MPL) and a catalyst layer (CL). Figure 3-1 provides a description of the computational domain and the transport phenomena modeled in the domain. In the GDLs were modeled as anisotropic fibrous network whereas other porous layers (MPLs & CLs) were assumed to be isotropic. Channels and ribs were treated as boundary conditions and their dimensions are provided in Table 3-1.

Table 3-1 Fuel cell operating conditions and geometric dimensions

Parameters	Value
Operating Conditions	
Cell temperature [K]	353
Cathode pressure [kPa]	150
Cathode RH [%]	70
Anode Pressure [kPa]	150
Anode RH [%]	70
Cell geometry	
Channel width [cm]	0.1
Rib width [cm]	0.1

3.4.1. Assumptions

The single-phase, non-isothermal model developed by Bhaiya et al.[106] was used in this work. The model is based on the following assumptions:

1. The fuel cell is operated at steady-state and the pressure gradient through the porous layers is neglected.
2. Both anode and cathode catalyst layers are assumed to be homogeneous mixture of catalyst particles, ionomer and void space.
3. Gas flux is entirely diffusive and gas mixtures are assumed to be dilute mixtures (Fick's Law). Gas species behave ideally.
4. Liquid water transport is neglected.
5. Due to large interfacial area and low specific heat capacity of the gas, the gas and solid phases are assumed to be in local thermal equilibrium throughout all porous layers in the

MEA.[106]

6. Tafel kinetics is assumed for the ORR and the dual-pathway kinetics model[32,107] is used for HOR.

3.4.2. Governing equations

The transport of oxygen and water vapor were modeled with Fick's law for all porous layers. The transport of electrons and protons were described by Ohm's law for all porous layers in the MEA and electrolyte phase (i.e., CLs and PEM), respectively. The transport of sorbed water was solved in CLs and the PEM. The electro-osmotic effect, back diffusion and thermo-osmotic effects were considered for sorbed water transport. The thermal transport was solved in all MEA components. In thermal transport, it was assumed that conduction and diffusion were the dominant transport mechanisms and convection contribution was assumed to be relatively small.[106] It was also assumed that the thermo-diffusion effect (also known as Dufour effect), heat generation due to viscous dissipation were negligible. The modeled domain for each solved parameter is presented in Table 3-2 and the governing equations are summarized in Table 3-3.

Table 3-2 Solution domain

Variable	aGDL & aMPL	ACL	PEM	CCL	cGDL & cMPL
x_{O_2}	×	×	×	○	○
$x_{H_2O(v)}$	○	○	×	○	○
ϕ_m	×	○	○	○	×
ϕ_s	○	○	×	○	○
λ	×	○	○	○	×
T	○	○	○	○	○

Table 3-3 Governing Equations and solved parameters

Solved parameter	Governing Equation		
x_{O_2}	$-\nabla \cdot \left(c_t D_{O_2}^{eff} \nabla x_{O_2}\right)$	$= S_{O_2}$	[3-1]
$x_{H_2O(v)}$	$-\nabla \cdot \left(c_t D_{H_2O}^{eff} \nabla x_{H_2O}\right)$	$= S_{H_2O(v)}$	[3-2]
ϕ_{H^+}	$-\nabla \cdot \left(\sigma_m^{eff} \nabla \phi_m\right)$	$= S_{H^+}$	[3-3]
ϕ_{e^-}	$\nabla \cdot \left(\sigma_s^{eff} \nabla \phi_s\right)$	$= S_{e^-}$	[3-4]
λ	$-\nabla \cdot \left(n_d \frac{\sigma_m^{eff}}{F} \nabla \phi_m + \frac{\rho_{dry}}{EW} D_\lambda^{eff} \nabla \lambda + \frac{D_T^{eff}}{M_{H_2O}} \nabla T\right)$	$= S_\lambda$	[3-5]
T	$-\nabla \cdot \left(k^{eff} \nabla T\right) + \sum_{i=gas,\lambda} \vec{N}_j \cdot \nabla \overline{H}_j$	$= S_T$	[3-6]

The source terms accounted for the current generated due to electrochemical reactions at both catalyst layers. Sorbed water movement between the electrolyte and the void phases by evaporation were coupled by S_λ. In S_λ, k_t represents a time constant and is set to $10000\ \mathrm{s}^{-1}$ to ensure a strong coupling between the membrane and the CL.[74,106] The thermal source, S_T consisted of various sources of heat including reversible and irreversible heat generation due to half-cell reactions, vaporization of water, ohmic heating and water sorption phenomena. The source terms are summarized in Table 3-4. Contact resistances between the layers were neglected.

Table 3-4 Source terms and modeled domain

Source terms	GDL & MPL	ACL	CCL	PEM
S_{O_2}	0	0	$-i/4F$	0
$S_{H_2O(v)}$	0	$-S_\lambda$	$i/2F - S_\lambda$	0
S_{H^+}	0	i	$-i$	0
S_{e^-}	0	i	$-i$	0
S_λ	0	$k_t(\rho_{dry}/EW)(\lambda_{eq} - \lambda)$	$k_t(\rho_{dry}/EW)(\lambda_{eq} - \lambda)$	0
S_T	S_{ohm}	$S_{irr} + S_{rev} + S_{ohm} + S_{vap} + S_{sorp}$	$S_{irr} + S_{rev} + S_{ohm} + S_{vap} + S_{sorp}$	S_{ohm}
S_{irr}	0	$i\eta$	$-i\eta$	0
S_{rev}	0	$(i/2F)[-T(1 - f_{ORR})\Delta\bar{S}_{overall}]$	$(i/2F)(-Tf_{ORR}\Delta\bar{S}_{overall})$	0
S_{ohm}	$\sigma_s^{eff}(\nabla\phi_s \cdot \nabla\phi_s)$	$\sigma_s^{eff}(\nabla\phi_s \cdot \nabla\phi_s) + \sigma_m^{eff}(\nabla\phi_m \cdot \nabla\phi_m)$	$\sigma_s^{eff}(\nabla\phi_s \cdot \nabla\phi_s) + \sigma_m^{eff}(\nabla\phi_m \cdot \nabla\phi_m)$	$\sigma_m^{eff}(\nabla\phi_m \cdot \nabla\phi_m)$
S_{vap}	0	0	$-(i/2F)\bar{H}_{lv}$	0
S_{sorp}	0	$S_\lambda \bar{H}_{sorption}$	$S_\lambda \bar{H}_{sorption}$	0

The volumetric current density in the ACL was determined by the dual-path kinetics model proposed by Wang et al.[32,107] For the ORR at CCL, a simple Tafel kinetics was used:

$$i = A_v i_0^{ref} \left(\frac{c_{O_2}^{naf}}{c_{O_2}^{ref}} \right)^{\gamma} \exp\left(\frac{n\alpha F}{RT} \eta \right) \qquad [3\text{-}7]$$

where γ is the reaction order which is typically assumed to be 1, α is the charge transfer coefficient, F is the Faraday constant, R is the universal gas constant, T is the temperature, η is the overpotential defined as $(\phi_s - \phi_m - E)$. The theoretical cell voltage, E, was calculated using the Nernst equation. $c_{O_2}^{naf}$ represents the concentration of oxygen dissolved in thin Nafion™ film at the active site and is given by:

$$c_{O_2}^{naf} = c_t x_{O_2} / H_{O_2,N} \qquad [3\text{-}8]$$

The dimensionless Henry's law constant, $H_{O_2,N}$ is obtained by:

$$H_{O_2,N} = \frac{\widehat{H}_{O_2,N}}{RT} \quad \textbf{[3-9]}$$

$\widehat{H}_{O_2,N}$ is taken to be 3.52611×10^4 Pa · m^3/mol.[108]

The volumetric specific active surface area of the catalyst layer, A_v, was calculated by assuming the entire catalyst surface was available for reaction:

$$A_v = A_0 \cdot V_{FeNC} = A_0 \frac{m_{FeNC}}{\delta} \quad \textbf{[3-10]}$$

where A_0 is the specific surface area of the catalyst, V_{FeNC} is the catalyst loading per unit volume of the electrode, m_{FeNC} is the catalyst loading per unit area of the electrode and δ is the thickness of the catalyst layer. A_0 was measured by the gas sorption experiment (Quantachrome Gemini VII, US) using the BET equation. A_0 was measured to be $640\ \mathrm{m}^2_{FeNC}/\mathrm{g}_{FeNC}$.

3.4.3. Boundary conditions and model parameters

Table 3-5 Boundary conditions

Variable	AGDL-Ch	AGDL-Rib	CGDL-Ch	CGDL-Rib
x_{O_2}	no flux	no flux	$x_{O_2} = x^{\circ}_{O_2,c}$	no flux
$x_{H_2O(v)}$	$x_{H_2O(v)} = x^{\circ}_{H_2O(v),a}$	no flux	$x_{H_2O(v)} = x^{\circ}_{H_2O(v),c}$	no flux
ϕ_m	no flux	no flux	no flux	no flux
ϕ_s	no flux	$\phi_s = 0$	no flux	$\phi_s = V_{cell}$
λ	no flux	no flux	no flux	no flux
T	$\mathbf{n} \cdot \left(k^{eff} \nabla T\right) = 0$	$T = T_{cell}$	$\mathbf{n} \cdot \left(k^{eff} \nabla T\right) = 0$	$T = T_{cell}$

The boundary conditions are summarized in Table 3-5. No flux (symmetry) boundary conditions were applied at the top and bottom domain. $x^{\circ}_{O_2}$, $x^{\circ}_{H_2O(v)}$, T_{cell} and V_{cell} are the mole fraction of oxygen, mole fraction of water vapor, cell temperature and cell voltage which are determined based on the operating conditions.

The input parameters used in the current study are presented in Appendix from Table A-1 to Table A-4. All parameters were either measured or obtained from the literature except for the kinetic parameters for the ORR which is unknown given the novel nature of the non-PGM catalysts understudy. The reference exchange current density, i_0^{ref} was adapted from the work of Parasarathy et al.[109] and the charge transfer coefficient, α was assumed to be 0.6.

3.4.4. Parametric study

Two cases were considered for the parametric study. For the first case, it was assumed that the thickness of the catalyst layer increased linearly with the catalyst loading. This physically corresponds to adding material layer by layer with each layer having the same thickness. In other words, the volumetric catalyst loading, V_{FeNC} in Eq. [3-10], and consequently A_v, were kept constant, as the thickness of the catalyst layer varied. Workman et al.[29,41] reported that the non-PGM catalyst layer fabricated with $3.0\ \mathrm{mg/cm^2}$ catalyst loading and 45% Nafion™ loading had the thickness of $75\mu\mathrm{m}$. To be consistent with the reported value, $V_{FeNC} = 3.0\ \mathrm{mg \cdot cm^{-2}} / 0.0075\ \mathrm{cm} = 400\ \mathrm{mg_{FeNC}/cm_{\mathit{CL}}^3}$ was chosen. The catalyst loading, m_{FeNC} was calculated based on the thickness of the catalyst layer yielding the behavior shown in Figure 3-2.

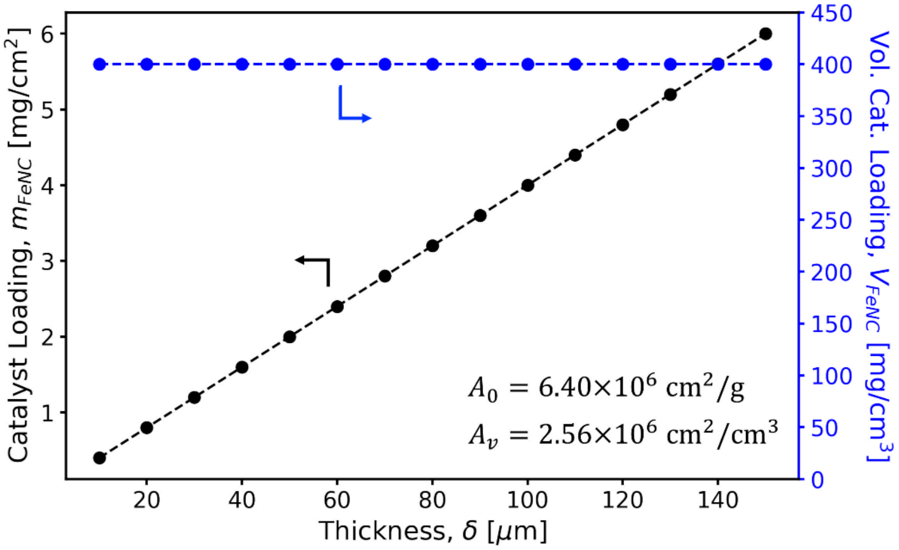

Figure 3-2 Case 1: constant V_{FeNC} – linear increase in the catalyst loading with the increasing thickness

For the second case, it was assumed that the thickness can be varied at the same catalyst loading (m_{FeNC}) and Nafion™ loading. This physically corresponds to creating more compact structure with fixed amount of catalyst and Nafion™. The second case study was performed since it is often of interest to see which combination of phase fractions (i.e., solid, ionomer and void) output the best performance. For this stage of the parametric study, at the given catalyst loading, both thicknesses and the ionomer loading were varied.

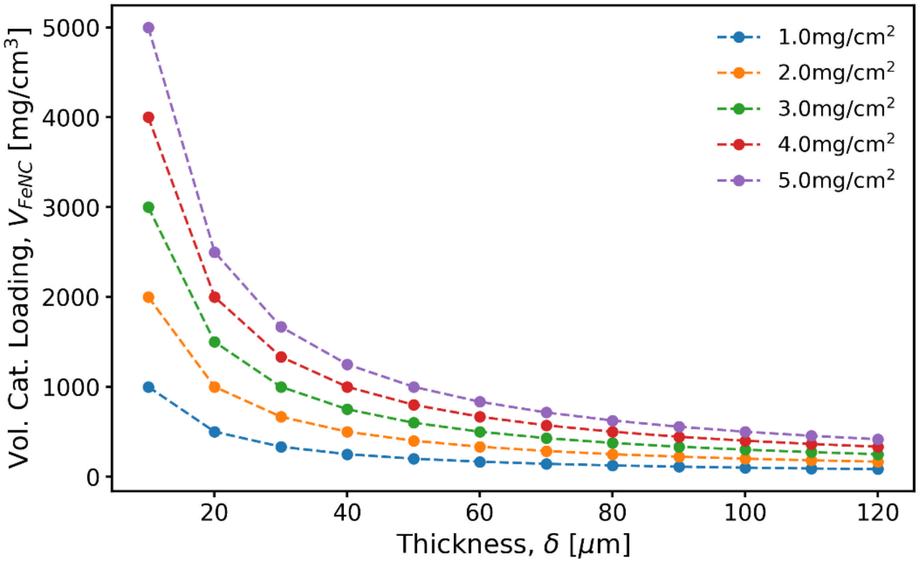

Figure 3-3 Case 2: variable V_{FeNC} – exponentially increasing catalyst loading per unit volume with decreasing thickness at the same catalyst loading per unit area

The physical and transport properties for GDLs, MPLs, PEM and ACL were kept constant for all simulations since the cathode catalyst layer was the primary interest in the current study. The RH was set to 70% rather than the often used 100% RH in the literature. The cell voltage of 0.6 V was used which is of a practical interest in transport applications. The DOE has specified target power density at a rated voltage. At 80°C, the rated voltage corresponds to 0.76 V[110] therefore, simulations were also run at 0.76 V. The inlet pressure for both anode and cathode were fixed at 150 kPa as suggested by the DOE.[110] The operating conditions are summarized in Table 3-1.

3.5. Results and Discussion

3.5.1. Case Study 1: Constant V_{FeNC}

For the first case study, a parametric study was performed with thickness ranging from 10 to $200\ \mu\text{m}$ with an increment of $10\ \mu\text{m}$. This corresponds to 0.40 to $6.0\ \text{mg/cm}^2$ with constant volumetric catalyst loading, V_{FeNC} ~~assumption made in the present study~~. The Nafion™ loading was varied from 10% to 80% with 5% increments.

3.5.1.1. Operation at 0.76 V

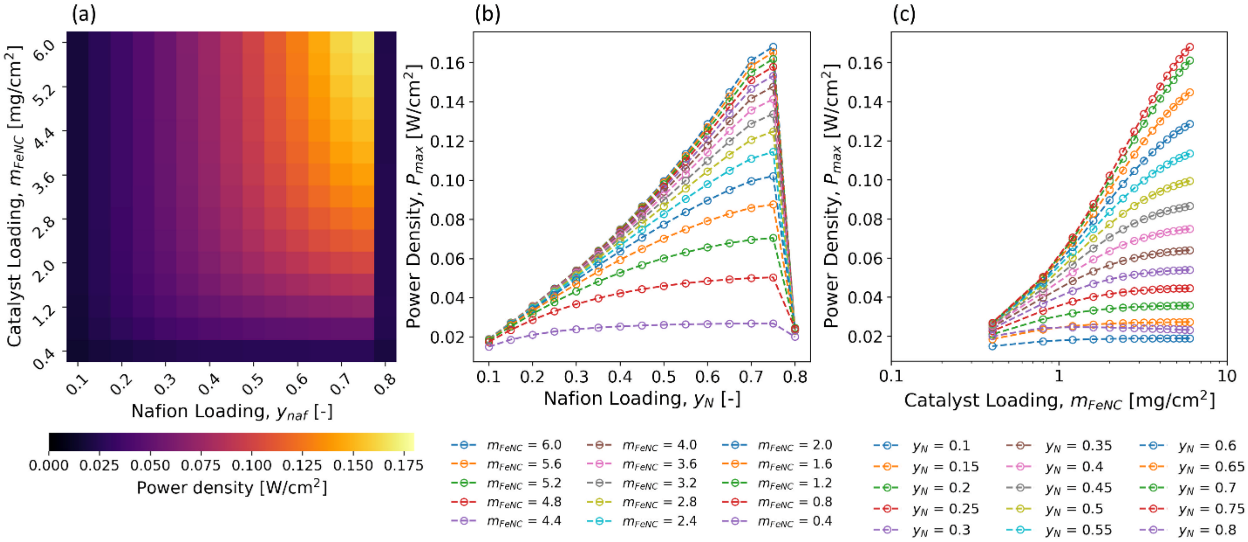

Figure 3-4 Power density at various catalyst and Nafion™ loadings at V_{cell} = 0.76 V (a) 2-D visualization (b) effect of Nafion™ loading on the performance (c) effect of catalyst loading on the performance

Figure 3-4(a) shows a two-dimensional representation of the power density at corresponding catalyst loading and Nafion™ loading. From Figure 3-4(a), it is evident that the performance generally increases with higher catalyst loading as well as higher Nafion™ loading. This is likely due to the fact that, at 0.76 V, the performance is controlled by the kinetics and proton conductivity and less by mass transport. Therefore, higher catalyst and Nafion™ loading led to better performance. The power density was plotted against the Nafion™ loading at various catalyst loadings in Figure 3-4(b). It can be seen that the performance improves with increasing Nafion™ loading until the maximum performance at y_N = 0.75 for all catalyst loadings. Then, the performance sharply decreases at y_N = 0.80 because mass transport resistance started to dominate. In Figure 3-4(c), the power density was plotted against the catalyst loading at various

Nafion™ loadings. The performance of the non-PGM cathode increased with the increasing catalyst loading. From Figure 3-4(c), the rate of performance increase starts to decay at higher loading, hinting that there exists a maximum catalyst loading at 0.76 V; though no optimal loading was found within the studied range. This result is somewhat in line with the experimental work carried out by Banham et al.[42] where increased current density was observed by increasing the catalyst loading up to $4.0\ \mathrm{mg/cm^2}$ at 0.76 V. However, direct comparison with the experimental work by Banham et al. is difficult since the maximum catalyst loading used in their study was $4.0\ \mathrm{mg/cm^2}$. Also, the differences in kinetic overpotential between $2.5\ \mathrm{mg/cm^2}$ and $4.0\ \mathrm{mg/cm^2}$ layers were minimal, which indicates that increasing the catalyst loading further may not necessarily cause a decrease in the kinetic overpotential. The possible explanation is the difference in the relative humidity in the reactant gas used in each work. In the work of Banham et al. 100% RH was used whereas in the present modeling work, 70% RH was used. This is actually a crucial difference since with 100% RH, water flooding becomes more severe. At 100% RH, as soon as electrochemical reaction takes place, water will start to condense into the pore space since the reactant gas is already fully saturated with water and the mass transport resistance will definitely be incurred earlier than the cell ran with 70% RH. This is also shown in the work of Banham et al. where $4.0\ \mathrm{mg/cm^2}$ sample performs slightly better up to 0.75 V, but when $V_{cell} < 0.75$ V, $2.5\ \mathrm{mg/cm^2}$ sample starts to perform better.

3.5.1.2. Operation at 0.60 V

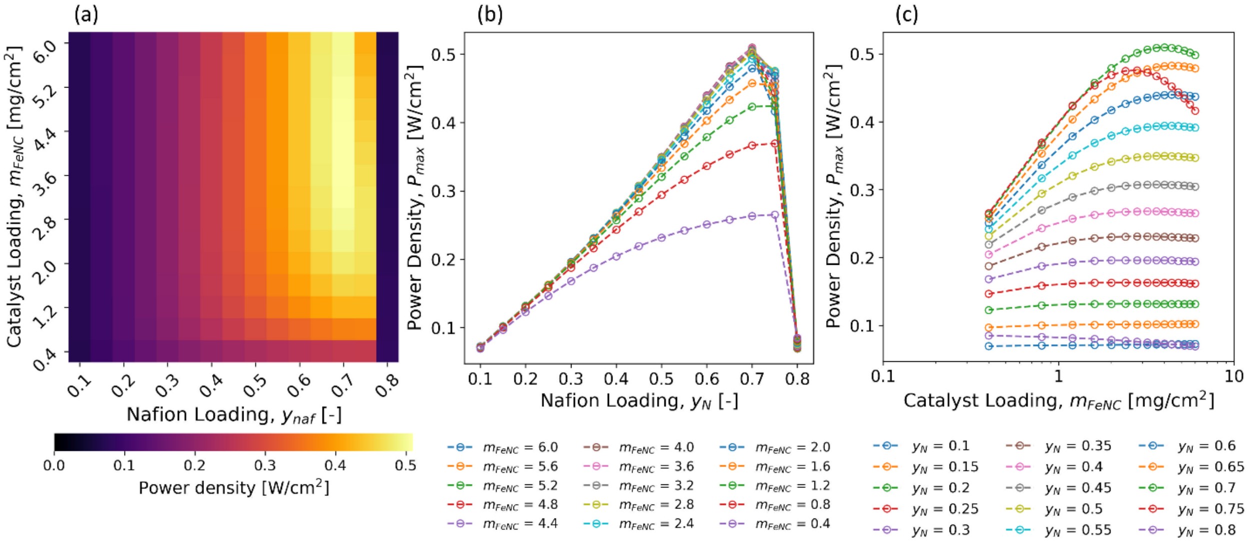

Figure 3-5 Power density at various catalyst and Nafion™ loadings at $V_{cell} = 0.60$ V (a) 2-D visualization (b) effect of Nafion™ loading on the performance (c) effect of catalyst loading on the performance

Figure 3-5(a) shows the two-dimensional visualization of the power density at 0.60 V with respect to the catalyst and Nafion™ loadings. From the simulation results, the optimum power density was obtained at catalyst loading of about 4.0 $\mathrm{mg/cm^2}$ and the Nafion™ loading of about 70%. Although, the optimum catalyst loading agreed with most published works, the optimum Nafion™ loading was significantly higher. For the conventional Pt/C electrodes, Antolini et al.[111] presented an empirical equation to find the optimal Nafion™ loading for Pt/C electrodes and according to the empirical equation presented by Antolini et al., the optimal Nafion™ loading was always 36%, irrespective of the catalyst loading. Experimental work by Passalacqua et al.[112] suggested that an optimum Nafion™ loading existed at 33% and the work done by Qi et al.[113] suggested 30%. A single optimal Nafion™ loading is seemingly true according to Figure 3-5(b) where the power density is plotted against the Nafion™ loading. In Figure 3-5(b), the power density peaks at 70% Nafion™ for all catalyst loadings and experiences a sharp decrease afterwards due to loss in the porosity for the reactants to transport through. For non-PGM catalyst layers, Artyushkova et al.[105] found that 50% Nafion™ loading was the optimum at the catalyst loading of 4 $\mathrm{mg/cm^2}$ after testing four different Nafion™ loadings: 33, 50, 67 and 75%. Stariha et al. conducted a similar study with 25, 35 and 45% Nafion™, but the optimal Nafion™ was found to be much lower at 35%. At 45% Nafion™, the performance was significantly reduced at 0.60 V due to increased mass transport resistance. Chung et al.[28] also tested their non-PGM catalyst at three different Nafion™ loadings (35, 50 and 60%) and according to the reported polarization curves, 50% Nafion™ performed the best at 0.60 V whereas 60% Nafion™ loading performed worse than 35%. Banham et al.[42] tested non-PGM electrodes with two different Nafion™ loadings and 35% Nafion™ loading was found to be the optimal due to better mass transport. Uddin et al.[45] found that 44% (I/C = 0.8) was the optimal Nafion™ for their catalyst. Although, unlike Pt/C catalyst, the optimal Nafion™ loading varied a lot between literature (i.e., from 35% to 50%), the simulation results still show higher Nafion™ loading than any other reported optimum Nafion™ loading for non-PGM catalysts. A possible explanation for the higher Nafion™ loading in the present study is again the lower relative humidity. As stated earlier, most non-PGM CLs are tested at 100% RH to maximize the proton conductivity. However, operating at 100% RH would flood the electrode, significantly limiting the performance at higher current density. This is especially important given the hydrophilic nature of the non-PGM catalysts.[103,114] At 70% RH, flooding is less likely to occur except for possibly in the micropores within the agglomerate particles due to reduced vapor pressure caused by Kelvin effect. The main passageway for the reactants, i.e., inter-agglomerate secondary pores, should still be relatively clear of liquid water. However, as a result of lower RH, the proton conductivity becomes lower and therefore requiring a higher Nafion™ loading to make up for the lower proton conductivity by increasing the electrochemically active surface area. Although, increased Nafion™ content could also increase the thickness of the Nafion™ film around the agglomerates, because 0.60 V is generally not regarded as the mass transport limited region, increased film thickness would have a small effect on the concentration overpotential. This was experimentally shown in the work of Uddin et al.[45] where they tested non-PGM MEAs under 60 and 100% RH. Initially at lower current density, the MEA tested under 100% RH showed lower overpotential due to improved kinetics and increased proton conductivity. However, at higher current density, the voltage of the MEA tested under 100% RH started to drop quickly and the MEA started to perform better with 60% RH.

The effect of catalyst loading/thickness was also investigated. Figure 3-5(c) shows the power density plotted against the catalyst loading. Interestingly, no significant improvement was observed with the catalyst loading above about 3.0 $\mathrm{mg/cm^2}$ for all Nafion™ loadings, except for the case with 75 and 80% Nafion™ loading. For 75% Nafion™ loading, the performance increased until about 2.5 $\mathrm{mg/cm^2}$, but further increase in the catalyst loading decreased the performance due to added resistance by the thickness. For 80% Nafion™, the performance actually increased with decreasing catalyst loading. This is because, at 80% Nafion™ loading, due to the loss of pore space, the performance is mass transport limited meaning the performance is dominated by the thickness of the CL rather than the kinetics (amount of catalyst). For all other Nafion™ loadings, there existed an optimum catalyst loading, although insignificant at loading higher 3.0 $\mathrm{mg/cm^2}$.

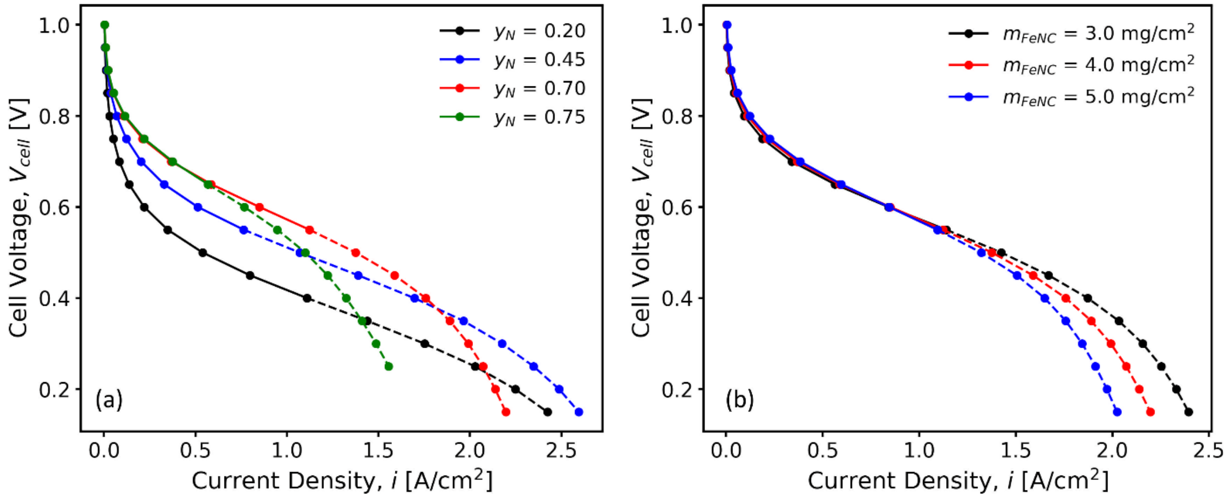

Figure 3-6 Polarization curves at various ink compositions: (a) Catalyst loading fixed at $4.0\ \mathrm{mg/cm^2}$. Nafion™ loading varied from 0.20 to 0.75 (b) Catalyst loading varied from 3.0 to $5.0\ \mathrm{mg/cm^2}$. Nafion™ loading fixed at 0.70. The dashed lines represent where the maximum relative humidity is > 100%

Figure 3-6(a) shows the polarization curves for catalyst loading fixed at $4.0\ \mathrm{mg/cm^2}$ and at four different Nafion™ loadings (20, 45, 70 and 75%). $4.0\ \mathrm{mg/cm^2}$ was chosen because it was found to be the optimal catalyst loading. At low Nafion™ loading (20%), there was an initial sharp decrease in the overpotential. This is most likely due to low electrolyte potential caused by low proton conductivity (i.e., $\eta = \phi_s - \phi_m - E$). The performance improves at 0.76 V and 0.60 V with increasing Nafion™ loading until 70%. However, with 70% Nafion™ loading, the performance was more severely influenced by the mass transport at high current density due to low porosity. With 75% Nafion™, the performance started to decrease at 0.60 V, but it still outperformed 20 and 45% Nafion™ loaded cathodes in the kinetic region.

In Figure 3-6(b), Nafion™ loading was fixed at 70% which was found to be the optimum Nafion™ loading. The polarization curves for three different catalyst loadings were simulated $(3.0, 4.0$ and $5.0\ \mathrm{mg/cm^2})$. At 0.76 V, higher current density was obtained with higher catalyst loading, but the improvement was minimal. As it was shown in Figure 3-5(c), a negligible performance gain was observed from depositing catalyst higher than $3.0\ \mathrm{mg/cm^2}$ at the kinetic regime. In practical terms, increasing the catalyst loading higher than $3.0\ \mathrm{mg/cm^2}$ would just increase the material cost as well as the transport resistance as observed in Figure 3-6(b) with a minimal improvement in the performance.

In summary when constant volumetric catalyst loading was assumed, regardless of the areal catalyst loading, the optimum Nafion™ loading was obtained at 70%. Although, the optimal point was obtained at $m_{FeNC} = 4.0\ \mathrm{mg \cdot cm^{-2}}$ and $y_N = 0.70$, increasing the catalyst loading above $3.0\ \mathrm{mg \cdot cm^{-2}}$ showed only a negligible performance increase. The obtained optimum Nafion™ loading was higher than the ones reported in the literature. This was attributed to the fact that lower RH (70%) was used in the present study whereas all the other studies used 100% RH, therefore requiring higher Nafion™ loading to make up for ohmic losses.

3.5.2. Case Study 2: Variable V_{FeNC}

In the second case study, an attempt was made to find the optimal phase compositions (i.e., void, ionomer and solid) while also incorporating the fact that the catalyst structure can be varied by adding pore former etc. To achieve this, thicknesses were varied at a fixed catalyst loading (m_{FeNC}) which effectively changes the phase fractions as well as the volumetric catalyst loading (V_{FeNC}) as described in Figure 3-3. Controlling the structure of the electrode at fixed catalyst loading can be achieved in many ways, for instance by adding a pore former in the catalyst ink to form more porous CL structure while reducing the electrode thickness. Or, a secondary processing step can be added such as pre-compressing the cathode catalyst layer sprayed on to the polymer electrolyte membrane if deemed necessary. At each catalyst loading, the thickness was varied from 10 to $200\ \mu\mathrm{m}$ with $10\ \mu\mathrm{m}$ increment. The Nafion™ loading was varied from 20 to 80% with an increment of 5%.

3.5.2.1. Operation at 0.76 V

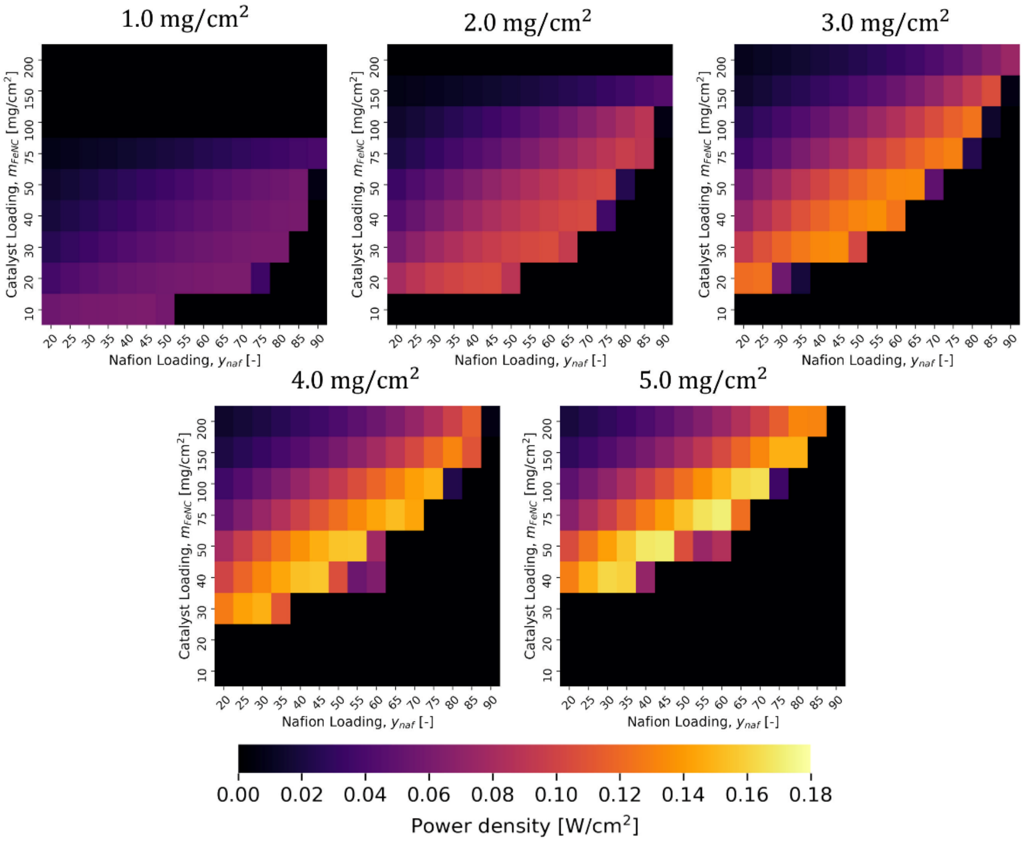

Figure 3-7 2-D visualization of power density with respect to the CL thickness and Nafion™ loading at fixed catalyst loading per unit volume at 0.76 V. Black pixels at low thickness region represents the area where the porosity drops below 0.

Figure 3-7 shows the power density plot with respect to catalyst and Nafion™ loading at 0.76 V. At all catalyst loading, the thinner electrode showed higher power density which is fully expected since it was found that, at 0.76 V, the performance was mostly dominated by the kinetics. The thinner electrode would mean more active catalyst in a given volume which improves the kinetics. Also, improved transport characteristics caused by the thickness reduction further improves the performance. However, at each thickness, there existed an optimum Nafion™ loading, which is again generally toward higher Nafion™ loading, beyond which increases in the Nafion™ loading had detrimental effect on the performance. Unlike case study 1, different catalyst loadings had different optimum Nafion™ loading, although the observed differences were small, with the exception of catalyst loading of $1.0\ \mathrm{mg/cm^2}$. Generally, the optimum Nafion™ loading ranged from 55 to 60% which is closer to what is reported throughout the literature. Table 3-6 summarizes the optimum thickness and Nafion™ loading at each catalyst loading and Figure 3-8 shows the maximum power density achieved at each catalyst loading.

Table 3-6 Optimum thickness and Nafion™ loading at each catalyst loading (0.76 V)

Catalyst Loading	Thickness	Nafion™ Loading	ε_s	ε_n	ε_v	Power Density @ 0.76 V
$[\mathrm{mg/cm^2}]$	$[\mu\mathrm{m}]$	$[-]$	$[-]$	$[-]$	$[-]$	$[\mathrm{W/cm^2}]$
1.0	10	0.40	0.430	0.333	0.237	0.06138
2.0	30	0.60	0.287	0.500	0.213	0.10480
3.0	40	0.55	0.322	0.458	0.219	0.13535
4.0	50	0.55	0.344	0.489	0.167	0.15542
5.0	75	0.60	0.287	0.500	0.213	0.17155

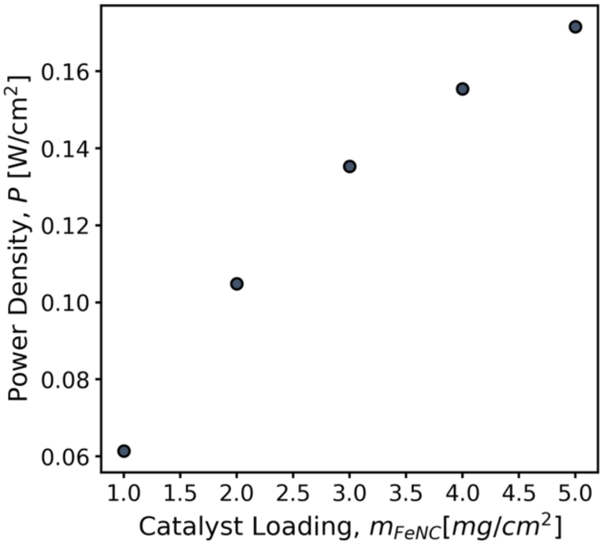

Figure 3-8 Maximum power density at each catalyst loading (0.76 V)

As it was seen with the first case study, no optimum catalyst loading was found within the studied range. Higher catalyst loading resulted in higher power density.

3.5.2.2. Operation at 0.60 V

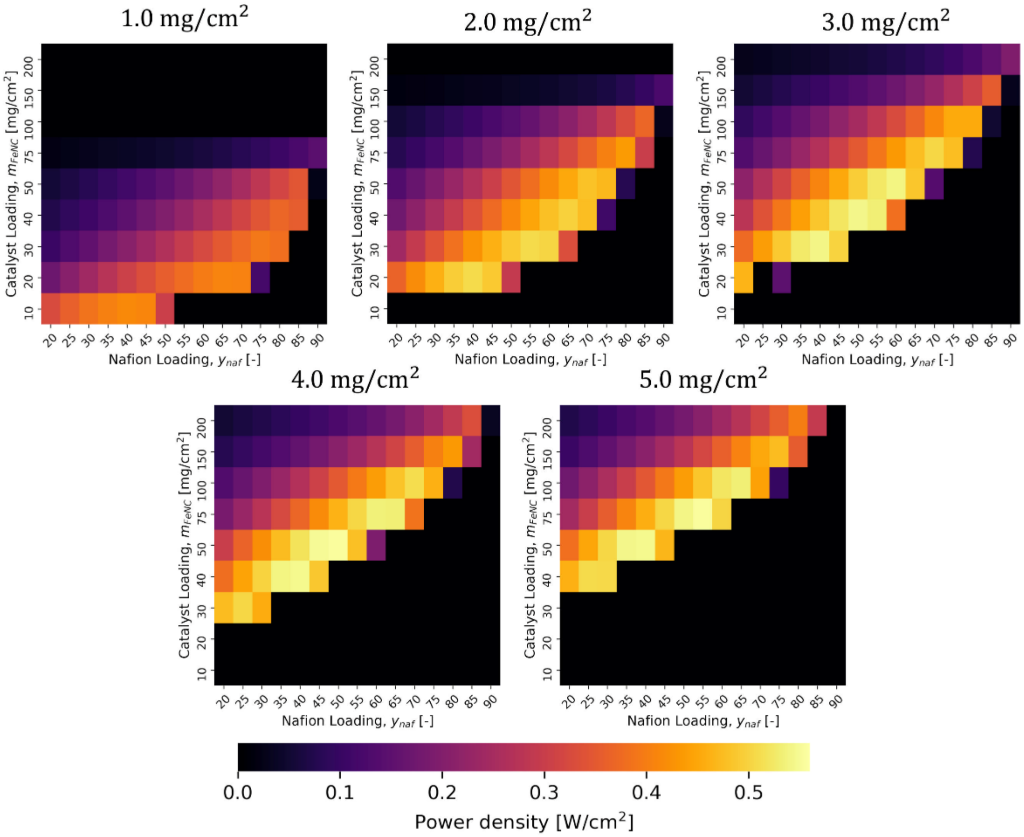

Figure 3-9 2-D visualization of power density with respect to the CL thickness and Nafion™ loading at fixed catalyst loading per unit volume at 0.60 V. Black pixels at low thickness region represents the area where the porosity drops below 0.

Figure 3-9 shows the power density plot with respect to catalyst and Nafion™ loading at 0.60 V. A similar trend compared to 0.76 V operation was observed. This is also expected since thinner electrodes improve both kinetics and transport characteristics until they become so thin that there is not enough porosity for gas phase transport. Table 3-7 summarizes the optimum thickness and Nafion™ loading at each catalyst loading and Figure 3-10 shows the maximum power density achieved at each catalyst loading.

Table 3-7 Optimum thickness and Nafion™ loading at each catalyst loading (0.60 V)

Catalyst Loading	Thickness	Nafion™ Loading	ε_s	ε_n	ε_v	Power Density @ 0.76 V
$[\mathrm{mg/cm^2}]$	$[\mu\mathrm{m}]$	$[-]$	$[-]$	$[-]$	$[-]$	$[\mathrm{W/cm^2}]$
1.0	10	0.40	0.430	0.333	0.237	0.41440
2.0	20	0.40	0.430	0.333	0.237	0.50860
3.0	40	0.50	0.322	0.375	0.303	0.54420
4.0	50	0.50	0.344	0.400	0.256	0.55448
5.0	75	0.55	0.287	0.333	0.380	0.55468

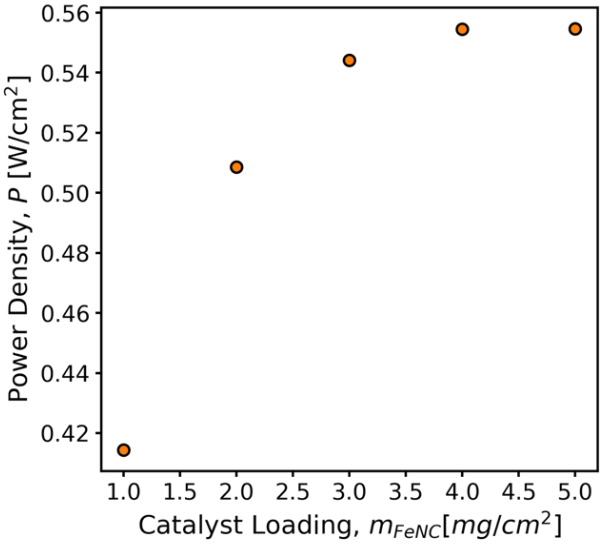

Figure 3-10 Maximum power density at each catalyst loading (0.60 V)

At 0.60 V, the maximum achievable power density started to decay from $3.0\ \mathrm{mg/cm^2}$. The increase in the power density from $3.0\ \mathrm{mg/cm^2}$ to $4.0\ \mathrm{mg/cm^2}$ was less than 2% after optimization of the thickness and Nafion™ loading. This agrees with the findings of the first case study where only a minimal performance improvement was observed by adding catalyst beyond $3.0\ \mathrm{mg/cm^2}$.

To further investigate the structure-performance relationship, the power density with respect to porosity and Nafion™ volume fraction is plotted in Figure 3-11 where Figure 3-11(a) is the power density scatter plot at 0.76 V and Figure 3-11(b) is the power density scatter plot at 0.60 V.

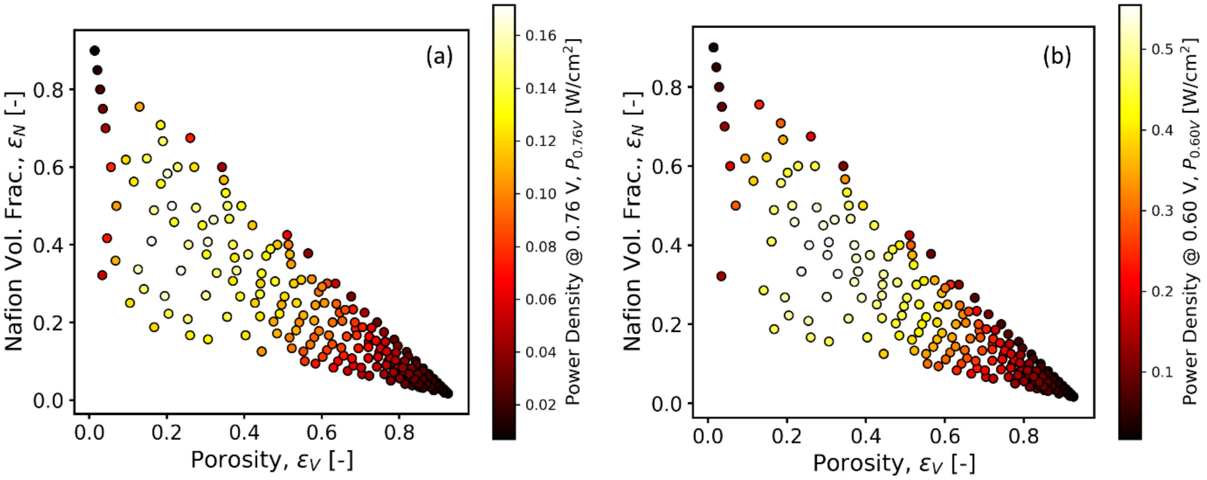

Figure 3-11 Scatter plot of power density with respect to porosity and ionomer volume fraction (a) at 0.76 V and (b) at 0.60 V.

From Figure 3-11, it can be visually observed that there exists an optimum phase composition, indicated by the clusters of white-colored markers. As expected, at either extreme (i.e., either high Nafion™ volume fraction or high porosity), the power densities appear to be the lowest with dark circles. Also, generally speaking, the power densities were low at high porosity region which is expected since both 0.76 V and 0.60 V are not in the mass transport regime. The key difference between 0.76 V and 0.60 V is in the optimum phase composition. For 0.76 V, the optimum combination is approximately 20% porosity and 45% ionomer phase fraction whereas for 0.60 V, the optimum combination is around 30% porosity and 35% ionomer volume fraction. As the regime is transitioning from the kinetic to the ohmic by changing the cell voltage from 0.76 V to 0.60 V, the optimum phase composition shifted. Slightly higher porosity and lower ionomer volume fraction was favored at 0.60 V to compensate for lower reactant concentration due to due to the impact of mass transfer resistance in the pore. For further clarification, power density was plotted against porosity and ionomer volume fraction at 0.76 V (Figure 3-12(a, b)) and at 0.60 V (Figure 3-12(c, d)). From Figure 3-12, it is evident that the porosity at which the max power density occurs shifts toward the higher porosity from 0.76 V to 0.60 V whereas for the ionomer volume fraction it is the other way around. Note that the optimum porosity and Nafion™ volume fraction were wide plateaus rather than sharp peaks. At 0.76 V, the plateaus were at 15 – 25% and 30 – 60% for porosity and Nafion™, respectively. At 0.60 V, the plateaus were at 25 – 35% and 30 – 50% for porosity and Nafion™, respectively.

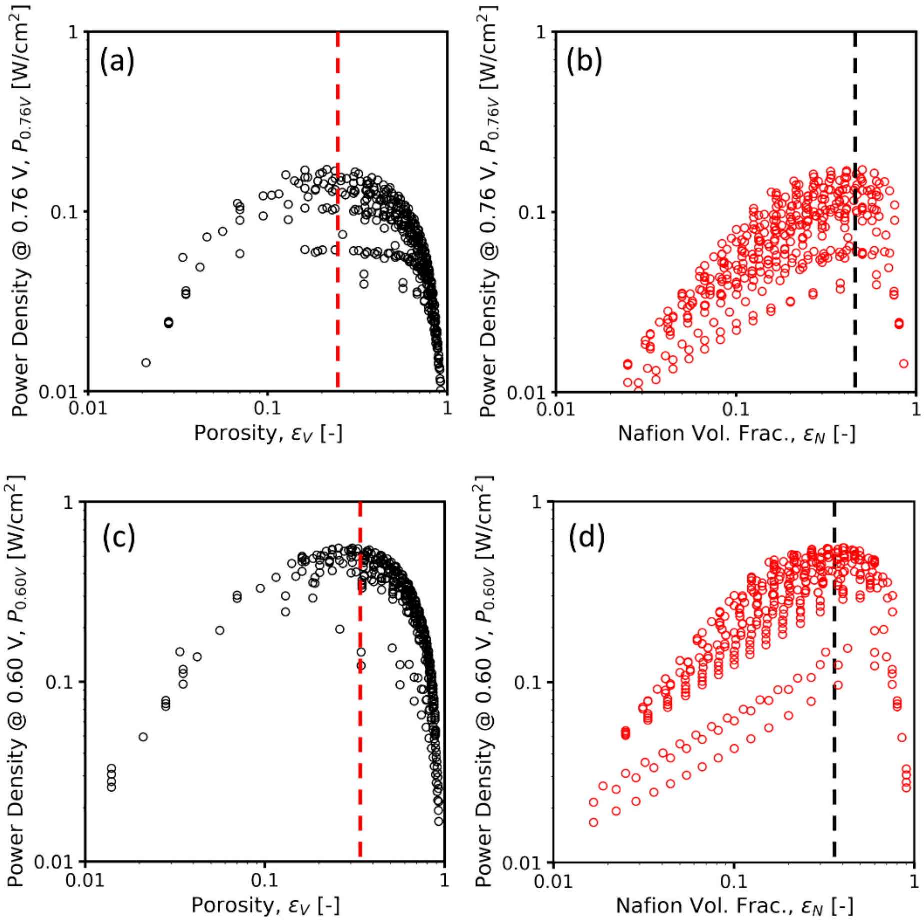

Figure 3-12 Power densities plotted against (a) porosity at 0.76 V, (b) Nafion™ volume fraction at 0.76 V (c) porosity at 0.60 V and (d) Nafion™ volume fraction at 0.60 V. Dashed lines were placed near the maximum power density for each plot.

3.6. Conclusion

In the present study, the effect of catalyst layer composition on the performance of the non-PGM cathode catalyst layer was investigated using a single-phase, non-isothermal model under practical operating condition of 70% RH, 150 kPa and 0.76 V or 0.60 V. 0.76 V is the target set out by the US Department of Energy whereas 0.60 V is the typical operating voltage in the automotive application. Parametric studies were performed by adjusting catalyst loading, Nafion™ loading and thicknesses. For catalyst loading, values up to $6.0\,\mathrm{mg/cm^2}$ were investigated and Nafion™ loading was varied within 10 – 90%. Thicknesses were varied from 10 to $200\,\mu$m. The model was implemented in an open-source fuel cell simulation framework (OpenFCST).

Two different cases were investigated. The first case study assumed fixed volumetric catalyst loading at $400\,\mathrm{mg/cm^3}$ meaning the thickness linearly increases with the catalyst loading per unit area (m_{FeNC}). In this case study, it was found that, at 0.76 V, the performance was dominated by the kinetics and ohmic loss. The performance increased with increasing catalyst loading as well as Nafion™ loading within the studied range. At 0.60 V, the optimum catalyst loading was found to be $4.0\,\mathrm{mg/cm^2}$, however, there was only minimal improvement in the performance from $3.0\,\mathrm{mg/cm^2}$ to $4.0\,\mathrm{mg/cm^2}$. At 0.60 V, optimum Nafion™ loading was found to be 70% for all catalyst loadings which is higher than the usual optimum Nafion™ loading reported in other studies.[105,28,30,45] This was attributed to the fact that most published works used fully humidified oxygen reactant which maximizes the proton conductivity but, is more prone to water flooding. At 70% RH, the non-PGM CCL is less prone to water flooding, however, higher Nafion™ loading was necessary to make up for lower proton conductivity.

In the second case study, the volumetric catalyst loading was varied at a fixed catalyst loading per unit area. This means that at fixed catalyst loading, the CCL can have different thicknesses and in turn different porosities and ionomer volume fractions. The primary purpose of this case study was to investigate which combination of porosity and ionomer volume fraction would give the best performance given that layer morphologies can be adjusted during production. Generally, at all catalyst loading, thinner layer resulted in better performance until the layer was too thin that the porosity was too small. This was expected since condensing a fixed catalyst loading per unit area will increase the catalyst loading per unit volume. Also, the thinner layer would improve the transport characteristics leading to better performance. It was again found in the second case study that the optimum catalyst loading was at $4.0\ \mathrm{mg/cm^2}$, but with minimal improvement beyond $3.0\ \mathrm{mg/cm^2}$. Due to thinner electrodes, the required Nafion™ loading was relieved from 70% in the first case study to approximately 50 to 60% Nafion™ loading in the second case. This is much closer to what is reported to be the optimum Nafion™ loading in a lot of studies.[28,30,45,105] There existed optimum porosity as well as ionomer volume fraction. At 0.76 V, it was approximately 20% and 45% for porosity and ionomer volume fraction, respectively. At 0.60 V, 30% and 35% for porosity and ionomer volume fraction, respectively. The difference between the optimum values are due to the shift in the operating regime. 0.76 V is closer to the kinetic regime where the amount of catalyst and ionomer are more important whereas mass transport effects start to occur at 0.60 V therefore requiring slightly higher porosity and less ionomer. In summary, the catalyst loading of $4.0\ \mathrm{mg/cm^2}$ and Nafion™ loading of 55% with the thickness of $50\ \mu\mathrm{m}$ was found to perform the best at the rated voltage set by the US DOE (i.e., 0.76 V), but it was also found that slightly less Nafion™ loading (i.e., 50%) was better for practical operation at 0.60 V.

Chapter 4 Measuring Effective Diffusivity in Porous Media with a Gasket-free Radial Arrangement

4.1. Preface

The ability to characterize the effective diffusivity of the porous electrode of the fuel cell is crucial in designing better catalyst layer. There are several techniques that have successfully probed the in-plane and through-plane effective diffusivities of GDL, however, CLs impose further challenge due to their thinness and non-self-supporting structure. In the present study, as a step toward designing better non-PGM catalyst layer, a novel method for measuring the in-plane effective diffusivity of thin porous materials was developed. The developed technique is particularly appealing for ultra-thin materials such as CLs because it does not require a gasket. The developed technique was thoroughly validated by measuring the binary diffusion coefficient of open space, and the effective diffusivity of classical porous media, namely a pack of spheres.

4.2. Abstract

A simple technique for measuring the effective diffusivity, and ultimately tortuosity, in porous media is presented. The method uses a custom-built apparatus, based on a radial geometry, which eliminates the need for any gaskets to seal the edge of the sample. This makes it particularly well suited for thin media such as films and layers. The experiment is based on the transient response of the oxygen concentration at the center of the sample as oxygen diffuses into an initially nitrogen filled domain from the sample perimeter. The analytical solution of Fick's law for transient diffusion in cylindrical coordinates is fitted to the measured oxygen concentration profile to obtain the effective diffusivity. To validate the method, binary diffusion

coefficients of N_2-Air system were measured, and the results show a close match and are consistent for a range of experimental parameters like flow rate and domain thickness. The classical study of diffusion in porous media based on sphere packing is revisited for further validation of the technique. The results show good agreement to the well-known Bruggeman correlation as well as to the experimental values reported in the literature. The new technique is further applied to other types of thin porous materials and the results indicate that the Bruggeman correlation generally overestimates the effective diffusivity of non-sphere packing.

4.3. Introduction

The effective diffusivity in thin porous media is of great importance in modern engineering applications. Energy conversion and storage devices such as fuel cells[130–133] and metal-air batteries[134] as well as water desalination[135,136], filtration and separation[137], and gas sensors[138,139] are just a few examples. In many of these applications, the performance of the device is highly dependent on the diffusive transport; therefore, accurate ex-situ characterization is crucial to producing high performing engineered porous media. Unfortunately, there isn't yet a well-established, easy to apply and standardized method for characterizing the effective diffusivity in thin porous media due to the geometrical constraints imposed by their thinness.

Despite the challenge, there has been numerous attempts to develop a technique for measuring the effective diffusivity in thin porous media. The Loschmidt apparatus is a classic technique[140] for measuring binary diffusion coefficient where two gases of interest are filled in two separate compartments. The compartments are initially separated by closing the connection, then the connection is opened to allow gases to diffuse into one another. The transient gas concentrations are measured as a function of time to obtain the binary diffusion coefficient. Astrath et al.[141] modified the original Loschmidt cell by measuring the gas concentration as a function of time at a fixed position, thereby measuring the diffusivity transiently. Zamel et al.[78] adopted this method and modified it even further to study the effective diffusion in gas diffusion layers (GDL) in proton exchange membrane fuel cells (PEMFC). In their work, two gas compartments were separated by a GDL, which has a thickness range from 200 – 400 μm, effectively adding resistance to the bulk diffusion. The delay induced by the porous sample can be used to extract the effective diffusivity. This technique was subsequently used to characterize the effective diffusivity in the catalyst layer in PEMFC, though with considerably more complexity.[142] A significant limitation of the modified Loschmidt cell generally is that it requires the sample to be self-standing which might not be possible in some cases. Also, it is questionable whether such thin materials will add noticeable resistance to the bulk diffusion process. Another classical measurement technique is the Wicke-Kallenbach (W-K) diffusion cell.[143] In the W-K type cells, a porous sample is placed between two gas flow channels where two different types of gases flow in each channel. The concentration gradient across the porous sample drives the gas diffusion into the porous sample. Secanell and co-workers[62,76,82] adopted the W-K cell and used it to measure the effective diffusivity in GDLs. The modified W-K cell was also used by workers at General Motors to measure the effective diffusivity in the catalyst layer (CL) of PEMFC.[86] The main drawbacks of the W-K type technique are that careful control of the gas flow rate and extremely accurate measurement of the gas concentration is required since the effective diffusivity is extracted based on the mass balance around the diffusion cell. Also, because materials such as GDLs and CLs are so thin, even a slight pressure difference can cause significant convective flow. An alternative approach to measuring diffusivity was used by Rashapov et al.[69] where they developed a simple technique based on the transient diffusion of oxygen into a porous sample initially filled with nitrogen. The concentration of oxygen is measured at a fixed position as a function of time and the analytical solution of Fick's second law is fitted to the experimental data to extract the effective diffusivity. This technique was subsequently applied to dry[70] and partially saturated[79] GDLs. Although quite convenient, this technique required application of sealing material on the edges to prevent diffusion and satisfy the boundary condition of the analytical solution of 1-D diffusion in a planar sheet. This can be problematic for thinner materials such as CL. Perhaps the most well-established method for measuring effective diffusivity in porous media is to flood the pore space with liquid brine and measure the ionic conductivity. The analogy between Ohm's law and Fick's law is used to indirectly obtain formation factor. This is generally not applicable in many porous electrodes of interest as they are often made with conductive materials, which complicates the interpretation and implementation of these experiments considerably.[66,67] It is also quite difficult to ensure that materials are fully saturated with brine, especially if they've been given a hydrophobic treatment of some sort.[144]

In this work, a novel and simple technique for measuring the effective diffusivity in thin porous media is developed. This method is a variation to the earlier work done by Rashapov et al.,[69] but adopting a radial geometry instead, which has several advantages: 1) no sealing is required, therefore it is easily applicable even to ultrathin materials, 2) because no seal is required there is no need to apply pressure to the sample holder which might damage or deform the sample, and 3) the measurement time is only on the order of minutes. The newly developed method was thoroughly validated and applied to classical porous media such as sphere packing.

4.4. Experimental Methods

The radial diffusivity apparatus consists of two specially designed sample mounts or pedestals (top and bottom), a cylindrical chamber for gas flow and a fiber optic O_2 sensor. All components of the apparatus were built in-house except for the optical oxygen sensor which was purchased from Pyro-Science (Aachen, Germany). The O_2 sensor used in this study was ultra-fast response sensor (OXR430-UHS) with the response time less than 0.3 seconds according to the manufacturer and verified in the lab.

4.4.1. Diffusion Pedestals

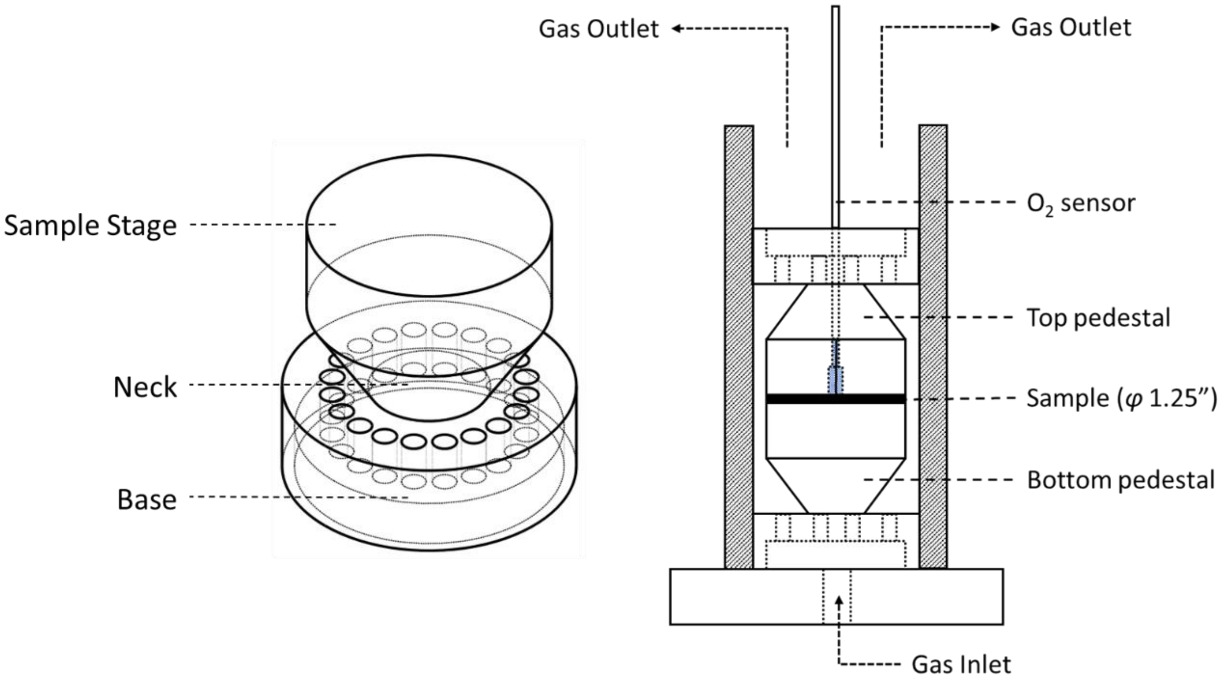

Figure 4-1 (left) Pedestal design for radial diffusivity apparatus (right) Radial diffusivity apparatus system setup

The top and bottom pedestals were designed and machined as shown in Figure 4-1(left). The O_2 sensor probe (a fiber optic strand of 0.43 mm diameter) was positioned through the center of the top pedestal and the tip of the sensor was aligned with the surface of the top pedestal. A hole for the sensor was drilled in two stages where a smaller hole that matched the sensor diameter was first made and subsequently a larger hole that was filled with silicone elastomer to seal around the fiber. Two levels of holes were necessary as friction fit of the sensor with just a single hole resulted in a significant amount leakage into the sample due to gaps between the hole itself and the sensor, which led to error in the measurement. The base of the sample mounts was designed with a sliding fit inside the cylindrical chamber to guide and position them, while the pedestal portion was slightly smaller. This created a small gap around the perimeter of the sample stage for N_2 gas to flow by the sample perimeter with high velocity. The neck of the pedestal was designed with an angle so that the gas is smoothly supplied to the sample perimeter.

4.4.2. System Setup and Test Procedure

The entire system setup in shown in Figure 4-1(right). A porous sample of 1.25-inch in diameter was placed on the sample stage of the bottom pedestal and they were placed inside the cylindrical chamber. The top pedestal was then slid into the chamber and gently onto of the sample. N_2 gas was supplied from the bottom and distributed to the system through the holes on the pedestal and exited through the top.

Prior to each experiment, the oxygen sensor was calibrated according to the local environmental conditions (i.e. temperature, pressure, humidity) to ensure O_2 reading of 20.9%. Temperature and pressure were measured externally, and humidity was measured internally by the O_2 sensor electronics. The porous sample was placed on the bottom pedestal and left under the ambient condition for at least half an hour to establish initial oxygen concentration of 20.9% everywhere within the porous domain.

The data logging is initiated at $t = 0$ and approximately after 5 seconds, N_2 supply was turned on to allow the flow N_2 gas past the sample perimeter. N_2 gas was supplied at high flow rate to ensure nearly instantaneous change in the boundary condition. The depletion of the oxygen concentration at the center of the sample was measured and recorded as a function of time. After a constant value of 0% oxygen was recorded for at least 20 seconds, data logging was stopped.

4.4.3. Data Analysis

The effective diffusion coefficient was extracted by fitting the analytical solution of the Fick's second law for cylindrical coordinates to the oxygen concentration profile obtained experimentally. Assuming diffusion is everywhere radial within the sample, the Fick's law of transient diffusion is written as:

$$\frac{\partial c_i}{\partial t} = \frac{1}{r}\frac{\partial}{\partial r}\left(rD\frac{\partial c_i}{\partial r}\right) \qquad [4\text{-}1]$$

where c_i is the concentration of species i, r is the spatial coordinate along the concentration gradient, t is time and D is the diffusion coefficient. Eq. [4-1] can be solved analytically with the following boundary conditions:

$$c(t) = \begin{cases} c_0, & r = R, \quad t \geq 0 \\ c_1, & 0 < r < R, \quad t = 0 \end{cases} \qquad [4\text{-}2]$$

where $c(t)$ is the concentration as a function of time at a fixed position r, R is the radius of the sample, c_0 is the constant surface concentration and c_1 is the initial concentration distribution of the species within the sample. The analytical solution for such case is provided by Crank[145]:

$$\frac{c(t) - c_1}{c_0 - c_1} = 1 - \frac{2}{R}\sum_{n=1}^{\infty}\frac{\exp(-D\alpha_n^2 t)\,J_0(\alpha_n r)}{\alpha_n J_1(\alpha_n R)} \qquad [4\text{-}3]$$

where $J_0(r)$ and $J_1(r)$ are the Bessel functions of the first kind of order 0 and 1, respectively. α_n is defined in Eq. [4-4] where $\alpha_n R$ are the nth root of:

$$J_0(\alpha_n R) = 0 \qquad [4\text{-}4]$$

After obtaining the oxygen concentration profile, $c(t)$, the only unknown variable in Eq. [4-3] is the diffusion coefficient, D. Therefore, Eq. [4-3] can be fitted to the experimental data by the method of least squares.

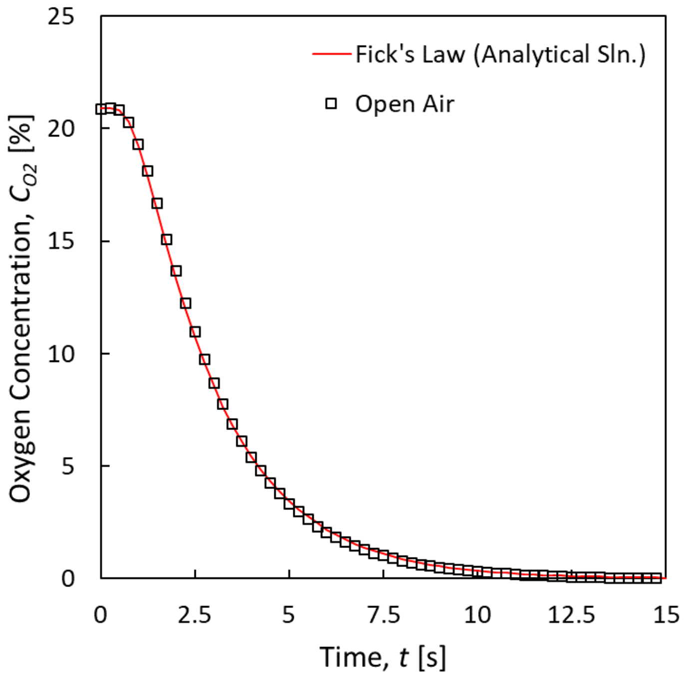

Figure 4-2 The analytical solution of Fick's second law fitted to transient oxygen concentration profile of an open air

Figure 4-2 shows an example of the above analytical solution fitted to the experimental data for N_2 diffusion in open air. As evident from Figure 4-2, the analytical solution fits well to the experimental data. It is also noteworthy that for open air the steady state is expected to be reached within 15 seconds. The rapid experimental time can be beneficial especially for samples with lower porosity or smaller pore sizes where the diffusion takes place at a much slower rate, but it does necessitate the use of a high response time oxygen probe.

It should also be pointed out that the effective diffusivity obtained from the above procedure is not in the same sense as the one most widely used:

$$D_i^{eff} = (\varepsilon/\tau)D_i \qquad [4\text{-}5]$$

where D_i^{eff} is the effective diffusivity in porous media, D_i is the bulk diffusivity of a binary system, ε is the porosity and τ is the tortuosity of the porous sample.

This can be explained by performing a transient mass balance around the porous media. Assuming incompressible fluid flow with no convection and no reaction, the continuity equation in porous media can be expressed as[146]:

$$\varepsilon \frac{\partial c_i}{\partial t} = D_i^{eff} \nabla^2 c_i \qquad [4\text{-}6]$$

In Eq. [4-6], ε is multiplied to the transient term (LHS) since, in porous media, the volume where gas species can reside is decreased by a factor of ε. In other words, c_i is defined as $\mathrm{mol/m^3}$ of sample, but the gas molecules are confined to the pore space so the oxygen concentration measurement is $\mathrm{mol/m^3}$ of void space, thus the measured concentration must be multiplied by ε for application in Eq. [4-6]. On the RHS, the flux is also decreased by the presence of solid phase which is already embedded in the definition of the effective diffusivity given by Eq. [4-5]. Therefore, substituting Eq. [4-5] into Eq. [4-6] effectively cancels out ε on both sides, resulting in:

$$\frac{\partial c_i}{\partial t} = \left(\frac{D_i}{\tau}\right) \cdot \nabla^2 c_i \qquad [4\text{-}7]$$

This means that the *effective diffusivity* obtained from the current technique should be interpreted as $(1/\tau)D_i$, not as $(\varepsilon/\tau)D_i$. This is actually one of the interesting aspects of the current method where tortuosity, τ, is measured directly, independent of the porosity.

4.4.4. Sample Preparation

Three types of porous medium were considered for testing: 1) monodispersed random sphere packing, 2) polydispersed agglomerated sphere packing and 3) quartz frits with non-ideal pore shape. Tested samples are summarized in Table 4-1. SEM Images of each sample are shown in Figure 4-3.

Table 4-1 Summary of Porous Samples Tested for Diffusivity Measurement

Category	Material	Size [µm]	Porosity [-]
Monodispersed Random Sphere	Glass	100	0.39*
		1000	0.40*
	Stainless Steel	3000	0.46*
		2500	0.44*
		1500	0.45*
		1000	0.45*
	Silica	25	0.46*
Polydispersed Agglomerated Sphere	Alumina	3.5 – 15	0.79*
		0.3 – 0.8	0.73*
Quartz Frits	Quartz frits	200 – 300§	0.627**
		40 – 90§	0.452**
		4 – 15§	0.412**

* tapped density
** buoyancy technique[147]
§ given by manufacturer

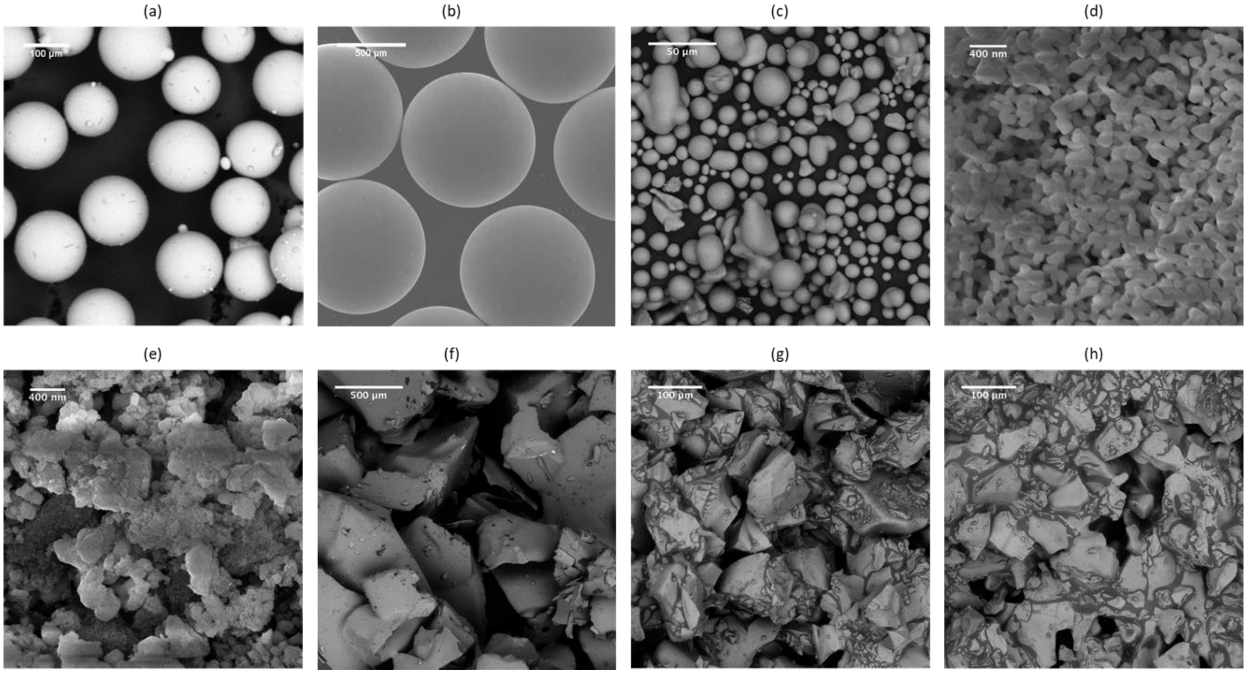

Figure 4-3 SEM Images of (a) 0.1 mm glass beads, (b) 1 mm stainless steel balls, (c) 25 µm spherical SiO_2, (d) 3.5-15 µm Al_2O_3, (e) 0.3-0.8 µm Al_2O_3, (f) quartz frits with pore size 200 – 300 µm, (g) quartz frits with pore size 40 – 90 µm, (h) quartz frits with pore size 4 – 15 µm

Due to the nature of sphere particles not being able to form a rigid structure, a special method for preparing porous disc was adopted. For glass, silica and alumina materials, they were first dispersed in water. Then, the dispersion was filtered through a membrane with the average pore size of 0.03 µm. The dispersion was stirred as they were being poured into the filtration apparatus to achieve a “random” packing of sphere particles. The filtered deposits on the membrane were cut into 1.25-inch diameter disc and placed onto the bottom pedestal. The membrane was carefully peeled off and the sample was dried at 80°C until constant mass was measured.

For stainless steel (440C type) balls, a sheet of flexible magnet was purchased. Flexible magnet was cut into 1.25-in diameter disc and was attached to the sample stage of the bottom pedestal. The stainless-steel balls were then poured onto the flexible magnet in a packing die made in-house and gently packed, just enough to make the top surface flat.

30 mm disc of quartz frits of various porosities (Table 4-1) were purchased from Technical Glass Products and tested as-received since they were already made into a disc shape.

4.4.5. Porosity Measurement

The effective diffusivity is generally a decreasing function of porosity, therefore porosities of each sample tested were measured. The method of measuring porosity was also altered according to the nature of the sample. For monodispersed spheres (glass, stainless steel and silica) and polydispersed agglomerated spherical particles (alumina), “tapped density” was measured and it was used to calculate porosity. Particles were measured to a certain weight and they were placed in a 10-mL graduated cylinder. The graduated cylinder was repeatedly tapped until there was no more volume change. Tapped density of the particles was calculated using Eq. [4-8].

$$\rho_{tapped} = \frac{m_s}{V_{tapped}} \qquad [4\text{-}8]$$

where ρ_{tapped} is the tapped density of the particles, m_s is the mass of the solid and V_{tapped} is the final tapped volume. This process mimicked the sample preparation process as filtration of randomly dispersed particles will result in "a tight random" packing of the particles. The porosity of the sample was calculated using the following equation:

$$\varepsilon = 1 - \frac{\rho_{tapped}}{\rho_s} \tag{4-9}$$

where ε is the porosity of the sample from (0 – 1) and ρ_s is the density of the pure solid. Since, bulk densities of the solids tested are well known, the porosities can also be calculated.

Porosities of quartz frits were measured using the buoyancy technique.[147] Thickness of the quartz frits were measured with a micrometer with 1 µm resolution and ± 0.1 µm accuracy. The sample was then weighed both dry and submerged in highly wetting silicone oil (5 cSt). Implementing Archimedes' principle allowed the determination of the pure solid density and ultimately the porosity of the sample.

4.4.6. Validation with Open Air

Validity of the radial diffusivity apparatus was analyzed by measuring bulk diffusivity of nitrogen-air (N_2-Air) binary system with no sample present between the pedestals, only an empty gap. To ensure that the diffusion was the only mode of mass transport during the experiment, bulk diffusivity measurement was performed with different gap distances between the pedestals and with different N_2 gas flow rates.

The results for binary diffusion coefficients of N_2-Air system with various gap distance is shown in Figure 4-4(left). In Figure 4-4(left), the red line indicates the theoretical bulk diffusion coefficient of N_2-Air system estimated by the Chapman-Enskog equation [64]:

$$D_{ij} = \frac{0.00186 \cdot T^{3/2}}{P \cdot \sigma_{ij}^2 \cdot \Omega}\left(\frac{1}{M_i} + \frac{1}{M_j}\right)^{1/2} \qquad [4\text{-}10]$$

where D_{ij} is the binary diffusion coefficient of species i and j measured in cm^2/s, T is the temperature in Kelvin, P is the pressure in atmospheres, and M_i and M_j are the molecular weights of species i and j, respectively. σ_{ij} and Ω are Lennard-Jones potential parameters from the Chapman-Enskog theory where the values for various species are given elsewhere.[64]

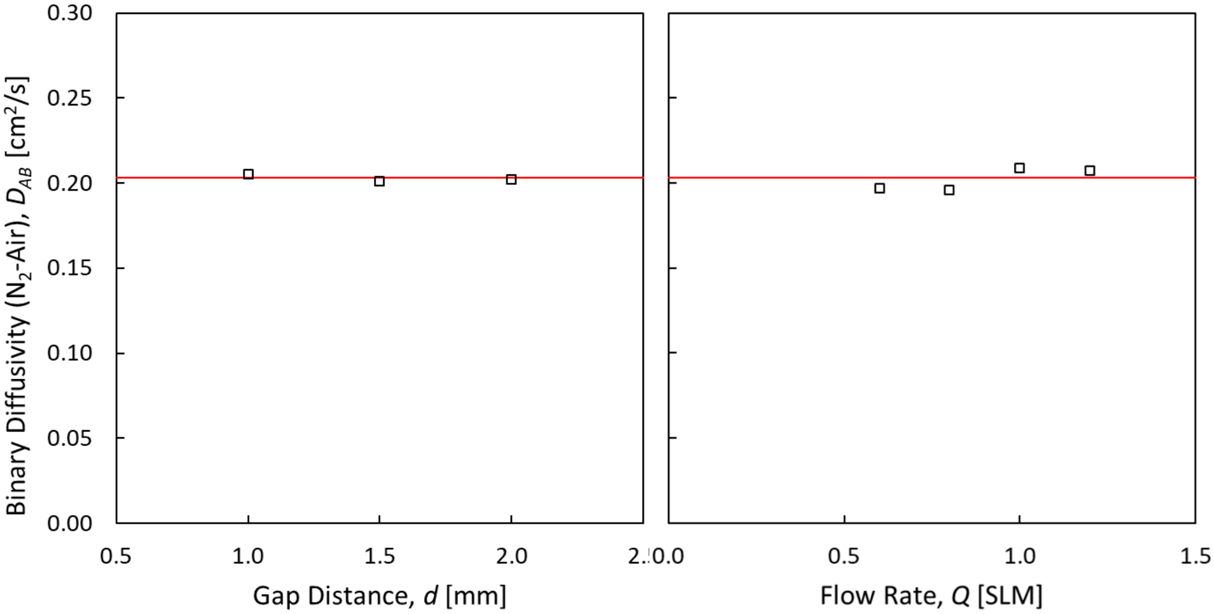

Figure 4-4 Diffusion coefficient of N_2-Air binary system measured with various gap distances (left) and various volumetric flow rates (right). The line indicates the prediction of the Chapman-Enskog equation given in Eq. [4-10]

The average of binary diffusion coefficients measured at different gap distances with the value of 0.203 cm^2/s and the deviation of 1.03%. Figure 4-4(right) shows the binary diffusion coefficients of N_2-Air system tested with various volumetric flow rates of N_2 gas. Again, in Figure 4-4(right), the red line shows the binary diffusion coefficient of N_2-Air estimated by the Chapman-Enskog theory. The average value was 0.202 cm^2/s with the deviation of 3.31%. The results indicate that the binary diffusion coefficient depends neither on the gap distance nor on the volumetric flow rates and confirms that the diffusion is the only mode of the mass transport in the experiments.

One of the challenges in designing a diffusivity experiment is keeping the boundary condition constant as oxygen diffusing out of the sample can result in the change in boundary condition. This problem was resolved by using the flow rate of 1500 sccm for N_2 gas. From Figure 4-2, for open air, the steady state is reached approximately 10 seconds after the boundary condition has been applied ($C_{O_2} = 0$). At the flow rate of 1500 sccm N_2, the total number of moles of N_2 entering the sample perimeter is 1.022×10^{-2} mol N_2. Assuming the bottom and the top pedestals are approximately 2 mm apart, there would be 1.35×10^{-5} mol O_2 and 5.12×10^{-5} mol N_2 within the open space initially. After approximately 10 seconds, all O_2 molecules would have diffused out of the open space and the balancing moles of N_2 would have diffused into the open space from the gas flow. Then, the gas flow leaving the top of the gap would have O_2 concentration of approximately 0.1% and N_2 concentration of 99.9%. The concentration change within the gas flow is minimal, therefore it is valid to assume the boundary conditions are constant throughout the experiment. This is also illustrated in Figure 4-5. The concentration change will be even lower for the thin engineered porous media since their thicknesses are generally within micrometer range. Also, the diffusion process is slower for the porous materials than it is for the bulk diffusion in the open space. High flow rate will not only change the boundary condition instantly, but also will flush away the trace amount of oxygen diffusing out of the sample immediately, effectively keeping the boundary condition constant.

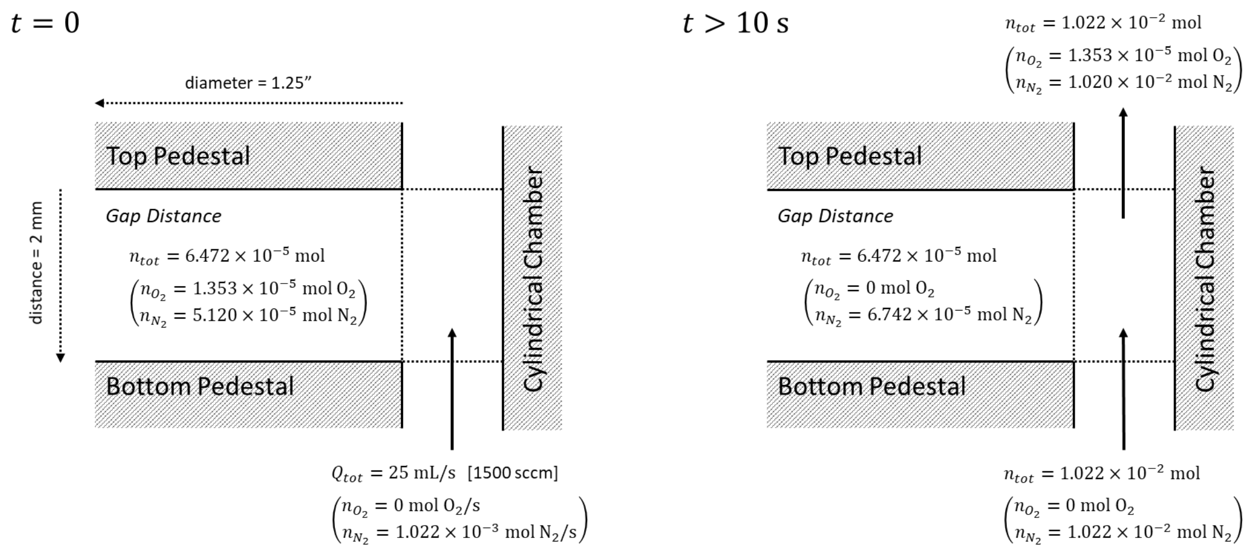

Figure 4-5 Illustration on justification of the constant boundary condition

4.5. Results and Discussion

The radial diffusivity apparatus was tested with various porous media with different pore geometries (i.e. shape and size). Spherical particles were extensively tested since sphere packings are the most well studied porous media experimentally and theoretically. Agglomerated spherical alumina packing and quartz frits were chosen to investigate the ability of the apparatus to measure porous media with other types of pore geometry.

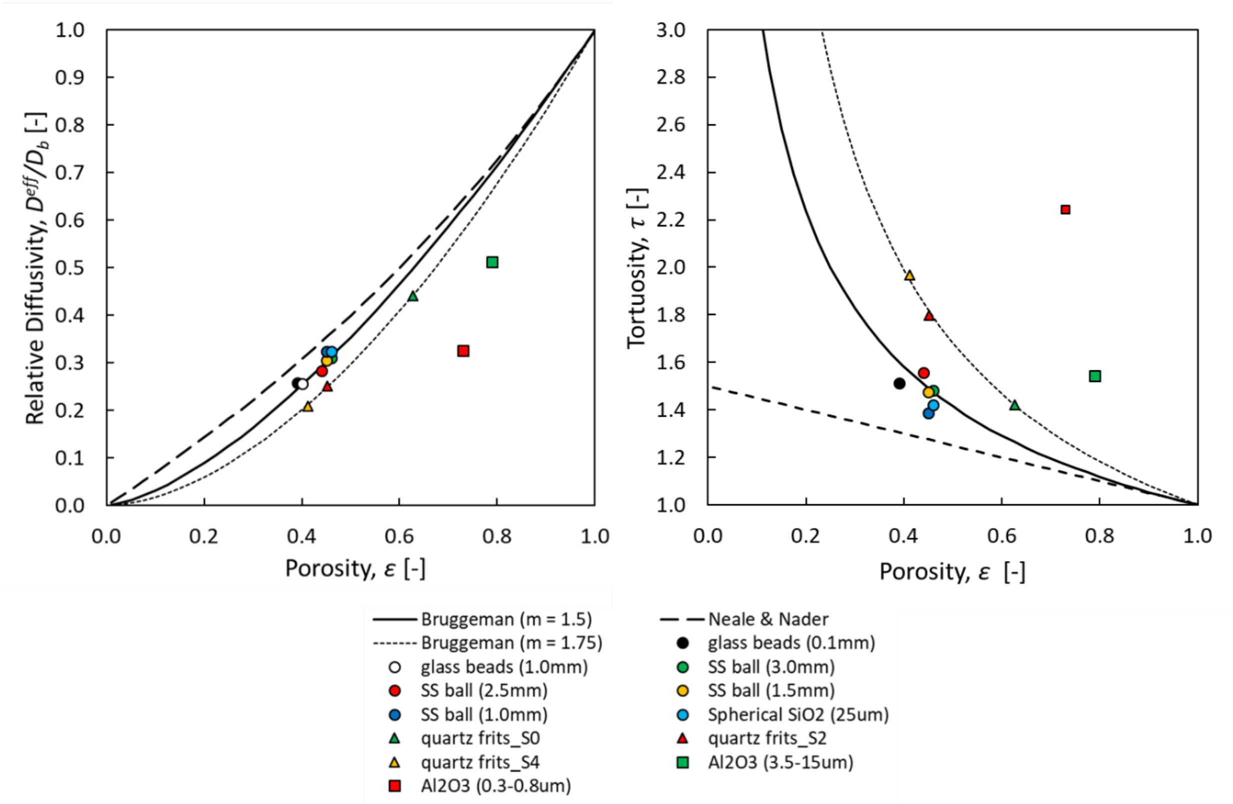

Figure 4-6 Relative diffusivity (left) and tortuosity (right) of porous media and comparison to the theoretical correlations. (Each data point is an average of three measurements. Error bar omitted for clarity)

Figure 4-6 shows the relative diffusivity $\left(D_i^{eff}/D_i\right)$ of the sphere packing with various sizes and materials. The experimental values were compared to the Bruggeman[148] and Neale and Nader[149] approximations. There are many published models for estimating the tortuosity factor of porous media, however, the Bruggeman and Neale and Nader were chosen because two correlations were specifically developed for random homogeneous isotropic sphere packing.

Although, the Bruggeman approximation is most commonly used to estimate the effective diffusivity, there are numerous reports where the model overestimates the effective diffusivity, especially for low porosity.[86,130,150,151] What is often overlooked is that the original equation derived by the Bruggeman is actually $D_i^{eff}/D_i = \varepsilon^{(1+n)/n}$, or simply $D_i^{eff}/D_i = \varepsilon^m$, where m (or n) is the shape factor. The most widely used form of the Bruggeman equation ($D_i^{eff}/D_i =$

$\varepsilon^{1.5}$) is a special instance of the Bruggeman's original derivation where the particle shape is spherical (m = 1.5).[148,151] It is evident from the previous works[152–154], as well as the present work, when assumptions of the approximation are satisfied (random, isotropic spheres), the tortuosity estimated by the Bruggeman agrees well with the experimental measurements. In many cases of interest to engineers, however, the shape of the particles is much more complex than spheres, hence the Bruggeman equation must be used with caution. Gaseous diffusion in glass sphere packing of various particle sizes was experimentally investigated by Currie.[153] Comparison between the values obtained by Currie and the present study is illustrated in Figure 4-7. The values lie in the higher porosity region are stainless steel sphere packing. For glass sphere packing, Currie and the present study showed similar porosity as well as the relative diffusivity. Generally, the tortuosity in both studies either followed the Bruggeman correlation or were just slightly underestimated by it.

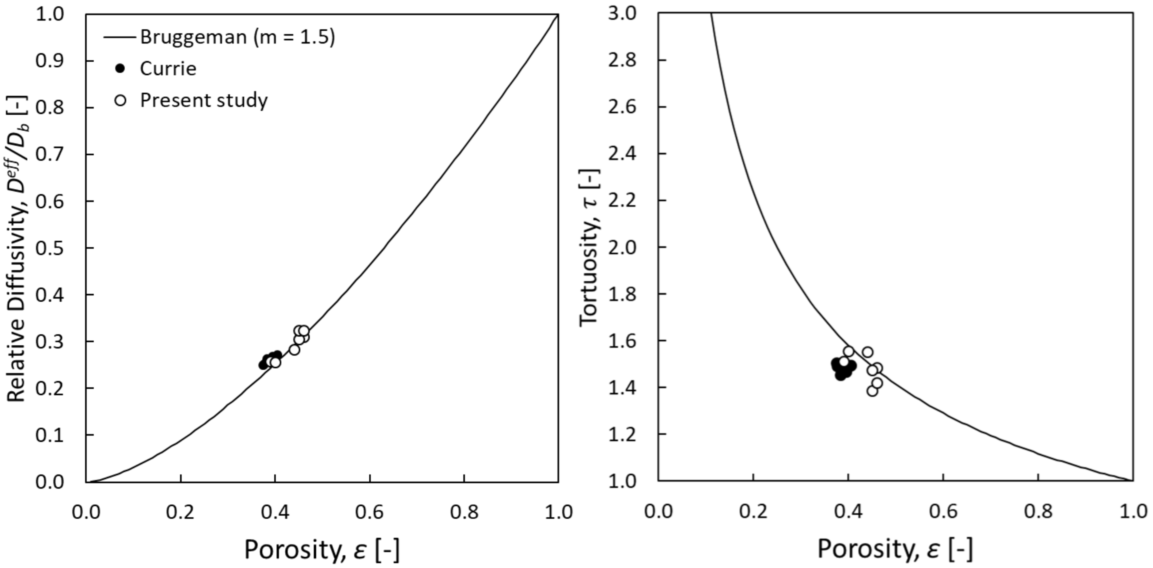

Figure 4-7 Comparison of the relative diffusivity (left) and the tortuosity (right) between Currie[153] and the present study (m = 1.5)

The tortuosity of the quartz frits had higher values than what the Bruggeman correlation predicted (Figure 4-6). This problem is commonly encountered when the particle shape of the porous media deviates from the ideal spherical shape. This was also seen from Currie's work where higher Bruggeman exponents were obtained for most porous media. Currie attempted to calculate the relative surface area (S_γ) of the tested materials where S_γ was defined as the ratio of the surface area of the material to that of a sphere with equal volume. Although, no mathematical description was given, the experimental data showed a general trend where with increasing relative surface area, the shape factor increased.[153] Some works claim that the deviation is attributed the anisotropy of the porous structure[155], however it is still unclear as to why such behavior is observed. An attempt was made to obtain the Bruggeman exponent that fits the quartz frits data by least-square method, and m = 1.75 was obtained.

Packing of the agglomerated spherical alumina particles exhibited effective diffusion behavior well below the Bruggeman correlation. The effect is even more dramatic than that of the quartz frits because Knudsen diffusion is expected to play a significant role due to small pore sizes of the alumina packings. From Figure 4-6, it can be seen that the relative diffusivity of alumina packing with particle size 0.3 – 0.8 µm deviates even more from the Bruggeman than the alumina packing with particle size 3.5 – 15 µm does since alumina packing with 0.3 – 0.8 µm particles are expected to have smaller pore size, hence a stronger Knudsen effect was expected. Pore size distributions of each Al_2O_3 particle size were roughly estimated from the SEM images and the result is shown in Figure 4-8. As expected, the pore size distribution of 0.3 – 0.8 µm alumina packing falls in the lower region with the average pore diameter of approximately 31 nm. 3.5 – 15 µm alumina packing had larger and broader pore size distribution with the average pore diameter of around 103 nm. Fitting the Bruggeman equation here is nonsensical since the diffusion in alumina packing is affected by the pore size. In Bruggeman's equation, pore size effect was never considered therefore should not be used outside of the molecular diffusion regime. Nonetheless the experimental data obtained by the present experiment are self-consistent and suggest that the tool can be used for effective diffusivity determination in such nanoporous media. Although, no further analysis in Knudsen effect was not carried out in this chapter, it is more closely looked at in the next chapter with the non-PGM catalyst layers which are also nanoporous.

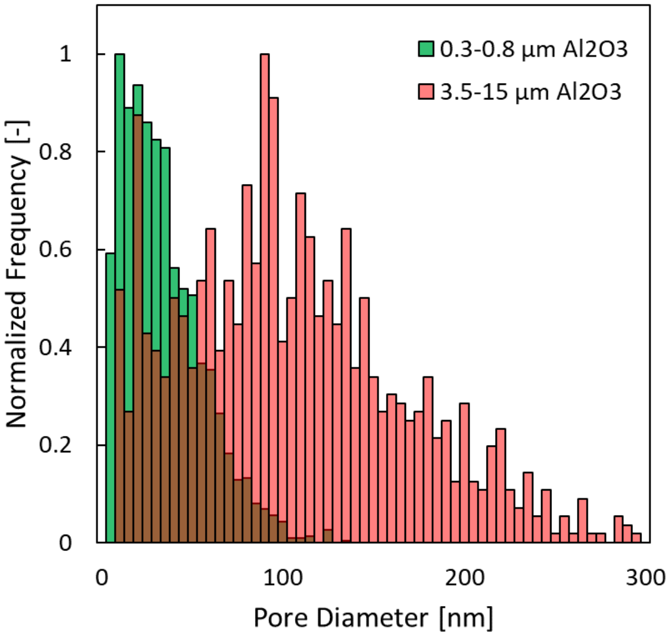

Figure 4-8 Pore size distributions of 0.3-0.8 µm Al_2O_3 packing (green) and 3.5-15 µm Al_2O_3 packing (red)

4.6. Conclusion

A simple and effective experimental technique for measuring the effective diffusivity of thin porous materials has been developed. The apparatus adopted a non-steady state approach of measuring the diffusivity with a radial geometry. Samples were initially filled with air, and oxygen was allowed to diffuse out of the sample by supplying high flow rate of N_2 gas along the perimeter of the sample. The transient oxygen concentration profile obtained from the radial diffusivity apparatus was fitted to the analytical solution of the Fick’s law of transient diffusion in cylindrical coordinates to obtain the effective diffusivity. The method was validated by measuring the binary diffusion coefficient of N_2-Air system with various gap distances and flow rates and it was shown that the gap distances and the flow rates had no effect on the measured binary bulk diffusivity.

The radial diffusivity apparatus was applied to the classical sphere packing as well as other types of porous media such as agglomerated alumina packing and quartz frits. Diffusivity in sphere packing showed good agreement with the well-known Bruggeman correlation whereas the other types of porous media exhibited lower values than predicted by the Bruggeman correlation. The method is therefore sensitive enough to detect Knudsen effects, though a full analysis of this behavior was left out for the next chapter.

Besides the fact that the current method is exceedingly simple to implement, the other crucial advantage of the radial diffusivity apparatus is that it requires no sealing, therefore can be easily applied even to ultrathin porous layers. With the recent interest in porous electrode used in energy applications such as batteries and fuel cells, the radial diffusivity apparatus can be quite powerful as most electrodes are made extremely thin to minimize the mass and charge transport limitations. Gas sensing devices are another potential application where a thin porous layer is used to detect various hazardous gases and vapors.

As with most techniques, the radial diffusivity apparatus has certain limitations. The technique is only able to measure the effective diffusivity in the in-plane direction, thus if the material possesses an anisotropic structure with different in-plane and through-plane properties, such as fibrous media, only the in-plane component of the effective diffusivity tensor can be obtained. In cases where the in-plane properties vary between the x and y directions, as in fibrous media with aligned fibers, the proposed method would be very difficult to interpret and essentially invalid.

Chapter 5 Fabrication of PGM-free Catalyst Layer with Enhanced Mass Transport Characteristics via Electrospraying Technique

5.1. Preface

In this chapter, non-PGM catalyst layers were fabricated using the electrospraying technique with various operating conditions. The structural properties of the electrosprayed non-PGM catalyst layers were extensively characterized experimentally using standard techniques as well as the method developed in Chapter 4. Non-PGM CLs with substantially different structural properties were obtained with relatively simple adjustments to the operating conditions. Tortuosity-porosity relationship was also extracted using Archie's law from the effective diffusivity data.

5.2. Abstract

The performance of Precious Group Metal-free (PGM-free) catalyst layers suffers from mass transport limitations due to the thickness required to achieve sufficiently high loading to match the performance of the Pt-based electrodes. A more detailed understanding of the PGM-free electrode structure is of a great importance to further improve their performance, but the nano-scale structure presents a challenge. In the present study, non-PGM catalyst was synthesized by the sacrificial support method and the electrospraying technique was used to fabricate catalyst layer electrodes. Electrodes with substantially different structural properties were obtained by varying the electrospraying parameters such as ink flow rate and the distance between the needle and the substrate. A wide range of structural properties of these non-PGM electrodes were

experimentally measured, including thickness, porosity, pore size distribution, specific surface area, and the mass transport characteristics in the form of tortuosity. In general, the non-PGM catalyst layers fabricated by the electrospraying technique had much lower tortuosity than conventional catalyst layers due to a combination of highly porous structure and larger inter-agglomerate pores reducing the impact of the Knudsen effect. Geometric tortuosity was also obtained by adjusting the measured effective diffusivity values to remove the Knudsen effect and it was found that electrosprayed and conventional layers follow a similar trend with porosity.

5.3. Introduction

Polymer Electrolyte Membrane Fuel Cells (PEMFCs) are an essential part of a renewable energy economy.[1] PEMFCs are particularly appealing for transportation applications because of their fast-refueling time, and long driving range per fuel charge. PEMFC powered vehicles are now produced at the commercial scale by some of the major automotive companies (i.e. Hyundai, Honda, Toyota). Despite the great progress on the development of PEMFC technology, the price is still the major barrier for wider adoption of the FC powered vehicles. The Toyota 2020 Mirai base model is priced 58,550 USD whereas the prices of other Toyota mid-sized sedans range from 24,000~28,000 USD.[4] One of the primary reasons for the high cost is the use of precious platinum (Pt) catalyst in both anode and cathode. According to a report by the Department of Energy (DOE) in 2017, Pt can make up as much as 40% of the total manufacturing cost.[156] Pt is primarily used in the cathode to make up for the sluggish kinetics of the oxygen reduction reaction (ORR).

The high cost of Pt had inspired the development of highly active nano-structured Pt-based electrocatalysts, such as Pt-alloy[8–11] and core-shell[12–19] catalysts, and more recently, shape controlled nanocrystals[20–22] and nanoframes[23–25]. Despite this progress, the Pt catalyst loading must still be further reduced for FC technology to become economically competitive with the conventional internal combustion engine.[26] An alternative path to reduce cost would be to completely replace Pt with non-precious group metal (non-PGM) catalysts. Fe-N/C catalyst is a promising class of non-PGM catalyst which was discovered by Jasinski[37] in 1964 and improved by others over the ensuing decades.[39,157] Especially, the breakthrough made by Gupta el al. [39] in 1989, where they synthesized a PGM-free ORR catalyst by heat-treating a mixture of metal salts (i.e., Co(II) or Fe(II)), polyacrylonitrile (PAN) and high surface area carbon, gave researchers much flexibility in designing the novel non-PGM catalysts.[40,27,36,41,29]

Currently, the state-of-the-art Fe-N/C catalysts give performance comparable to conventional Pt/C catalyst layers (0.2 – 0.4 $\mathrm{mg_{pt}/cm^2}$ loading) tested under air at the loading around 2 – 4 $\mathrm{mg_{FeNC}/cm^2}$ when tested under pure oxygen.[42] Proietti et al.[27] achieved a peak power density of $0.91\ \mathrm{W/cm^2}$ after careful optimization of the heat treatment conditions for iron acetate/phenanthroline/zeolitic imidazolate framework-derived catalyst. Shui et al.[31] also achieved a similar power density, i.e., around $0.9\ \mathrm{W/cm^2}$, with carbon-fiber based Fe-N/CF catalyst prepared via electrospinning with Tri-1,10-phenanthroline iron(II) perchlorate (TPI) and ZIFs, a subgroup of metal-organic-framework (MOF). Cyanamide-Polyaniline based Fe-N/C catalyst prepared by Chung et al.[28] exhibited peak power density of around $0.94\ \mathrm{W/cm^2}$. Recently, Uddin et al.[45] reported a record high peak power density with $1.14\ \mathrm{W/cm^2}$ by optimizing the primary particle size of the MOF-derived Fe-N/C catalyst. The accurate control of the primary particle size allowed the investigation of the relationship between the catalyst particle size and the quality of the ionomer infiltration which was, in turn, used to optimize the proton and reactant transport. All of the above tests, however, were done under pure oxygen and the peak power density under air is reported to be much lower, ranging from 0.2 to $0.6\ \mathrm{W/}$

cm^2.[41,29,46–50] This indicates that the non-PGM electrodes suffer severely from mass transport limitation due to the excessive thickness required to obtain a sufficient catalyst loading.

Optimizing the electrode structure to improve the transport processes is a major challenge for adoption of non-PGM catalyst layers and requires a thorough understanding of morphological features across many scales (i.e., from nano- to micro-scale). With the recent advances in imaging techniques, many of the structural and transport properties of the non-PGM catalyst layers have been resolved with various imaging techniques.[48,50,158,159] However, it is still difficult to resolve the material structure at multiple scales due to the trade-off between resolution and field of view. It is evident that experimental approaches are still the best path to characterize the morphologically dependent transport properties such as tortuosity. In the present study, non-PGM electrodes are fabricated by electrospraying under a variety of conditions to obtain different structures and morphologies to investigate the viability of electrospraying technique on producing the target structure proposed in Chapter 3. The structural and mass transport characteristics of these non-PGM electrodes were then examined experimentally by measuring thickness, porosity, pore size, specific surface area, and in-plane effective diffusivity.[65] The diffusivity was then further analyzed to extract the tortuosity, which is generally considered a structural parameter, from the measurement which was significantly impacted by Knudsen diffusion. The Bosanquet equation was used to account for the Knudsen effect and to evaluate the tortuosity from the in-plane effective diffusivity. It was shown that the electrospraying technique had the ability to create non-PGM electrodes with distinctive structural properties with relatively simple adjustments to the operating conditions, and most importantly, electrodes had high porosity and low tortuosity compared to conventionally produced layers, which is expected to be essential for the success of non-PGM catalysts.

5.4. Experimental

5.4.1. Material Production

5.4.1.1. Catalyst Synthesis and Ink Preparation

Iron-Nicarbazin (Fe-NCB) electrocatalysts were prepared by the sacrificial support method (SSM).[29,41] In short, the precursors including nicarbazin (12.5 g, Sigma-Aldrich), silica (2.5 g, LM-150, Cabot; 2.5 g, Ox-50, Evonik; 1 g, Stöber Spheres, home-made) and iron nitrate (1.2g, Sigma-Aldrich) were mixed in water. The water in the suspension was slowly allowed to evaporate until a gel was formed. The gel was then completely dried and the remaining solid was ground initially by a mortar and a pestle and subsequently by a ball mill, for 30 min, at 45 Hz. The solid mix of precursors was subjected to a first pyrolysis at 975 °C, under a 7% H_2 after atmosphere. Then, the silica particles were etched out with 40% HF for 4 days. The etched precursors were washed until the effluent had a neutral pH, then were subjected to a second pyrolysis at 950 °C for 30 min. After the second pyrolysis, the resulting electrocatalysts were ball-milled for 1 hr. More detailed synthesis parameters can be found elsewhere.[29,41]

The catalysts were made into inks by first mixing Fe-NCB electrocatalysts and 5 wt% Nafion™ dispersion in isopropyl alcohol (IPA). 5 wt% Nafion™ dispersion was prepared by diluting 1000 EW 20 wt% Nafion™ dispersion (D2020, Fuel Cell Store, US) in IPA. The dry weight of Nafion™ was adjusted to be 45% of the total solid deposit and the catalyst to solvent ratio was 5 $\mathrm{mg_{catalyst}/mL_{solvent}}$. The suspension was then subjected to sonication in an ice bath for 2 hours.

5.4.1.2. Preparation of the Catalyst Layers

Different non-PGM electrodes were fabricated by the electrospraying technique which has the ability to create a variety of microstructures with relatively simple adjustments to the process.[91,92,97,96,93–95,98–100] The electrospraying technique has been used to fabricate conventional Pt/C catalyst layers over the last decade, however, it has never been applied to non-PGM catalyst. There are some reports suggesting the electrosprayed catalyst layers show better mass transport characteristics[99,100] which makes it an appealing deposition technique for non-PGM electrodes. In the present work, operating parameters such as flow rate and the distance between the needle and the substrate, were varied in an attempt to correlate the electrode characteristics to their transport properties.

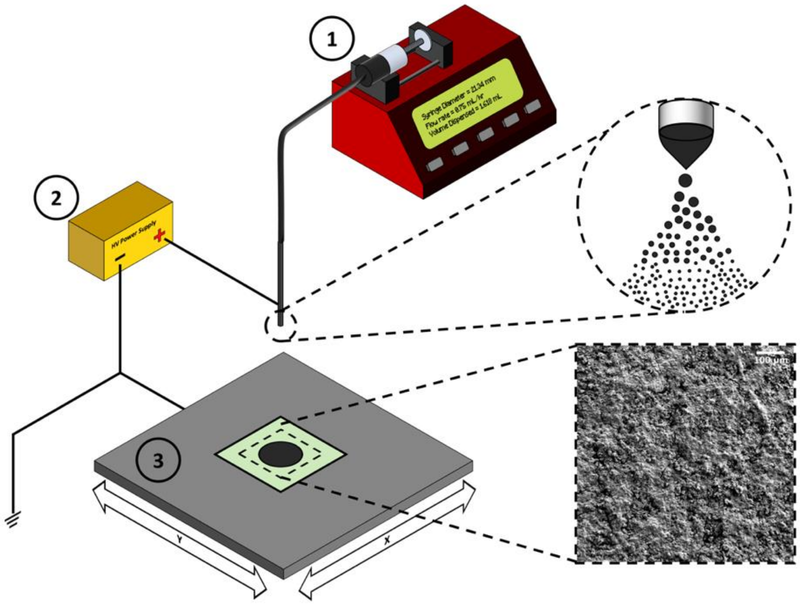

Figure 5-1 Schematic diagram of electrospraying setup. The setup includes 1) a syringe pump, 2) high voltage power supply and 3) XY moving stage

The electrospraying setup was built in-house with a syringe pump (NE1000, New Era Pump Systems Inc.), a syringe stirrer (VP710D3, V&P Scientific Inc.) and a high-voltage power supply (MJ30P0400-11, Glassman) as shown in Figure 5-1. The conventional polarity configuration was used where the positive pole was connected to the capillary needle and the conductive substrate was grounded. The high voltage power supply was remotely controlled via multifunctional I/O device (USB-6001, National Instruments). To ensure a homogeneous deposition, a custom-built XY moving stage was used. A conductive aluminum plate was installed on the moving stage. In order to collect a smooth catalyst layer, it was deposited on a $175\ \mu$m thick Indium-Tin-Oxide coated Polyethylene Terephthalate (ITO/PET) layer. Due to PET's sturdiness and smooth surface, it provided several advantages in handling and characterizing the samples compared to the typically used aluminum foil. The entire electrospray system was automated via LabVIEW to control the rastering speed and path, pump flow rate, and power supply voltage. The catalyst ink was deposited onto the substrate in a serpentine pattern, alternating between the horizontal and the vertical direction for a homogeneous coating, at a speed of $15\ \mathrm{mm/s}$ with 0.5 mm pitch. The ink flow rate (Q) and the needle-to-substrate distance (d) were varied for the present study and the applied voltage was adjusted until the droplet at the needle tip formed a Taylor cone for the stable cone-jet mode. The initial study plan was to include the impact of the applied voltage on the microstructure of the catalyst layer, however, only a relatively narrow range of voltages allowed a for stable cone-jet operation, so this parameter was not flexible. For the present study, the applied voltage ranged from $3.50{\sim}4.50$ kV, which was determined on a case by case basis to establish a stable cone.

The catalyst loading was checked by measuring the initial and the final weight of the sample assuming that the ink stayed homogeneous throughout the deposition. This was a fair assumption since the ink was ultrasonicated for 2 hours prior to the deposition and was also stirred throughout the whole deposition process. The studied electrospraying parameters and the weight-based catalyst loadings are summarized in Table 5-1.

Table 5-1 A summary of electrospray operating parameters and the catalyst loadings

Sample Name	Flow Rate [mL/hr]	Distance [cm]	Voltage [kV]	Catalyst loading [$\mathrm{mg/cm^2}$]
Q50D30	0.50	3.0	3.50	2.91
Q75D30	0.75	3.0	3.50	2.92
Q100D30	1.00	3.0	3.90	2.93
Q50D50	0.50	5.0	3.70	2.97
Q75D50	0.75	5.0	3.70	3.13
Q100D50	1.00	5.0	4.00	3.12
Q50D70	0.50	7.0	4.20	3.04
Q75D70	0.75	7.0	4.40	2.92
Q100D70	1.00	7.0	4.50	2.98

5.4.2. Electrode Characterization

5.4.2.1. Porosity and Thickness

The porosity of each electrode sample was measured using the buoyancy method.[116,160] The method essentially uses the Archimedes' principle to obtain the skeletal density of the sample from the missing mass between the dry and the submerged weight in a highly wetting fluid. The samples were dried at $105°\mathrm{C}$ for at least 12 hours prior to the measurement to remove any water residing in the pore space. The samples were then further dried under vacuum at room temperature before being saturated with the wetting fluid. For the current study, $5\ \mathrm{cSt}$ silicone oil (Clearco Products Co., Inc., US) was used as the wetting fluid.

To obtain the bulk volume of the catalyst layer samples, the thicknesses of the samples were measured using a micrometer with $1\ \mu\mathrm{m}$ resolution with $\pm 0.1\ \mu\mathrm{m}$ readout resolution. The micrometer was equipped with friction clutch to ensure the sample was always compressed to the same amount of force. The thickness of the substrate was measured before the deposition. The substrate was quite smooth and consistent with the average thickness of $175\ \mu\mathrm{m}$ and the deviation of $\pm 1\ \mu\mathrm{m}$. The sample thickness was calculated by subtracting the thickness of the substrate from the total thickness.

Since the catalyst layer samples were in two layers (catalyst layer + substrate), Eq. [5-1] was used to calculated the actual porosity of the catalyst layers assuming that the substrate was essentially non-porous:

$$\varepsilon_{sample} = \varepsilon_{overall} \cdot \frac{\delta_{overall}}{\delta_{sample}} \qquad [5\text{-}1]$$

where ε_{sample} is the actual porosity of the electrode layer, $\varepsilon_{overall}$ is the overall porosity of the electrode and the substrate measured by the buoyancy method, $\delta_{overall}$ is the thickness of the electrode and the substrate combined and δ_{sample} is the thickness of the electrode sample only.

The porosity measured by the buoyancy method was cross-checked by calculating the theoretical porosity based on the ink composition. The composition-based porosity was estimated using the following relations:

$$\varepsilon_s = \frac{m_{cat}}{\delta} \cdot \frac{1}{\rho_{cat}} \qquad [5\text{-}2]$$

$$\varepsilon_n = \frac{m_{cat}}{\delta} \cdot \frac{\omega_n}{(1-\omega_n)\rho_n} \qquad [5\text{-}3]$$

$$\varepsilon_v = 1 - \varepsilon_s - \varepsilon_n \qquad [5\text{-}4]$$

where ε is the volume fraction of each phase, ρ is the density, m_{cat} is the catalyst loading, δ is the thickness of the catalyst layer and ω_n is the Nafion™ loading in mass fraction. The subscripts s, n and v denote solid (catalyst), Nafion and void, respectively. The density of the non-PGM catalyst was measured by gas pycnometer (Ultrapyc 5000 Micro, Quantachrome, US) using helium as the working gas. The measured density of the non-PGM catalyst was $2.326\ \mathrm{g/cm^2}$ and $2.0\ \mathrm{g/cm^2}$ was used as the density of the Nafion™.[73]

5.4.2.2. Pore Size Distribution

The pore size distributions of the samples were estimated by mercury intrusion porosimetry (PoreMaster® 33, Quantachrome, US). First, the cumulative intrusion curve as a function of capillary pressure was obtained and smoothed by weighting each point by its neighboring points (4% of the data). Next, the obtained capillary pressure was then converted into an approximate pore size using the Washburn equation:

$$d_{pore} = -\frac{4\gamma \cos\theta}{p_c} \qquad [5\text{-}5]$$

where d_{pore} is the pore diameter estimated by the Washburn equation, γ is the surface tension of mercury (Hg), θ is the contact angle of Hg and p_c is the capillary pressure. $0.485\ \mathrm{N/m}$ was used for the surface tension and $140°$ was used for the contact angle.

Finally, the cumulative intrusion curve was normalized by the total intruded volume and its derivative was used to obtain the pore size distribution, i.e.,

$$\frac{dX_i}{d\ln(r_i)} = \frac{1}{V_T}\frac{V(r_i) - V(r_{i-1})}{\ln(r_i) - \ln(r_{i-1})} \qquad [5\text{-}6]$$

where X_i is the normalized volume of pore radius r_i at i^{th} intrusion step and $V(r_i)$ is the cumulative intrusion at r_i.

When performing the mercury intrusion for thin nanoporous electrodes, such as fuel cell catalyst layers, often mercury intrusion is observed during the filling process in the low pressure station.[160,161] This is attributed to the presence of a void space either between the samples themselves or between the sample and the wall of the penetrometer. To avoid this problem, the non-PGM electrodes were made into three strips of 70 mm x 9 mm and were loaded into the penetrometer in a triangle shape, the substrate side facing the wall of the penetrometer.

5.4.2.3. Specific Surface Area

For the specific surface area, N_2 sorption experiments were performed at 77 K using a Gemini VII surface analyzer (Micromeritics, US). All samples were cut into a known shape which weighed ~ 200 mg. They were then cut into smaller pieces to fit into the glass tube. The samples were pre-conditioned by purging dry N_2 gas for at least 12 hours at 105℃. The specific surface areas were calculated from the standard Brunauer-Emmett-Teller (BET) equation in the range of $0.05 \sim 0.30\ p/p_0$. The specific surface areas are typically reported in the unit of m^2/g. Although, this is useful for materials such as catalysts themselves, it is not very informative for electrode samples. The more relevant metric for the catalyst layer samples would be the surface area per unit volume or per unit area of the catalyst layer. Therefore, the specific surface areas were converted into m^2/m^3 and m^2/m^2 in this work, using the known geometric properties of the samples.

5.4.2.4. In-Plane Effective Diffusivity

The radial in-plane effective diffusivity, D^{eff}, of the electrosprayed non-PGM catalyst layers were measured using the technique developed and validated previously.[65] This technique was designed to be applied to thin layers, and has been proven to provide accurate results quickly and simply. Briefly, a porous electrode sample is cut in a thin disk and sandwiched between two cylindrical pedestals. The sample is initially flushed with N_2 to create $c_{O_2} = 0$ inside the microstructure of the porous sample. Once the sample is completely filled with N_2 gas, the boundary conditions are changed by flowing air past the outer radius so O_2 is allowed diffuse into the microstructure of the porous sample. The O_2 concentration is measured using a high-speed fiber optic oxygen probe (OXR430-UHS, PyroScience GmbH, Germany) at the center of the sample. The benefit of this technique is that it does not require any gasket[119,162,163] which makes it particularly suited for thin porous materials such as catalyst layers. The resulting data is in the form of oxygen concentration vs time. The effective diffusivity of the sample can be obtained by fitting the experimental oxygen vs time data to Fick's second law with the effective diffusivity as a fitting parameter. For the present paper however, this was taken one step further to separate the structural tortuosity and the Knudsen effect, as discussed later.

5.5. Results and Analysis

5.5.1. Morphology, Thickness and Porosity

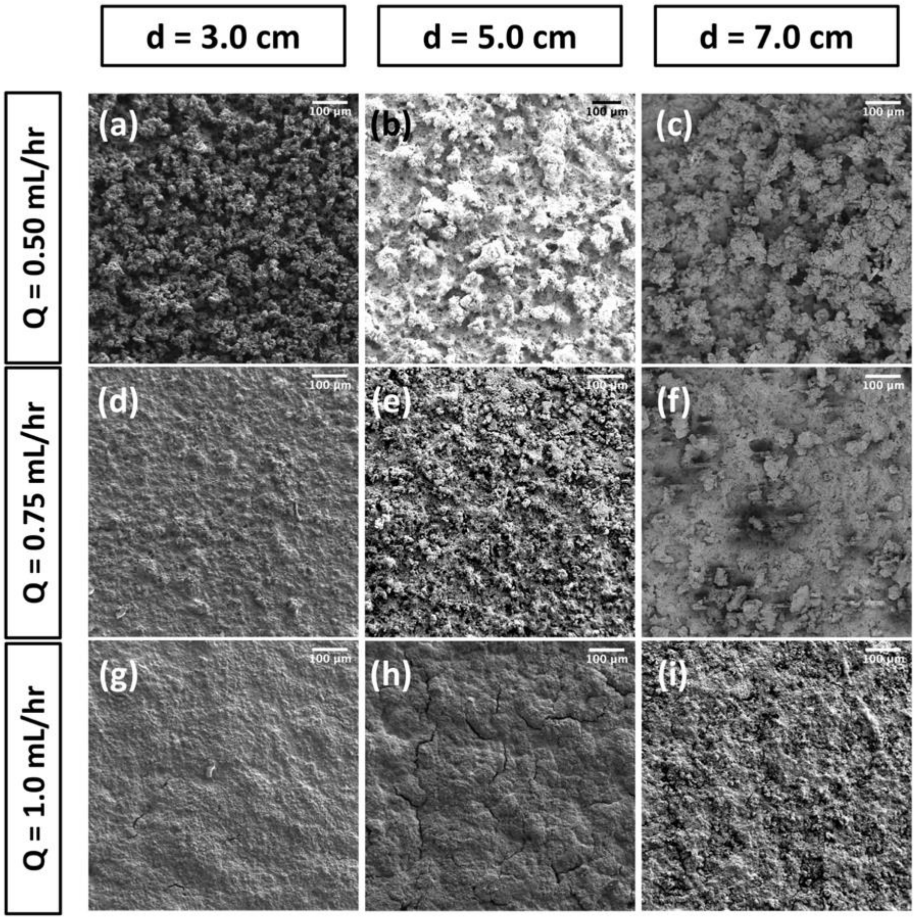

Figure 5-2 SEM images of electrosprayed non-PGM catalyst layers (a) Q50D30 (b) Q50D50 (c) Q50D70 (d) Q75D30 (e) Q75D50 (f) Q75D70 (g) Q100D30 (h) Q100D50 (i) Q100D70

The SEM images of the electrosprayed PGM-free catalyst layers are shown in Figure 5-2. In general, the morphology of the electrosprayed layers looked less dense when produced with the slower flow rate and became more compact as the flow rate was increased. No difference was visually observed between samples with different distances.

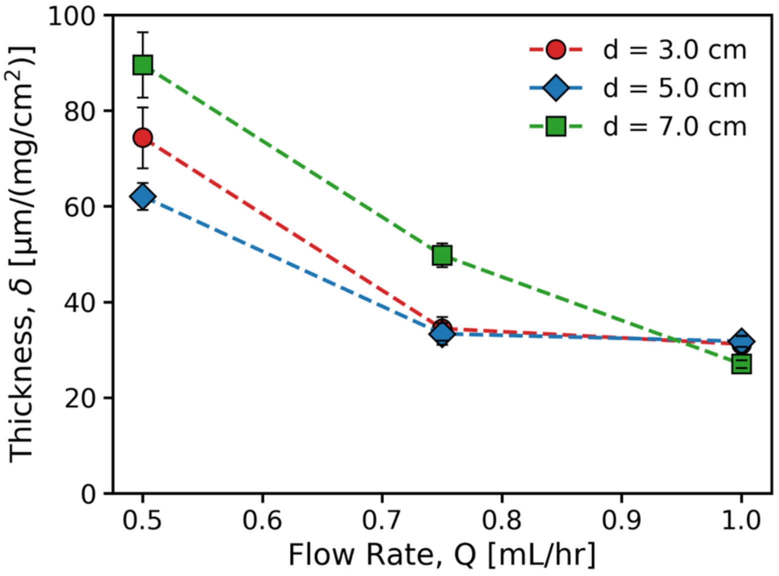

Figure 5-3 Thicknesses of non-PGM catalyst layers electrosprayed at various operating conditions. d is the needle-collector distance and Q is the flow rate of the catalyst ink (NOTE: The total thickness was normalized by the catalyst loading to eliminate the loading effect from the analysis)

Since the thickness of the catalyst layer is a function of the catalyst loading, the total thickness was normalized by the actual catalyst loading in Table 5-1. Figure 5-3 shows the normalized thicknesses of the electrosprayed non-PGM catalyst layers under various flow rates and distances. The thickness of the electrosprayed PGM-free catalyst layers with $3.0\ \mathrm{mg/cm^2}$ target loading ranged from 80 to $270\ \mu\mathrm{m}$ depending on the operating parameter. As an indication that the electrospraying technique is indeed creating more porous layers, their thickness is generally higher than non-PGM layers made by conventional means. This was also observed by Takahashi et al.[99] where the Pt-based catalyst layer always resulted in a thicker layer with electrospraying technique compared to the pulse spray coating. Workman et al.[29,41] prepared the non-PGM catalyst layers with the same type of non-PGM catalyst using an ultrasonic nozzle and reported a thickness of around $75\,\mu\text{m}$ with $3\,\text{mg/cm}^2$ loading. Baricci et al.[164], also fabricated catalyst layers with the same type of catalyst, but with a spray gun and they reported much thicker layers with the thickness of $261\,\mu\text{m}$ with the catalyst loading of $4\,\text{mg/cm}^2$. Assuming the thickness increases linearly with the catalyst loading, this would correspond to approximately $200\,\mu\text{m}$-layer with $3\,\text{mg/cm}^2$ loading. Clearly the thickness of the catalyst layer is a strong function of the deposition method. In the study of Workman et al.[29,41], they used a high flow rate (i.e. $1\,\text{mL/min}$) suggesting that the deposited layer was not necessarily dry and the solvent needed to evaporate afterwards.

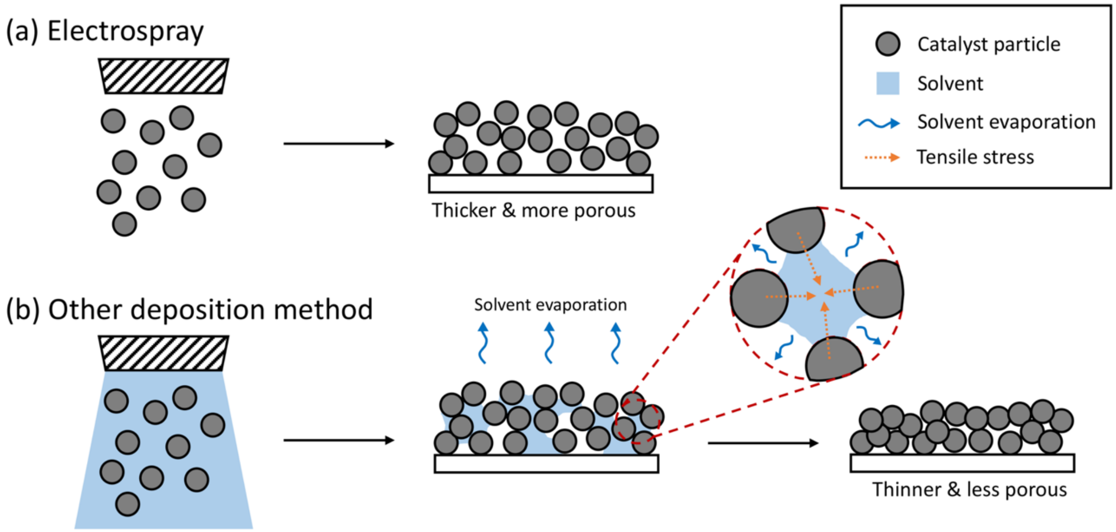

Figure 5-4 Comparison of electrospraying technique and other deposition methods

During solvent evaporation, the tensile stress caused by the capillary force may have pulled the catalyst particles closer together, creating more compact and thinner structure. In the electrospray deposition, however, the solvent is expected to dry in flight and only relatively dry solid would collide into the substrate causing a thicker and less compact layer. This is illustrated in Figure 5-4. The trend is clear from Figure 5-3, where the thickness generally decreases with increasing flow rate. This hypothesis is also supported by the SEM images in Figure 5-2. However, the trend was not as clear with the needle-collector distance (d). By the same logic, it would be expected that as the distance gets larger, the thickness would increase because the solvent would have more time to evaporate. Although, this trend was more or less followed when the flow rates were 0.75 and 1.0 mL/hr, when the flow rate was 0.50 mL/hr, the thickness of the catalyst layer was thicker when the distance was 3.0 cm compared to when the distance was 5.0 cm. This may indicate that 3.0 cm was enough for the droplet to completely dry with the slowest flow rate (0.5 mL/hr).

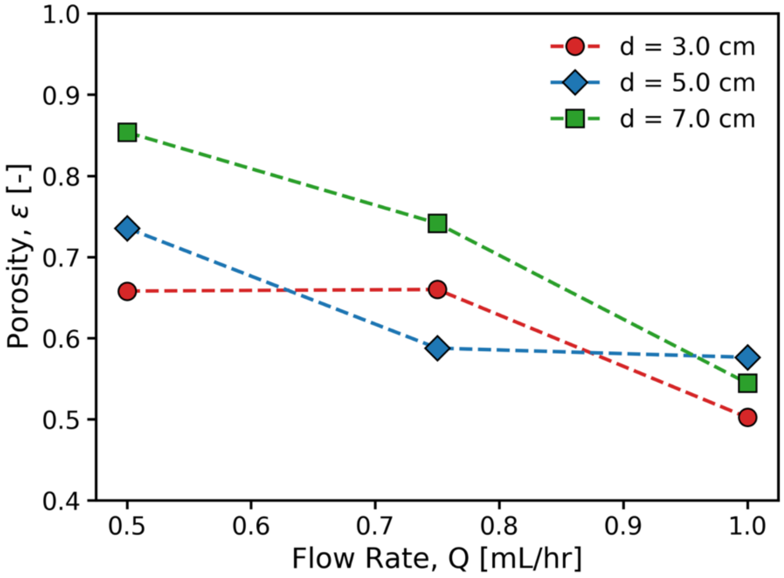

Figure 5-5 Porosities of non-PGM catalyst layer electrosprayed at various operating conditions

Figure 5-5 shows the porosity of the electrosprayed PGM-free catalyst layers. There is only limited information available on the porosity of the PGM-free catalyst layers in the literature, however the packing of nanoparticles with impregnated Nafion™ typically results in 40 to 70%

porosity.[160,161,165] In Figure 5-5, the porosity of the electrosprayed catalyst layer was as high as 85% showing its ability to create highly porous structure which is expected to be beneficial for reactant transport. By the same reasoning as the analysis of the thickness above, the porosity generally increased with the decreasing flow rate. Figure 5-6 shows the comparison between the porosity obtained by the buoyancy method and the porosity calculated based on the ink composition. Although, the density of $2.0\ \mathrm{g/cm^3}$ is typically used for Nafion™, the density of Nafion™ can change from 1.40 to $2.0\ \mathrm{g/cm^3}$ depending on the water content in Nafion™.[166] Also, it is possible that thin film of Nafion™ has different density than the bulk Nafion™. To account for this, the porosity based on a range of possible Nafion™ density is indicated as error bar in Figure 5-6. $1.5\ \mathrm{g/cm^3}$ was used for the lower error bar and $2.5\ \mathrm{g/cm^3}$ was used for the upper error bar. The two values were generally in good agreement.

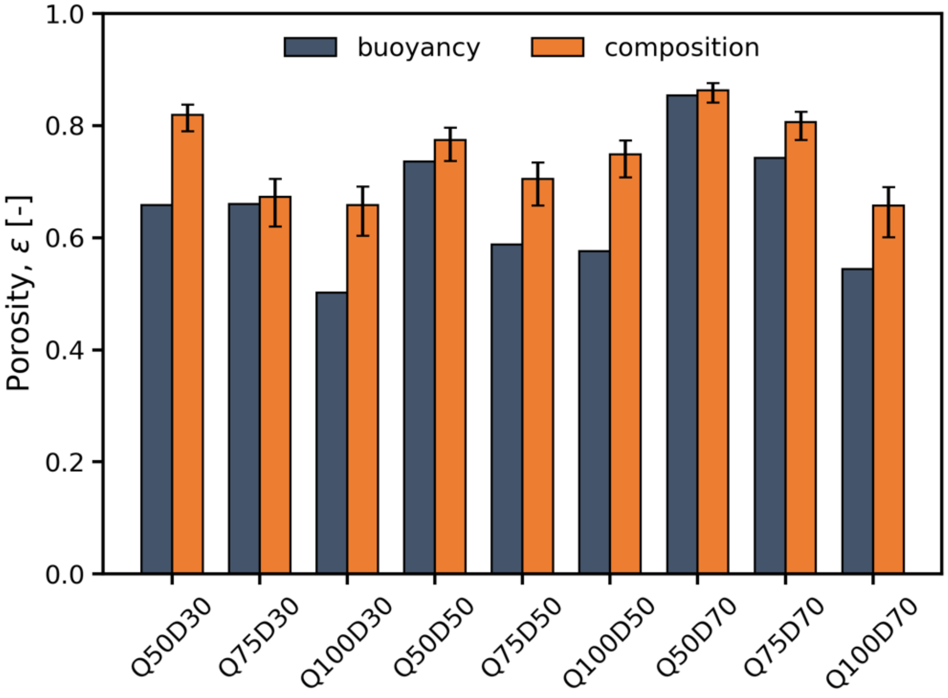

Figure 5-6 Comparison of porosity obtained by two different methods (Buoyancy and composition-based). $\rho_{Naf} = 2.0\ \mathrm{g/cm^3}$ used for the orange bars. 1.5 and $2.5\ \mathrm{g/cm^3}$ are used for lower and upper error bars, respectively.

In summary, the electrospraying process resulted in layers that, for the same catalyst loading, were up to 3 times thicker compared to other deposition techniques, such as air spraying and ultrasonic spraying. A low porosity catalyst layer is undesirable in PGM-free catalyst layers since it would worsen the already high mass transport resistance. The electrospraying technique can enhance mass transport by creating a more porous structure.

5.5.2. Pore Size Distribution

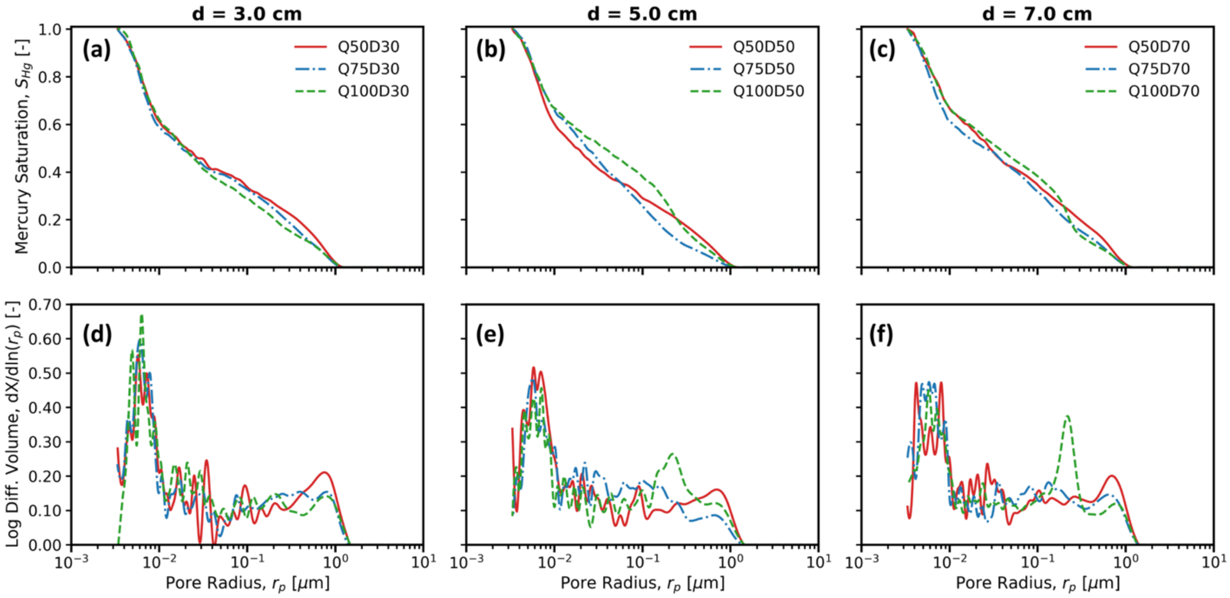

Figure 5-7 Capillary pressure curves (a – c) and pore size distributions (d – f) of non-PGM catalyst layers electrosprayed under various operating conditions; (a), (d) d = 3.0 cm and Q = 0.50, 0.75, 1.0 mL/hr; (b), (e) d = 5.0 cm and Q = 0.50, 0.75, 1.0 mL/hr; (c), (f) d = 7.0 cm and Q = 0.50, 0.75, 1.0 mL/hr

Figure 5-7 shows the capillary pressure curves (a – c) obtained from the mercury intrusion porosimetry (MIP) and the pore size distribution (d – f) calculated using the Washburn equation. All catalyst layer samples show a bimodal distribution with a sharp peak at $5 - 10$ nm, and a wide peak spanning a range of 10 nm to $1\ \mu$m. The first peak, around 7 nm radius, is presumably due to the pores within the catalyst particles, while the second, wide pore region is due to the pores between the catalyst agglomerates in the catalyst layer.

From the synthesis steps, the catalyst prepared by the sacrificial support method is expected to have a bimodal pore size distribution with one peak at $5 - 10$ nm and the other one around at 70 nm, the latter being a result of the etched out Stöber spheres. This was confirmed by conducting the gas sorption experiment of the non-PGM catalyst and calculating the pore size distribution of it using the BJH method, as shown in the left most figure in Figure 5-8. The pore size distribution obtained from MIP experiments does not show a clear peak at 70 nm. The suppression of the 70 nm peak can be attributed to the fact that the Nafion™ can intrude into the pores greater than 30 nm.[167] Since the MIP experiments were done on the catalyst layer samples, the pores formed from the etched out Stöber spheres are likely intruded by the Nafion™. Nafion™ cannot enter into ~ 7 nm pores, therefore the smaller pores can still be clearly observed in the MIP results. The proposed electrode structure is shown in the right figure in Figure 5-8.

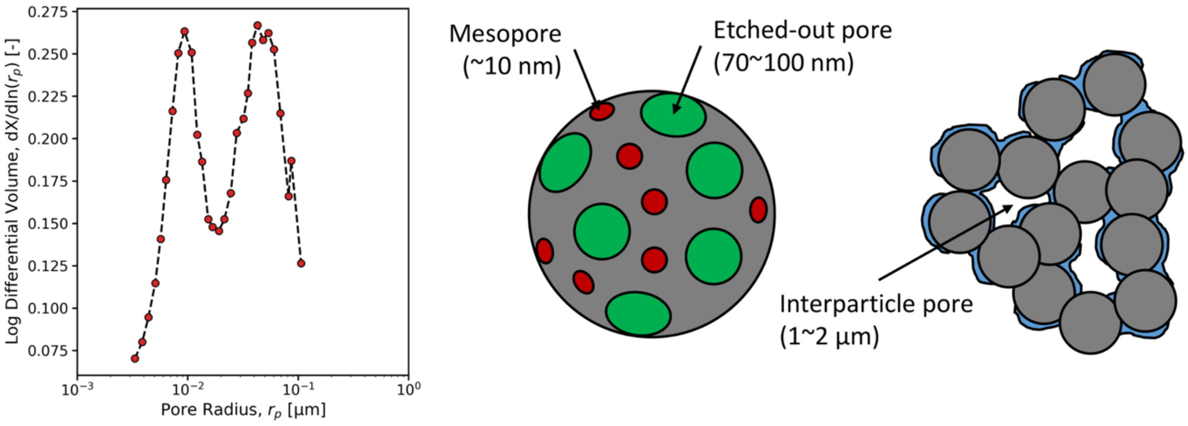

Figure 5-8 Left: Pore size distribution of catalyst particles obtained with BJH theory. Right: Proposed structure of the electrosprayed PGM-free catalyst layer based on MIP and BJH pore size distributions.

From Figure 5-7, it is evident that there is no major difference in the 10 nm peak. This is expected since the electrodes have the same catalyst and Nafion™ loading. The slowest flow rate, 0.50 mL/hr generally showed the highest macropore volume (i.e., at 1 μm). This coincides with the fact that the porosity increased as the flow rate was decreased because macropores contribute more to the porosity than the micro- or mesopores. Samples prepared at flow rate 1.0 mL/hr with distance 5.0 cm and 7.0 cm showed an extra peak at ~200 nm. The extra peak could have been induced by poor Nafion™ coverage due to high flow rate, but further study is required to draw any firm conclusion.

5.5.3. Specific Surface Area

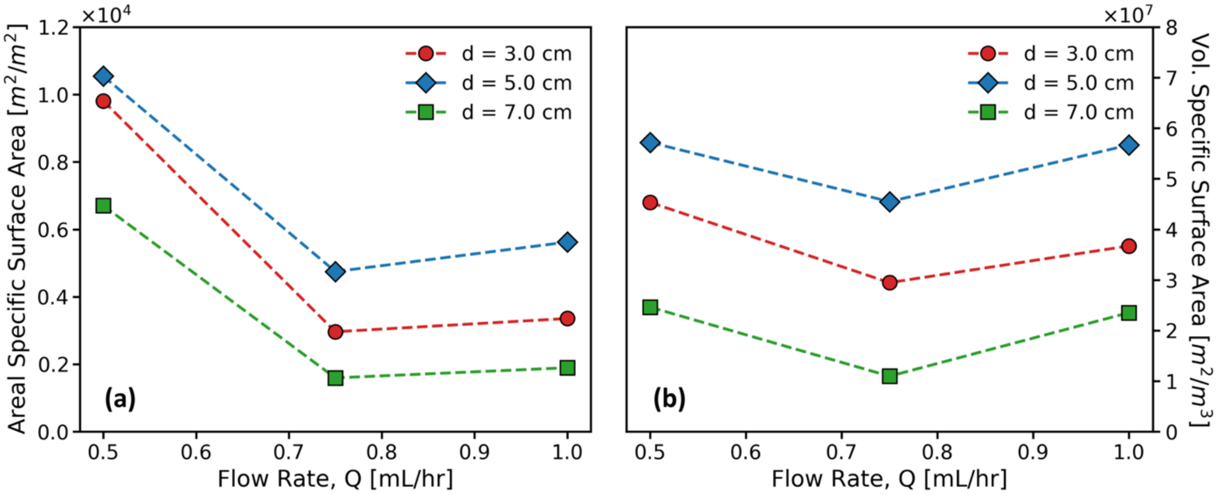

Figure 5-9 Specific surface area of electrosprayed PGM-free catalyst layers (a) per active area and (b) per active volume

The specific surface area (SSA) of the catalyst itself and the catalyst layer samples were measured by the gas sorption experiment. The SSA of the Fe-NCB catalyst was around $650\ \mathrm{m^2/g}$ which is similar to the reported value of the same type of catalyst.[48] Figure 5-9 shows the areal (a) and the volumetric (b) SSA of each catalyst layers samples. The areal SSA of the electrosprayed PGM-free catalyst layers were in the order of $10^4\ \mathrm{m^2_{BET}/m^2_{electrode}}$. It is clear from Figure 5-9 that the samples made with the slowest flow rate had the highest areal SSA. For the flow rates 0.75 and 1.0 mL/hr, the areal specific surface area stayed more or less the same for all distances. The areal SSA generally increased from 3.0 cm to 5.0 cm, however, the samples sprayed at 7.0 cm distance showed the lowest SSA. There seems to be a critical distance where the SSA can be increased, however, more study is required.

Interestingly, when the thickness was considered (i.e. volumetric SSA), the SSA flattened out and no clear variation was visible between different flow rates. This can be an important consideration when optimizing the electrosprayed electrode since this means that the SSA is essentially independent of the flow rate assuming the distance is fixed. Therefore, when optimizing the electrospraying parameters, one can expect that the samples electrosprayed at the same distance would have similar activation loss and the mass transport losses in the electrode (i.e., H^+, e^-, reactants and product) are more important considerations.

5.5.4. Effective Diffusivity

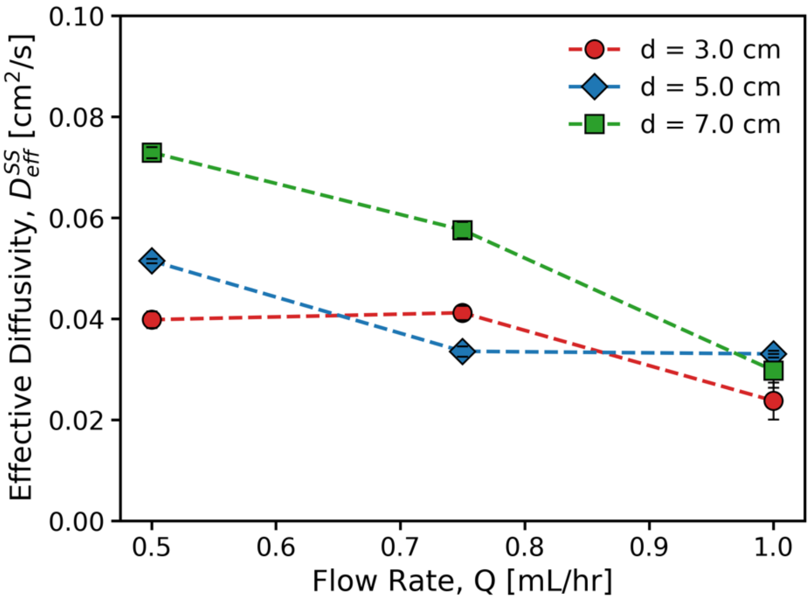

Figure 5-10 Effective diffusivities of the electrosprayed PGM-free catalyst layers at various operating conditions

Figure 5-10 shows D^{eff} for the electrosprayed samples fabricated under various conditions, with values ranging from $0.02\ \mathrm{cm}^2/\mathrm{s}$ to $0.08\ \mathrm{cm}^2/s$. The effective diffusivity values closely followed the porosity trend, with samples produced at slower flow rates showing higher effective diffusivity. This is expected since the effective diffusivity is known to be strongly dependent on the porosity of the material. The measured effective diffusivity values are about an order of magnitude higher than the reported values for the conventional Pt-based catalyst layers.[161,165,87,168,57] This can be attributed to the fact that the electrosprayed PGM-free electrode had much larger secondary pores (inter-agglomerate pores) than the conventional Pt-based electrodes. The reported peak value of the secondary pore radius of the Pt-based electrode is somewhere between $20-50\ \mathrm{nm}$ depending on the type of carbon support used and the deposition method[161,57,169,55] whereas it is as high as $1\ \mu\mathrm{m}$ for the electrosprayed PGM-free catalyst layers according to the MIP results. To illustrate this further the pore size distributions obtained for three different types of catalyst layers using MIP are compared in Figure 5-11. The Pt/C catalyst layers prepared by the inkjet printing technique[5,80], regardless of the type of the carbon support used, show maximum pore radii below $100\ \mathrm{nm}$. In contrast, the secondary pores in the electrosprayed PGM-free catalyst layer are much larger so consequently the electrosprayed PGM-free electrode will have less Knudsen resistance. In addition, the higher diffusivity observed in the present electrosprayed samples can be partly attributed to the fact that they had higher porosity that those reported for conventional CLs.

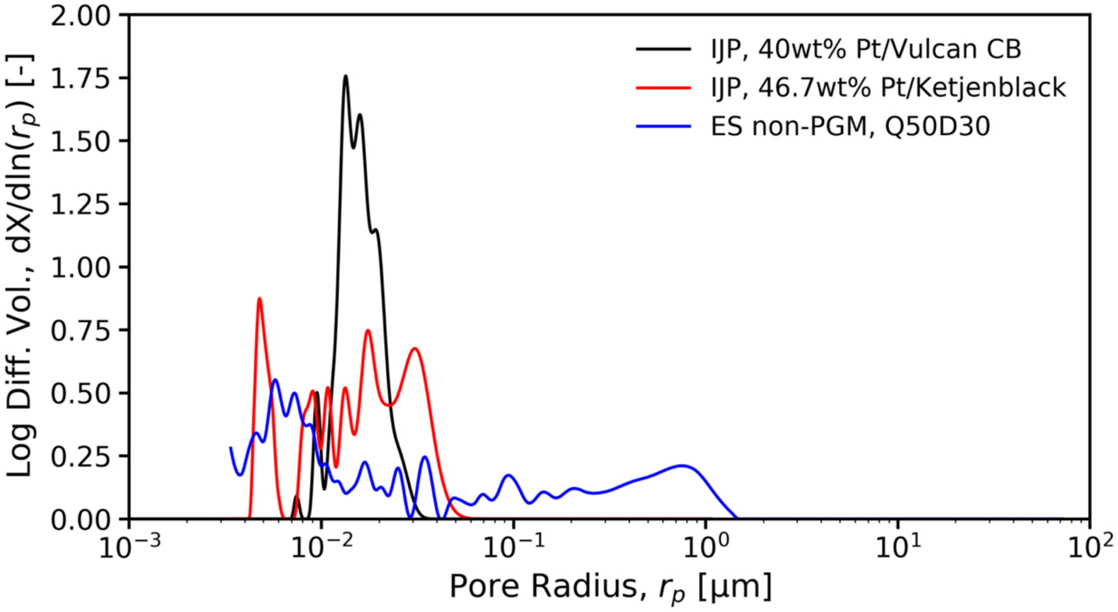

Figure 5-11 Comparison of conventional inkjet printed Pt/C catalyst layer and the electrosprayed PGM-free catalyst layer – Black: Inkjet printed Pt/C (Vulcan) catalyst layer, Red: Inkjet printed Pt/C (Ketjenblack) catalyst layer and Blue: Electrosprayed PGM-free catalyst layer.

5.5.5. Tortuosity

In Chapter 4, the analysis of Knudsen effect of the nanoporous alumina packing was left out to focus on the viability of the technique developed on measuring the effective diffusivity of thin porous media. To fill the knowledge gap, the effect of Knudsen friction on the effective diffusivity and tortuosity is further analyzed in this section. The effective diffusivity is an important transport property, but it depends on the surrounding conditions as well as the pore sizes of the material. The tortuosity, however, depends only on the morphology of the porous media. Once the tortuosity is obtained for a particular material, it can be used to calculate the effective diffusivity of the material under any conditions, including the Knudsen regime.

In Table 5-2 the average pore diameter and the corresponding Knudsen numbers ($\mathrm{Kn} = \lambda/d_{pore}$) for all samples tested here are listed (λ is the mean free path defined as $k_B T/\sqrt{2} p \pi d_g^2$

where k_B is the Boltzmann constant, T is the temperature, p is the pressure and d_g is the effective diameter of the gas molecule). Since the Knudsen numbers fall between 0.1 and 10 the Knudsen resistance is present in all the experimental data. Therefore, in order to obtain the true geometric tortuosity owing purely to the structure of the produced materials, this resistance must be removed from the measured effective diffusion values.

Table 5-2 Average pore diameter, Knudsen number, molecular diffusivity and Knudsen diffusivity of electrosprayed non-PGM catalyst layers

Sample Name	$d_{p,avg}$ [nm]	Kn [−]	D_{ij} [cm^2/s]	D_{ik} [cm^2/s]
Q50D30	357	0.2132	0.2039	0.5277
Q75D30	306	0.2488	0.2039	0.4523
Q100D30	279	0.2729	0.2039	0.4124
Q50D50	289	0.2634	0.2039	0.4271
Q75D50	202	0.3769	0.2039	0.2986
Q100D50	294	0.2589	0.2039	0.4345
Q50D70	330	0.2307	0.2039	0.4877
Q75D70	274	0.2778	0.2039	0.4050
Q100D70	287	0.2653	0.2039	0.4242

There are only a limited number of studies that have attempted to remove the Knudsen resistance from experimentally obtained values to produce a geometric tortuosity. Pant et al.[170] developed a diffusion bridge technique that could simultaneously measure the permeability and the Knudsen diffusivity of microporous layers which have similar structure and pore sizes to CLs.[171,172] They used the binary friction model to account for the Knudsen effect. Yu et al.[161] and Inoue et al.[87] used a simpler approach based on the Bosanquet equation. This latter approach was used in the present work to determine the geometric tortuosity for the electrosprayed catalyst layers.

The standard definition of tortuosity is given as:

$$\tau_{obs} = \varepsilon \cdot \left(\frac{D_{i,j}}{D_i^{eff}}\right) \qquad [5\text{-}7]$$

where D_i^{eff} is the experimentally observed effective diffusivity as discussed in the previous section, and $D_{i,j}$ is the binary diffusivity of the diffusing species in open air. This definition of τ is denoted as *observed* since it is based on the uncorrected observed D_i^{eff} values.

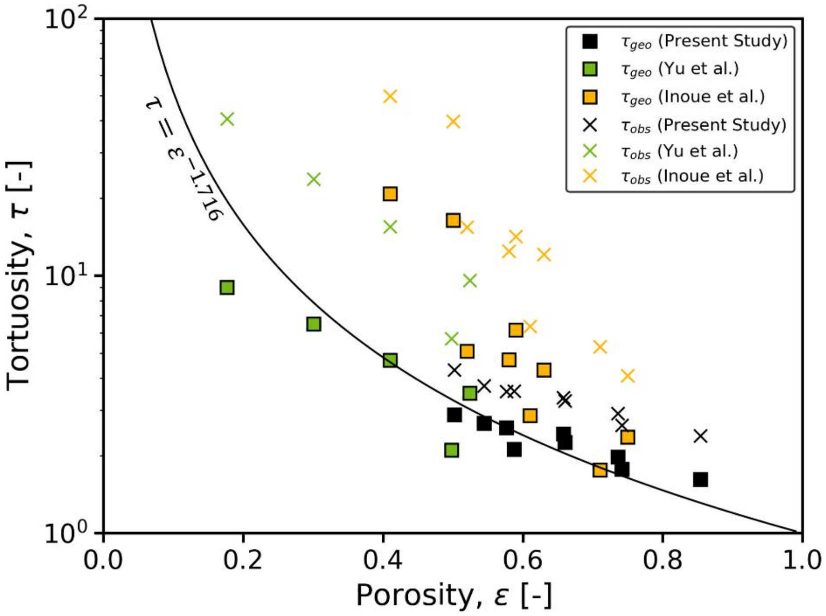

Figure 5-12 Tortuosity-Porosity plot of the electrosprayed PGM-free catalyst layers. (Lines indicate the power-law fit whereas the markers are the experimental data). *Note: The observed tortuosity from the work of Yu et al.[161] was calculated based on the information given. Others are plotted as given in the work.

Figure 5-12 shows the τ_{obs} values computed using Eq. [5-7] as a function of porosity. This figure also shows the published results of Yu et al.[161] and Inoue et al.[87] for their conventional catalyst layers, and the observed tortuosity is notably higher than the electrosprayed materials. Not only do the conventional materials have generally lower porosity, but their trend with porosity is offset substantially upwards compared to the electrosprayed materials, due to the higher Knudsen resistance present in their much smaller pores.

The true geometric tortuosity (τ_{geo}) of these materials was found by adjusting for the impact of the Knudsen resistance as follows:

$$\tau_{geo} = \varepsilon \cdot \left(\frac{D_i}{D_i^{eff}}\right) \tag{5-8}$$

where D_i is the prevailing gas diffusion coefficient in the experiment owing the combination of molecular diffusion and Knudsen effects, and was estimated using the Bosanquet equation:

$$D_i = \left(\frac{1}{D_{i,j}} + \frac{1}{D_{i,k}}\right)^{-1} \tag{5-9}$$

where $D_{i,j}$ is the binary molecular diffusivity between species i and j and $D_{i,k}$ is the Knudsen diffusivity of the species i. The Knudsen diffusivity was evaluated as:

$$D_{i,k} = \frac{d_{pore}}{3}\sqrt{\frac{8RT}{\pi M_i}} \tag{5-10}$$

where R is the gas constant, and d_{pore} is the average pore diameter calculated from the capillary pressure curve data as the volume-averaged pore diameter[57]:

$$d_{pore} = \frac{1}{V_T}\sum_i V_i d_i \tag{5-11}$$

where V_T is the total pore volume, V_i is the pore volume at the i^{th} intrusion step and d_i is the corresponding pore diameter. Figure 5-10(b) shows the τ_{geo} for both the electrosprayed and conventional CLs calculated using Eq. [5-8]. Unlike the τ_{obs} values, in this case it can be seen that both materials follow a common trend, which suggests that they have similar pore structures. This is to be expected given the similarities in the constituent materials (carbon power and Nafion™ ionomer). The τ_{geo} values follow the expected power-law function with porosity; therefore, an attempt was made to fit the power law function to the experimental data, yielding:

$$\tau_{geo} = \varepsilon^{-1.716} \qquad [5\text{-}12]$$

Eq. [5-12] can be used in conjunction with Eq. [5-8] to obtain an actual effective diffusivity value for a given electrosprayed catalyst layer material with known porosity and pore size distributions, for use in modeling studies for instance.

5.6. Conclusion

In the present work, the electrospraying technique was explored to fabricate fuel cell catalyst layers with a PGM-free electrocatalysts. Several operating parameters that are known to have a strong impact (flow rate and distance) on the resulting porous structure were varied. The structures of the electrosprayed PGM-free catalyst layers were extensively characterized and it was confirmed that relatively simple adjustments to the production parameters resulted in catalyst layers with a variety of characteristics which makes it an appealing deposition technique to tailor the CL microstructure as suggested in the second case study in Chapter 3. The characterized properties included the thickness, porosity, pore size distribution, specific surface area and tortuosity. It was found that the electrosprayed layers generally resulted in thicker and more porous structure compared to the catalyst layer fabricated by other techniques such as air spray and ultrasonic spray. This was attributed to the fact that the electrospray technique enables the solvent to evaporate completely in-flight between the nozzle and the substrate resulting in thicker and looser structure. Also, the flow rate seemed to have more impact on the resulting structure than the needle-collector distance. Generally, slower flow rate resulted in thicker and more porous structures whereas higher flow rate resulted in thinner and more compact porous structures. The pore size distribution of the PGM-free catalysts synthesized by the sacrificial support method was evaluated to be bimodal at 10 nm and 70 nm. When the PGM-free catalysts were made into catalyst layers, most of the 70 nm pores disappeared and a new pore at $1-2$ μm range formed. It is highly likely that $1-2$ μm pores are inter-agglomerate pores formed after the deposition and 70 nm pores are mostly covered up by Nafion™ since Nafion™ can only intrude into pores larger than 30 nm.

The effective diffusivity of the non-PGM catalyst layers were experimentally measured and were higher for the slower flow rate and decreased with increasing flow rate. The effective diffusivities of the electrosprayed non-PGM catalyst layers were an order of magnitude higher than the conventional Pt/C catalyst layers which is attributed to larger inter-agglomerate pore size leading to a significantly reduced Knudsen effect. The geometric tortuosity was evaluated and was found to follow a similar trend to catalysts prepared by traditional methods.

Chapter 6 Concluding Remarks

6.1. Summary

This thesis aimed at providing better understanding of how to design, produce, and characterize improved non-PGM catalyst layers.

In Chapter 3, the optimal composition of non-PGM catalyst layers was examined using numerical simulation of fuel cell performance. A comprehensive parametric study was performed varying the catalyst loading between 0.5 to 6 $\mathrm{mg/cm^2}$ and the Nafion™ loading from 10% to 90%. The simulations were performed under realistic operating conditions, for example 70% relative humidity inlet gas. The optimum catalyst loading was found at 4.0 $\mathrm{mg/cm^2}$, however there was only a minimal improvement in the performance between 3.0 and 4.0 $\mathrm{mg/cm^2}$ catalyst layers. The optimum Nafion™ loading was generally higher than the ones reported in the literature. In the literature, the optimum Nafion™ loading was generally found at 50%, however, in this study 70% Nafion™ was found to be the optimum. This was attributed to the fact that all published works on non-PGM uses 100% RH inlet gas to enhance the Nafion™ conductivity but is more prone to water flooding. Therefore, higher porosity and less Nafion™ loading is favored to mitigate the water flooding, but this is not a practical approach for cell operation. Also, for 70% RH, proton conductivity of the non-PGM CL is expected to be lower due to lower RH, therefore requiring higher Nafion™ loading.

In Chapter 4, a novel method for measuring the effective diffusivity in thin porous materials was developed. The method was validated by measuring the binary diffusion coefficient of the working gases, i.e., nitrogen and air, in open space. The experimentally measured binary diffusivity was compared with the Chapman-Enskog correlation and they were in good agreement. The method was further validated by measuring the effective diffusivity of a pack of spheres. The effective diffusivity obtained for sphere packs agreed well with the reported effective diffusivity for these well-defined structures. It is well known that the Bruggeman correlation significantly overpredicts the effective diffusivity in complex porous materials like catalyst layers. However, in this study, it was found that when the assumptions of the Bruggeman equation are satisfied, namely the structure was composed of monomodal spheres, the Bruggeman correlation predicted the effective diffusivity well. For polydisperse spheres or non-spherical solids, the data could be fit using Archie's law, which has the same functional form as the Bruggeman equation, but the exponents are treated as a fitting parameter. Values of 1.75 were required, compared to 1.5 for the standard Bruggeman approximation.

In Chapter 5, the non-PGM catalysts were fabricated via electrospraying technique at various processing conditions. The resulting set of non-PGM catalyst layers were extensively examined with existing tools (porosity, BET, etc) as well as the diffusivity tool developed in Chapter 4. It was found that, with relatively simple adjustment to the process parameter, catalyst layers with substantially different structural characteristics were produced, suggesting that the ES technique holds promise for yielding an optimized layer for use in fuel cells. Electrosprayed non-PGM catalyst layers showed improved mass transport characteristics owing to higher porosity as well as larger average pore sizes. Also, in this study, tortuosity-porosity relationship was empirically derived.

6.2. Future works

6.2.1. Through-plane Effective Diffusivity/Tortuosity

Although, catalyst layers are generally regarded as isotropic and in-plane measurement of the effective diffusivity can principally be applied in all direction, it is still recommended that a new technique be developed for measuring the through-plane effective diffusivity. Currently, there are two methods that have the capability to measure the effective diffusivity in through-plane direction: 1) Loschmidt cell and 2) Diffusion bridge (Wicke-Kallenbach). In both techniques, samples are stacked in multiple layers to add resistances or to increase the mass flux, but multi-layers add additional resistances at the interface and make extracting the effective diffusivity challenging. Also, the diffusion bridge method requires careful control of the pressure and flow rates on each face of the sample. For thin materials, even a slight pressure gradient may cause convective mass transfer. Therefore, direct measurement of the through-plane effective diffusivity of a single layer is desired.

6.2.2. Measurement of Other Effective Properties

In Chapter 5, characterization mostly focused on the structure. The ability to measure other transport characteristics such as electrical, ionic and thermal conductivity would further improve the understanding of the electrospray non-PGM catalyst layers. This requires modification of the electrospraying setup. Currently, the non-PGM catalyst is electrosprayed on conducting substrates (i.e., ITO or copper sheet). However, to be able to measure in-plane electrical and thermal conductivities, the sample needs to be deposited on electrically and thermally insulating substrate, for example PTFE.

6.2.3. Hydrophobic Non-PGM Electrode

Non-PGM electrodes are more prone to water flooding than the conventional Pt/C due to their hydrophilic nature[173] and reduced water saturation have shown to improve the performance[103,174] as well as the durability.[175] One way to reduce the water saturation is to impregnate the electrode with hydrophobic material such as PTFE. However, this approach is likely to have adverse effect on the FC performance since PTFE does not participate in any transport process. PTFE is known to be electrically, ionically and thermally insulating and its presence reduces the porosity. A better approach would be either to synthesize hydrophobic catalysts directly or to surface-treat the catalyst as a post-processing step, though this might damage the Nafion™ ionomer.

6.2.4. Non-PGM Performance Test under Lower Relative Humidity

In Chapter 3, it was found that non-PGM catalyst layers had different optimal composition under lower relative humidity due to issues related to liquid water. It is recommended that the electrosprayed non-PGM electrodes with low to high Nafion™ content are fabricated and tested under lower humidity. The performance under lower humidity should be compared against a cell run with fully humidified air which would provide useful insights into practical design of the non-PGM catalyst layers.

References

(1) Bockris, J. O. A Hydrogen Economy. *Science* **1972**, *176* (4041), 1323–1323. https://doi.org/10.1126/science.176.4041.1323.

(2) H2@Scale: Enabling Affordable, Reliable, Clean, and Secure Energy across Sectors. U.S. Department of Energy.

(3) Deloitte; Ballard. Powering the Future of Mobility: Hydrogen and Fuel Cell Solutions for Transportation - Volume 1.Pdf.

(4) Toyota Mid-Size Cars https://www.toyota.com/mid-size-cars/.

(5) Shukla, S.; Domican, K.; Karan, K.; Bhattacharjee, S.; Secanell, M. Analysis of Low Platinum Loading Thin Polymer Electrolyte Fuel Cell Electrodes Prepared by Inkjet Printing. *Electrochimica Acta* **2015**, *156*, 289–300. https://doi.org/10.1016/j.electacta.2015.01.028.

(6) Martin, S.; Garcia-Ybarra, P. L.; Castillo, J. L. Ten-Fold Reduction from the State-of-the-Art Platinum Loading of Electrodes Prepared by Electrospraying for High Temperature Proton Exchange Membrane Fuel Cells. *Electrochem. Commun.* **2018**, *93*, 57–61. https://doi.org/10.1016/j.elecom.2018.06.007.

(7) Wang, C.; Cheng, X.; Yan, X.; Shen, S.; Ke, C.; Wei, G.; Zhang, J. Respective Influence of Ionomer Content on Local and Bulk Oxygen Transport Resistance in the Catalyst Layer of PEMFCs with Low Pt Loading. *J. Electrochem. Soc.* **2019**, *166* (4), F239–F245. https://doi.org/10.1149/2.0401904jes.

(8) Mukerjee, S.; Srinivasan, S.; Soriaga, M. P.; McBreen, J. Role of Structural and Electronic Properties of Pt and Pt Alloys on Electrocatalysis of Oxygen Reduction - An In Situ XANES and EXAFS Investigation. *J Electrochem Soc* **1995**, *142* (5), 14.

(9) Wang, C.; Chi, M.; Li, D.; Strmcnik, D.; van der Vliet, D.; Wang, G.; Komanicky, V.; Chang, K.-C.; Paulikas, A. P.; Tripkovic, D.; Pearson, J.; More, K. L.; Markovic, N. M.; Stamenkovic, V. R. Design and Synthesis of Bimetallic Electrocatalyst with Multilayered Pt-Skin Surfaces. *J. Am. Chem. Soc.* **2011**, *133* (36), 14396–14403. https://doi.org/10.1021/ja2047655.

(10) Han, B.; Carlton, C. E.; Kongkanand, A.; Kukreja, R. S.; Theobald, B. R.; Gan, L.; O'Malley, R.; Strasser, P.; Wagner, F. T.; Shao-Horn, Y. Record Activity and Stability of Dealloyed Bimetallic Catalysts for Proton Exchange Membrane Fuel Cells. *Energy Environ. Sci.* **2015**, *8* (1), 258–266. https://doi.org/10.1039/C4EE02144D.

(11) Caldwell, K. M.; Ramaker, D. E.; Jia, Q.; Mukerjee, S.; Ziegelbauer, J. M.; Kukreja, R. S.; Kongkanand, A. Spectroscopic *in Situ* Measurements of the Relative Pt Skin Thicknesses and Porosities of Dealloyed PtM $_n$ (Ni, Co) Electrocatalysts. *J. Phys. Chem. C* **2015**, *119* (1), 757–765. https://doi.org/10.1021/jp5098553.

(12) Shao, M.; Liu, P.; Zhang, J.; Adzic, R. Origin of Enhanced Activity in Palladium Alloy Electrocatalysts for Oxygen Reduction Reaction †. *J. Phys. Chem. B* **2007**, *111* (24), 6772–6775. https://doi.org/10.1021/jp0689971.

(13) Sasaki, K.; Naohara, H.; Cai, Y.; Choi, Y. M.; Liu, P.; Vukmirovic, M. B.; Wang, J. X.; Adzic, R. R. Core-Protected Platinum Monolayer Shell High-Stability Electrocatalysts for Fuel-Cell Cathodes. *Angew. Chem. Int. Ed.* **2010**, *49* (46), 8602–8607. https://doi.org/10.1002/anie.201004287.

(14) Strasser, P.; Koh, S.; Anniyev, T.; Greeley, J.; More, K.; Yu, C.; Liu, Z.; Kaya, S.;

Nordlund, D.; Ogasawara, H.; Toney, M. F.; Nilsson, A. Lattice-Strain Control of the Activity in Dealloyed Core–Shell Fuel Cell Catalysts. *Nat. Chem.* **2010**, *2* (6), 454–460. https://doi.org/10.1038/nchem.623.

(15) Adzic, R. R. Platinum Monolayer Electrocatalysts: Tunable Activity, Stability, and Self-Healing Properties. *Electrocatalysis* **2012**, *3* (3–4), 163–169. https://doi.org/10.1007/s12678-012-0112-3.

(16) Bliznakov, S. T.; Vukmirovic, M. B.; Yang, L.; Sutter, E. A.; Adzic, R. R. Pt Monolayer on Electrodeposited Pd Nanostructures: Advanced Cathode Catalysts for PEM Fuel Cells. *J. Electrochem. Soc.* **2012**, *159* (9), F501–F506. https://doi.org/10.1149/2.006209jes.

(17) Shao, M.; Peles, A.; Odell, J. Enhanced Oxygen Reduction Activity of Platinum Monolayer with a Gold Interlayer on Palladium. *J. Phys. Chem. C* **2014**, *118* (32), 18505–18509. https://doi.org/10.1021/jp503296s.

(18) Kuttiyiel, K. A.; Choi, Y.; Hwang, S.-M.; Park, G.-G.; Yang, T.-H.; Su, D.; Sasaki, K.; Liu, P.; Adzic, R. R. Enhancement of the Oxygen Reduction on Nitride Stabilized Pt-M (M=Fe, Co, and Ni) Core–Shell Nanoparticle Electrocatalysts. *Nano Energy* **2015**, *13*, 442–449. https://doi.org/10.1016/j.nanoen.2015.03.007.

(19) Tian, X.; Luo, J.; Nan, H.; Zou, H.; Chen, R.; Shu, T.; Li, X.; Li, Y.; Song, H.; Liao, S.; Adzic, R. R. Transition Metal Nitride Coated with Atomic Layers of Pt as a Low-Cost, Highly Stable Electrocatalyst for the Oxygen Reduction Reaction. *J. Am. Chem. Soc.* **2016**, *138* (5), 1575–1583. https://doi.org/10.1021/jacs.5b11364.

(20) Choi, S.-I.; Xie, S.; Shao, M.; Odell, J. H.; Lu, N.; Peng, H.-C.; Protsailo, L.; Guerrero, S.; Park, J.; Xia, X.; Wang, J.; Kim, M. J.; Xia, Y. Synthesis and Characterization of 9 Nm Pt–Ni Octahedra with a Record High Activity of 3.3 A/Mg $_{\mathrm{Pt}}$ for the Oxygen Reduction Reaction. *Nano Lett.* **2013**, *13* (7), 3420–3425. https://doi.org/10.1021/nl401881z.

(21) Li, D.; Wang, C.; Strmcnik, D. S.; Tripkovic, D. V.; Sun, X.; Kang, Y.; Chi, M.; Snyder, J. D.; van der Vliet, D.; Tsai, Y.; Stamenkovic, V. R.; Sun, S.; Markovic, N. M. Functional Links between Pt Single Crystal Morphology and Nanoparticles with Different Size and Shape: The Oxygen Reduction Reaction Case. *Energy Env. Sci* **2014**, *7* (12), 4061–4069. https://doi.org/10.1039/C4EE01564A.

(22) Choi, S.-I.; Shao, M.; Lu, N.; Ruditskiy, A.; Peng, H.-C.; Park, J.; Guerrero, S.; Wang, J.; Kim, M. J.; Xia, Y. Synthesis and Characterization of Pd@Pt–Ni Core–Shell Octahedra with High Activity toward Oxygen Reduction. *ACS Nano* **2014**, *8* (10), 10363–10371. https://doi.org/10.1021/nn5036894.

(23) Chen, C.; Kang, Y.; Huo, Z.; Zhu, Z.; Huang, W.; Xin, H. L.; Snyder, J. D.; Li, D.; Herron, J. A.; Mavrikakis, M.; Chi, M.; More, K. L.; Li, Y.; Markovic, N. M.; Somorjai, G. A.; Yang, P.; Stamenkovic, V. R. Highly Crystalline Multimetallic Nanoframes with Three-Dimensional Electrocatalytic Surfaces. *Science* **2014**, *343* (6177), 1339–1343. https://doi.org/10.1126/science.1249061.

(24) Park, J.; Wang, H.; Vara, M.; Xia, Y. Platinum Cubic Nanoframes with Enhanced Catalytic Activity and Durability Toward Oxygen Reduction. *ChemSusChem* **2016**, *9* (19), 2855–2861. https://doi.org/10.1002/cssc.201600984.

(25) Luo, S.; Tang, M.; Shen, P. K.; Ye, S. Atomic-Scale Preparation of Octopod Nanoframes with High-Index Facets as Highly Active and Stable Catalysts. *Adv. Mater.* **2017**, *29* (8). https://doi.org/10.1002/adma.201601687.

(26) Kongkanand, A.; Mathias, M. F. The Priority and Challenge of High-Power Performance of Low-Platinum Proton-Exchange Membrane Fuel Cells. *J. Phys. Chem. Lett.* **2016**, *7* (7),

1127–1137. https://doi.org/10.1021/acs.jpclett.6b00216.

(27) Proietti, E.; Jaouen, F.; Lefèvre, M.; Larouche, N.; Tian, J.; Herranz, J.; Dodelet, J.-P. Iron-Based Cathode Catalyst with Enhanced Power Density in Polymer Electrolyte Membrane Fuel Cells. *Nat. Commun.* **2011**, *2* (1), 416. https://doi.org/10.1038/ncomms1427.

(28) Chung, H. T.; Cullen, D. A.; Higgins, D.; Sneed, B. T.; Holby, E. F.; More, K. L.; Zelenay, P. Direct Atomic-Level Insight into the Active Sites of a High-Performance PGM-Free ORR Catalyst. *Science* **2017**, *357* (6350), 479–484. https://doi.org/10.1126/science.aan2255.

(29) Workman, M. J.; Dzara, M.; Ngo, C.; Pylypenko, S.; Serov, A.; McKinney, S.; Gordon, J.; Atanassov, P.; Artyushkova, K. Platinum Group Metal-Free Electrocatalysts: Effects of Synthesis on Structure and Performance in Proton-Exchange Membrane Fuel Cell Cathodes. *J. Power Sources* **2017**, *348*, 30–39. https://doi.org/10.1016/j.jpowsour.2017.02.067.

(30) Banham, D.; Choi, J.-Y.; Kishimoto, T.; Ye, S. Integrating PGM-Free Catalysts into Catalyst Layers and Proton Exchange Membrane Fuel Cell Devices. *Adv. Mater.* **2019**, 1804846. https://doi.org/10.1002/adma.201804846.

(31) Shui, J.; Chen, C.; Grabstanowicz, L.; Zhao, D.; Liu, D.-J. Highly Efficient Nonprecious Metal Catalyst Prepared with Metal–Organic Framework in a Continuous Carbon Nanofibrous Network. *Proc. Natl. Acad. Sci.* **2015**, *112* (34), 10629–10634. https://doi.org/10.1073/pnas.1507159112.

(32) Wang, J. X.; Springer, T. E.; Adzic, R. R. Dual-Pathway Kinetic Equation for the Hydrogen Oxidation Reaction on Pt Electrodes. *J. Electrochem. Soc.* **2006**, *153* (9), A1732–A1740.

(33) Wang, J. X.; Zhang, J.; Adzic, R. R. Double-Trap Kinetic Equation for the Oxygen Reduction Reaction on Pt(111) in Acidic Media [†]. *J. Phys. Chem. A* **2007**, *111* (49), 12702–12710. https://doi.org/10.1021/jp076104e.

(34) Moore, M.; Putz, A.; Secanell, M. Investigation of the ORR Using the Double-Trap Intrinsic Kinetic Model. *J. Electrochem. Soc.* **2013**, *160* (6), F670–F681. https://doi.org/10.1149/2.123306jes.

(35) Srinivasan, S.; Ticianelli, E. A.; Derouin, C. R.; Redondo, A. Advances in Solid Polymer Electrolyte Fuel Cell Technology with Low Platinum Loading Electrodes. *J. Power Sources* **1988**, *22* (3–4), 359–375. https://doi.org/10.1016/0378-7753(88)80030-2.

(36) Wu, G.; More, K. L.; Johnston, C. M.; Zelenay, P. High-Performance Electrocatalysts for Oxygen Reduction Derived from Polyaniline, Iron, and Cobalt. *Science* **2011**, *332* (6028), 443–447. https://doi.org/10.1126/science.1200832.

(37) Jasinski, R. A New Fuel Cell Cathode Catalyst. *Nature* **1964**, *201*, 1212–1213. https://doi.org/10.1038/2011212a0.

(38) Jahnke, H.; Schönborn, M.; Zimmermann, G. Organic Dyestuffs as Catalysts for Fuel Cells. In *Physical and Chemical Applications of Dyestuffs*; Schäfer, F. P., Gerischer, H., Willig, F., Meier, H., Jahnke, H., Schönborn, M., Zimmermann, G., Eds.; Topics in Current Chemistry; Springer: Berlin/Heidelberg, 1976; Vol. 61, pp 133–181. https://doi.org/10.1007/BFb0046059.

(39) Gupta, S.; Tryk, D.; Bae, I.; Aldred, W.; Yeager, E. Heat-Treated Polyacrylonitrile-Based Catalysts for Oxygen Electroreduction. *J. Appl. Electrochem.* **1989**, *19* (1), 19–27. https://doi.org/10.1007/BF01039385.

(40) Lefèvre, M.; Proietti, E.; Jaouen, F.; Dodelet, J.-P. Iron-Based Catalysts with Improved Oxygen Reduction Activity in Polymer Electrolyte Fuel Cells. *Science* **2009**, *324* (5923),

71–74. https://doi.org/10.1126/science.1170051.

(41) Workman, M. J.; Serov, A.; Tsui, L.; Atanassov, P.; Artyushkova, K. Fe–N–C Catalyst Graphitic Layer Structure and Fuel Cell Performance. *ACS Energy Lett.* **2017**, *2* (7), 1489–1493. https://doi.org/10.1021/acsenergylett.7b00391.

(42) Banham, D.; Kishimoto, T.; Zhou, Y.; Sato, T.; Bai, K.; Ozaki, J.; Imashiro, Y.; Ye, S. Critical Advancements in Achieving High Power and Stable Nonprecious Metal Catalyst–Based MEAs for Real-World Proton Exchange Membrane Fuel Cell Applications. *Sci. Adv.* **2018**, *4* (3), eaar7180. https://doi.org/10.1126/sciadv.aar7180.

(43) Deng, Y.; Chi, B.; Li, J.; Wang, G.; Zheng, L.; Shi, X.; Cui, Z.; Du, L.; Liao, S.; Zang, K.; Luo, J.; Hu, Y.; Sun, X. Atomic Fe-Doped MOF-Derived Carbon Polyhedrons with High Active-Center Density and Ultra-High Performance toward PEM Fuel Cells. *Adv. Energy Mater.* **2019**, *9* (13), 1802856. https://doi.org/10.1002/aenm.201802856.

(44) Zhan, Y.; Xie, F.; Zhang, H.; Jin, Y.; Meng, H.; Chen, J.; Sun, X. Highly Dispersed Nonprecious Metal Catalyst for Oxygen Reduction Reaction in Proton Exchange Membrane Fuel Cells. *ACS Appl. Mater. Interfaces* **2020**, *12* (15), 17481–17491. https://doi.org/10.1021/acsami.0c00126.

(45) Uddin, A.; Dunsmore, L.; Zhang, H.; Hu, L.; Wu, G.; Litster, S. High Power Density Platinum Group Metal-Free Cathodes for Polymer Electrolyte Fuel Cells. *ACS Appl. Mater. Interfaces* **2020**, *12* (2), 2216–2224. https://doi.org/10.1021/acsami.9b13945.

(46) Larouche, N.; Chenitz, R.; Lefèvre, M.; Proietti, E.; Dodelet, J.-P. Activity and Stability in Proton Exchange Membrane Fuel Cells of Iron-Based Cathode Catalysts Synthesized with Addition of Carbon Fibers. *Electrochimica Acta* **2014**, *115*, 170–182. https://doi.org/10.1016/j.electacta.2013.10.102.

(47) Stariha, S.; Artyushkova, K.; Serov, A.; Atanassov, P. Non-PGM Membrane Electrode Assemblies: Optimization for Performance. *Int. J. Hydrog. Energy* **2015**, *40* (42), 14676–14682. https://doi.org/10.1016/j.ijhydene.2015.05.185.

(48) Stariha, S.; Artyushkova, K.; Workman, M. J.; Serov, A.; Mckinney, S.; Halevi, B.; Atanassov, P. PGM-Free Fe-N-C Catalysts for Oxygen Reduction Reaction: Catalyst Layer Design. *J. Power Sources* **2016**, *326*, 43–49. https://doi.org/10.1016/j.jpowsour.2016.06.098.

(49) Serov, A.; Workman, M. J.; Artyushkova, K.; Atanassov, P.; McCool, G.; McKinney, S.; Romero, H.; Halevi, B.; Stephenson, T. Highly Stable Precious Metal-Free Cathode Catalyst for Fuel Cell Application. *J. Power Sources* **2016**, *327*, 557–564. https://doi.org/10.1016/j.jpowsour.2016.07.087.

(50) Komini Babu, S.; Chung, H. T.; Zelenay, P.; Litster, S. Resolving Electrode Morphology's Impact on Platinum Group Metal-Free Cathode Performance Using Nano-CT of 3D Hierarchical Pore and Ionomer Distribution. *ACS Appl. Mater. Interfaces* **2016**, *8* (48), 32764–32777. https://doi.org/10.1021/acsami.6b08844.

(51) Taylor, R.; Krishna, R. *Multicomponent Mass Transfer*; Wiley, 1993.

(52) Krishna, R.; Wesselingh, J. A. The Maxwell-Stefan Approach to Mass Transfer. *Chem. Eng. Sci.* **1997**, *52* (6), 861–911. https://doi.org/10.1016/S0009-2509(96)00458-7.

(53) Fick, A. Ueber Diffusion. *Ann. Phys. Chem.* **1855**, *170* (1), 59–86. https://doi.org/10.1002/andp.18551700105.

(54) Mason, E. A.; Malinauskas, A. P. *Gas Transport in Porous Media: The Dusty-Gas Model*; Elsevier: Amsterdam, 1983.

(55) Sabharwal, M.; Pant, L. M.; Putz, A.; Susac, D.; Jankovic, J.; Secanell, M. Analysis of

Catalyst Layer Microstructures: From Imaging to Performance. *Fuel Cells* **2016**, *16* (6), 734–753. https://doi.org/10.1002/fuce.201600008.

(56) Zhou, J.; Putz, A.; Secanell, M. A Mixed Wettability Pore Size Distribution Based Mathematical Model for Analyzing Two-Phase Flow in Porous Electrodes: I. Mathematical Model. *J. Electrochem. Soc.* **2017**, *164* (6), F530–F539. https://doi.org/10.1149/2.0381706jes.

(57) Sabharwal, M.; Pant, L. M.; Patel, N.; Secanell, M. Computational Analysis of Gas Transport in Fuel Cell Catalyst Layer under Dry and Partially Saturated Conditions. *J. Electrochem. Soc.* **2019**, *166* (7), F3065–F3080. https://doi.org/10.1149/2.0081907jes.

(58) Wang, Y.; Wang, S.; Liu, S.; Li, H.; Zhu, K. Three-Dimensional Simulation of a PEM Fuel Cell with Experimentally Measured through-Plane Gas Effective Diffusivity Considering Knudsen Diffusion and the Liquid Water Effect in Porous Electrodes. *Electrochimica Acta* **2019**, *318*, 770–782. https://doi.org/10.1016/j.electacta.2019.06.120.

(59) Kosakian, A.; Urbina, L. P.; Heaman, A.; Secanell, M. Understanding Single-Phase Water-Management Signatures in Fuel-Cell Impedance Spectra: A Numerical Study. *Electrochimica Acta* **2020**, *350*, 136204. https://doi.org/10.1016/j.electacta.2020.136204.

(60) Whitaker, S. Flow in Porous Media I: A Theoretical Derivation of Darcy's Law. *Transp. Porous Media* **1986**, *1* (1), 3–25. https://doi.org/10.1007/BF01036523.

(61) Kerkhof, P. J. A. M. A Modified Maxwell-Stefan Model for Transport through Inert Membranes: The Binary Friction Model. *Chem. Eng. J. Biochem. Eng. J.* **1996**, *64* (3), 319–343. https://doi.org/10.1016/S0923-0467(96)03134-X.

(62) Pant, L. M.; Mitra, S. K.; Secanell, M. Absolute Permeability and Knudsen Diffusivity Measurements in PEMFC Gas Diffusion Layers and Micro Porous Layers. *J. Power Sources* **2012**, *206*, 153–160. https://doi.org/10.1016/j.jpowsour.2012.01.099.

(63) Pant, L. M.; Mitra, S. K.; Secanell, M. A Generalized Mathematical Model to Study Gas Transport in PEMFC Porous Media. *Int. J. Heat Mass Transf.* **2013**, *58* (1–2), 70–79. https://doi.org/10.1016/j.ijheatmasstransfer.2012.11.023.

(64) Hirschfelder, J. O.; Bird, R. Byron.; Spotz, E. L. The Transport Properties of Gases and Gaseous Mixtures. II. *Chem. Rev.* **1949**, *44* (1), 205–231. https://doi.org/10.1021/cr60137a012.

(65) Kim, Y.; Gostick, J. T. Measuring Effective Diffusivity in Porous Media with a Gasket-Free, Radial Arrangement. *Int. J. Heat Mass Transf.* **2019**, *129*, 1023–1030. https://doi.org/10.1016/j.ijheatmasstransfer.2018.10.054.

(66) Kramer, D.; Freunberger, S. A.; Flückiger, R.; Schneider, I. A.; Wokaun, A.; Büchi, F. N.; Scherer, G. G. Electrochemical Diffusimetry of Fuel Cell Gas Diffusion Layers. *J. Electroanal. Chem.* **2008**, *612* (1), 63–77. https://doi.org/10.1016/j.jelechem.2007.09.014.

(67) Flückiger, R.; Freunberger, S. A.; Kramer, D.; Wokaun, A.; Scherer, G. G.; Büchi, F. N. Anisotropic, Effective Diffusivity of Porous Gas Diffusion Layer Materials for PEFC. *Electrochimica Acta* **2008**, *54* (2), 551–559. https://doi.org/10.1016/j.electacta.2008.07.034.

(68) LaManna, J. M.; Kandlikar, S. G. Determination of Effective Water Vapor Diffusion Coefficient in Pemfc Gas Diffusion Layers. *Int. J. Hydrog. Energy* **2011**, *36* (8), 5021–5029. https://doi.org/10.1016/j.ijhydene.2011.01.036.

(69) Rashapov, R.; Imami, F.; Gostick, J. T. A Method for Measuring In-Plane Effective Diffusivity in Thin Porous Media. *Int. J. Heat Mass Transf.* **2015**, *85*, 367–374. https://doi.org/10.1016/j.ijheatmasstransfer.2015.01.101.

(70) Rashapov, R. R.; Gostick, J. T. In-Plane Effective Diffusivity in PEMFC Gas Diffusion Layers. *Transp. Porous Media* **2016**, *115* (3), 411–433. https://doi.org/10.1007/s11242-016-0648-4.

(71) Martínez, M. J.; Shimpalee, S.; Van Zee, J. W. Measurement of MacMullin Numbers for PEMFC Gas-Diffusion Media. *J. Electrochem. Soc.* **2009**, *156* (1), B80. https://doi.org/10.1149/1.3005564.

(72) Wang, Y.; Wang, S. Evaluation and Modeling of PEM Fuel Cells with the Bruggeman Correlation under Various Tortuosity Factors. *Int. J. Heat Mass Transf.* **2017**, *105*, 18–23. https://doi.org/10.1016/j.ijheatmasstransfer.2016.09.030.

(73) Secanell, M.; Songprakorp, R.; Suleman, A.; Djilali, N. Multi-Objective Optimization of a Polymer Electrolyte Fuel Cell Membrane Electrode Assembly. *Energy Environ. Sci.* **2008**, *1* (3), 378. https://doi.org/10.1039/b804654a.

(74) Secanell, M.; Songprakorp, R.; Djilali, N.; Suleman, A. Optimization of a Proton Exchange Membrane Fuel Cell Membrane Electrode Assembly. *Struct. Multidiscip. Optim.* **2010**, *40* (1–6), 563–583. https://doi.org/10.1007/s00158-009-0387-z.

(75) Baker, D. R.; Caulk, D. A.; Neyerlin, K. C.; Murphy, M. W. Measurement of Oxygen Transport Resistance in PEM Fuel Cells by Limiting Current Methods. *J. Electrochem. Soc.* **2009**, *156* (9), B991. https://doi.org/10.1149/1.3152226.

(76) Mangal, P.; Pant, L. M.; Carrigy, N.; Dumontier, M.; Zingan, V.; Mitra, S.; Secanell, M. Experimental Study of Mass Transport in PEMFCs: Through Plane Permeability and Molecular Diffusivity in GDLs. *Electrochimica Acta* **2015**, *167*, 160–171. https://doi.org/10.1016/j.electacta.2015.03.100.

(77) Zamel, N.; Li, X.; Shen, J. Correlation for the Effective Gas Diffusion Coefficient in Carbon Paper Diffusion Media. *Energy Fuels* **2009**, *23* (12), 6070–6078. https://doi.org/10.1021/ef900653x.

(78) Zamel, N.; Astrath, N. G. C.; Li, X.; Shen, J.; Zhou, J.; Astrath, F. B. G.; Wang, H.; Liu, Z. S. Experimental Measurements of Effective Diffusion Coefficient of Oxygen-Nitrogen Mixture in PEM Fuel Cell Diffusion Media. *Chem. Eng. Sci.* **2010**, *65* (2), 931–937. https://doi.org/10.1016/j.ces.2009.09.044.

(79) Tranter, T. G.; Stogornyuk, P.; Gostick, J. T.; Burns, A. D.; Gale, W. F. A Method for Measuring Relative In-Plane Diffusivity of Thin and Partially Saturated Porous Media: An Application to Fuel Cell Gas Diffusion Layers. *Int. J. Heat Mass Transf.* **2017**, *110*, 132–141. https://doi.org/10.1016/j.ijheatmasstransfer.2017.02.096.

(80) Shukla, S.; Stanier, D.; Saha, M. S.; Stumper, J.; Secanell, M. Analysis of Inkjet Printed PEFC Electrodes with Varying Platinum Loading. *J. Electrochem. Soc.* **2016**, *163* (7), F677–F687. https://doi.org/10.1149/2.1111607jes.

(81) Chan, C.; Zamel, N.; Li, X.; Shen, J. Experimental Measurement of Effective Diffusion Coefficient of Gas Diffusion Layer/Microporous Layer in PEM Fuel Cells. *Electrochimica Acta* **2012**, *65*, 13–21. https://doi.org/10.1016/j.electacta.2011.12.110.

(82) Carrigy, N. B.; Pant, L. M.; Mitra, S.; Secanell, M. Knudsen Diffusivity and Permeability of PEMFC Microporous Coated Gas Diffusion Layers for Different Polytetrafluoroethylene Loadings. *J. Electrochem. Soc.* **2013**, *160* (2), F81–F89. https://doi.org/10.1149/2.036302jes.

(83) Shen, J.; Zhou, J.; Astrath, N. G. C.; Navessin, T.; Liu, Z.-S. (Simon); Lei, C.; Rohling, J. H.; Bessarabov, D.; Knights, S.; Ye, S. Measurement of Effective Gas Diffusion Coefficients of Catalyst Layers of PEM Fuel Cells with a Loschmidt Diffusion Cell. *J.*

Power Sources **2011**, *196* (2), 674–678. https://doi.org/10.1016/j.jpowsour.2010.07.086.

(84) Salari, S.; Stumper, J.; Bahrami, M. Direct Measurement and Modeling Relative Gas Diffusivity of PEMFC Catalyst Layers: The Effect of Ionomer to Carbon Ratio, Operating Temperature, Porosity, and Pore Size Distribution. *Int. J. Hydrog. Energy* **2018**, *43* (34), 16704–16718. https://doi.org/10.1016/j.ijhydene.2018.07.035.

(85) Salari, S.; Tam, M.; McCague, C.; Stumper, J.; Bahrami, M. The Ex-Situ and in-Situ Gas Diffusivities of Polymer Electrolyte Membrane Fuel Cell Catalyst Layer and Contribution of Primary Pores, Secondary Pores, Ionomer and Water to the Total Oxygen Diffusion Resistance. *J. Power Sources* **2019**, 227479. https://doi.org/10.1016/j.jpowsour.2019.227479.

(86) Yu, Z.; Carter, R. N. Measurement of Effective Oxygen Diffusivity in Electrodes for Proton Exchange Membrane Fuel Cells. *J. Power Sources* **2010**, *195* (4), 1079–1084. https://doi.org/10.1016/j.jpowsour.2009.08.065.

(87) Inoue, G.; Yokoyama, K.; Ooyama, J.; Terao, T.; Tokunaga, T.; Kubo, N.; Kawase, M. Theoretical Examination of Effective Oxygen Diffusion Coefficient and Electrical Conductivity of Polymer Electrolyte Fuel Cell Porous Components. *J. Power Sources* **2016**, *327*, 610–621. https://doi.org/10.1016/j.jpowsour.2016.07.107.

(88) Rietveld, I. B.; Kobayashi, K.; Yamada, H.; Matsushige, K. Electrospray Deposition, Model, and Experiment: Toward General Control of Film Morphology. *J. Phys. Chem. B* **2006**, 14.

(89) Taylor, G. I. Disintegration of Water Drops in an Electric Field. *Proc. R. Soc. A* **1964**, *280* (1382), 383. https://doi.org/10.1098/rspa.1964.0151.

(90) Cloupeau, M.; Prunet-Foch, B. Electrostatic Spraying of Liquids: Main Functioning Modes. *J. Electrost.* **1990**, *25* (2), 165–184. https://doi.org/10.1016/0304-3886(90)90025-Q.

(91) Baturina, O. A.; Wnek, G. E. Characterization of Proton Exchange Membrane Fuel Cells with Catalyst Layers Obtained by Electrospraying. *Electrochem. Solid-State Lett.* **2005**, *8* (6), A267. https://doi.org/10.1149/1.1895267.

(92) Benítez, R.; Soler, J.; Daza, L. Novel Method for Preparation of PEMFC Electrodes by the Electrospray Technique. *J. Power Sources* **2005**, *151*, 108–113. https://doi.org/10.1016/j.jpowsour.2005.02.047.

(93) Chaparro, A. M.; Benítez, R.; Gubler, L.; Scherer, G. G.; Daza, L. Study of Membrane Electrode Assemblies for PEMFC, with Cathodes Prepared by the Electrospray Method. *J. Power Sources* **2007**, *169* (1), 77–84. https://doi.org/10.1016/j.jpowsour.2007.01.044.

(94) Chaparro, A. M.; Gallardo, B.; Folgado, M. A.; Martín, A. J.; Daza, L. PEMFC Electrode Preparation by Electrospray: Optimization of Catalyst Load and Ionomer Content. *Catal. Today* **2009**, *143* (3–4), 237–241. https://doi.org/10.1016/j.cattod.2008.12.003.

(95) Chaparro, A. M.; Folgado, M. A.; Ferreira-Aparicio, P.; Martín, A. J.; Alonso-Álvarez, I.; Daza, L. Properties of Catalyst Layers for PEMFC Electrodes Prepared by Electrospray Deposition. *J. Electrochem. Soc.* **2010**, *157* (7), B993. https://doi.org/10.1149/1.3425740.

(96) Martin, S.; Garcia-Ybarra, P. L.; Castillo, J. L. Electrospray Deposition of Catalyst Layers with Ultra-Low Pt Loadings for PEM Fuel Cells Cathodes. *J. Power Sources* **2010**, *195* (9), 2443–2449. https://doi.org/10.1016/j.jpowsour.2009.11.092.

(97) Martin, S.; Garcia-Ybarra, P. L.; Castillo, J. L. High Platinum Utilization in Ultra-Low Pt Loaded PEM Fuel Cell Cathodes Prepared by Electrospraying. *Int. J. Hydrog. Energy* **2010**, *35* (19), 10446–10451. https://doi.org/10.1016/j.ijhydene.2010.07.069.

(98) Chaparro, A. M.; Ferreira-Aparicio, P.; Folgado, M. A.; Martín, A. J.; Daza, L. Catalyst

Layers for Proton Exchange Membrane Fuel Cells Prepared by Electrospray Deposition on Nafion Membrane. *J. Power Sources* **2011**, *196* (9), 4200–4208. https://doi.org/10.1016/j.jpowsour.2010.09.096.

(99) Takahashi, K.; Kakinuma, K.; Uchida, M. Improvement of Cell Performance in Low-Pt-Loading PEFC Cathode Catalyst Layers Prepared by the Electrospray Method. *J. Electrochem. Soc.* **2016**, *163* (10), F1182–F1188. https://doi.org/10.1149/2.0611610jes.

(100) Conde, J. J.; Folgado, M. A.; Ferreira-Aparicio, P.; Chaparro, A. M.; Chowdhury, A.; Kusoglu, A.; Cullen, D.; Weber, A. Z. Mass-Transport Properties of Electrosprayed Pt/C Catalyst Layers for Polymer-Electrolyte Fuel Cells. *J. Power Sources* **2019**, *427*, 250–259. https://doi.org/10.1016/j.jpowsour.2019.04.079.

(101) Li, J.; Ghoshal, S.; Liang, W.; Sougrati, M.-T.; Jaouen, F.; Halevi, B.; McKinney, S.; McCool, G.; Ma, C.; Yuan, X.; Ma, Z.-F.; Mukerjee, S.; Jia, Q. Structural and Mechanistic Basis for the High Activity of Fe–N–C Catalysts toward Oxygen Reduction. *Energy Environ. Sci.* **2016**, *9* (7), 2418–2432. https://doi.org/10.1039/C6EE01160H.

(102) Zhang, C.; Wang, Y.-C.; An, B.; Huang, R.; Wang, C.; Zhou, Z.; Lin, W. Networking Pyrolyzed Zeolitic Imidazolate Frameworks by Carbon Nanotubes Improves Conductivity and Enhances Oxygen-Reduction Performance in Polymer-Electrolyte-Membrane Fuel Cells. *Adv. Mater.* **2017**, *29* (4), 1604556. https://doi.org/10.1002/adma.201604556.

(103) Babu, S. K.; Chung, H. T.; Zelenay, P.; Litster, S. Modeling Electrochemical Performance of the Hierarchical Morphology of Precious Group Metal-Free Cathode for Polymer Electrolyte Fuel Cell. *J. Electrochem. Soc.* **2017**, *164* (9), F1037–F1049. https://doi.org/10.1149/2.0041712jes.

(104) Jaouen, F.; Jones, D.; Coutard, N.; Artero, V.; Strasser, P.; Kucernak, A. Toward Platinum Group Metal-Free Catalysts for Hydrogen/Air Proton-Exchange Membrane Fuel Cells. *Johns. Matthey Technol. Rev.* **2018**, *62* (2), 231–255. https://doi.org/10.1595/205651318X696828.

(105) Artyushkova, K.; Habel-Rodriguez, D.; Olson, T. S.; Atanassov, P. Optimization of Ink Composition Based on a Non-Platinum Cathode for Single Membrane Electrode Assembly Proton Exchange Membrane Fuel Cells. *J. Power Sources* **2013**, *226*, 112–121. https://doi.org/10.1016/j.jpowsour.2012.10.062.

(106) Bhaiya, M.; Putz, A.; Secanell, M. Analysis of Non-Isothermal Effects on Polymer Electrolyte Fuel Cell Electrode Assemblies. *Electrochimica Acta* **2014**, *147*, 294–309. https://doi.org/10.1016/j.electacta.2014.09.051.

(107) Secanell, M.; Karan, K.; Suleman, A.; Djilali, N. Optimal Design of Ultralow-Platinum PEMFC Anode Electrodes. *J. Electrochem. Soc.* **2008**, *155* (2), B125. https://doi.org/10.1149/1.2806171.

(108) Sun, W.; Peppley, B. A.; Karan, K. An Improved Two-Dimensional Agglomerate Cathode Model to Study the Influence of Catalyst Layer Structural Parameters. *Electrochimica Acta* **2005**, *50* (16–17), 3359–3374. https://doi.org/10.1016/j.electacta.2004.12.009.

(109) Parthasarathy, A. Temperature Dependence of the Electrode Kinetics of Oxygen Reduction at the Platinum/Nafion® Interface—A Microelectrode Investigation. *J. Electrochem. Soc.* **1992**, *139* (9), 2530. https://doi.org/10.1149/1.2221258.

(110) DOE Technical Targets for Polymer Electrolyte Membrane Fuel Cell Components https://www.energy.gov/eere/fuelcells/doe-technical-targets-polymer-electrolyte-membrane-fuel-cell-components.

(111) Antolini, E.; Giorgi, L.; Pozio, A.; Passalacqua, E. Influence of Nafion Loading in the

Catalyst Layer of Gas-Diffusion Electrodes for PEFC. *J. Power Sources* **1999**, *77* (2), 136–142. https://doi.org/10.1016/S0378-7753(98)00186-4.

(112) Passalacqua, E.; Lufrano, F.; Squadrito, G.; Patti, A.; Giorgi, L. Nafion Content in the Catalyst Layer of Polymer Electrolyte Fuel Cells: Effects on Structure and Performance. *Electrochimica Acta* **2001**, *46* (6), 799–805. https://doi.org/10.1016/S0013-4686(00)00679-4.

(113) Qi, Z.; Kaufman, A. Low Pt Loading High Performance Cathodes for PEM Fuel Cells. *J. Power Sources* **2003**, *113* (1), 37–43. https://doi.org/10.1016/S0378-7753(02)00477-9.

(114) Leonard, N. D.; Artyushkova, K.; Halevi, B.; Serov, A.; Atanassov, P.; Barton, S. C. Modeling of Low-Temperature Fuel Cell Electrodes Using Non-Precious Metal Catalysts. *J. Electrochem. Soc.* **2015**, *162* (10), F1253–F1261. https://doi.org/10.1149/2.0311510jes.

(115) Schweiss, R.; Meiser, C.; Damjanovic, T.; Galbati, I.; Haak, N. SIGRACET® Gas Diffusion Layers for PEM Fuel Cells,. SGL Group.

(116) Rashapov, R. R.; Unno, J.; Gostick, J. T. Characterization of PEMFC Gas Diffusion Layer Porosity. *J. Electrochem. Soc.* **2015**, *162* (6), F603–F612. https://doi.org/10.1149/2.0921506jes.

(117) Tomadakis, M. M.; Sotirchos, S. V. Effective Kundsen Diffusivities in Structures of Randomly Overlapping Fibers. *AIChE J.* **1991**, *37* (1), 74–86. https://doi.org/10.1002/aic.690370107.

(118) Flückiger, R.; Freunberger, S. A.; Kramer, D.; Wokaun, A.; Scherer, G. G.; Büchi, F. N. Anisotropic, Effective Diffusivity of Porous Gas Diffusion Layer Materials for PEFC. *Electrochimica Acta* **2008**, *54* (2), 551–559. https://doi.org/10.1016/j.electacta.2008.07.034.

(119) Rashapov, R. R.; Gostick, J. T. In-Plane Effective Diffusivity in PEMFC Gas Diffusion Layers. *Transp. Porous Media* **2016**, *115* (3), 411–433. https://doi.org/10.1007/s11242-016-0648-4.

(120) Zamel, N.; Litovsky, E.; Li, X.; Kleiman, J. Measurement of the Through-Plane Thermal Conductivity of Carbon Paper Diffusion Media for the Temperature Range from −50 to +120°C. *Int. J. Hydrog. Energy* **2011**, *36* (19), 12618–12625. https://doi.org/10.1016/j.ijhydene.2011.06.097.

(121) Zamel, N.; Litovsky, E.; Shakhshir, S.; Li, X.; Kleiman, J. Measurement of In-Plane Thermal Conductivity of Carbon Paper Diffusion Media in the Temperature Range of −20°C to +120°C. *Appl. Energy* **2011**, *88* (9), 3042–3050. https://doi.org/10.1016/j.apenergy.2011.02.037.

(122) Dobson, P.; Lei, C.; Navessin, T.; Secanell, M. Characterization of the PEM Fuel Cell Catalyst Layer Microstructure by Nonlinear Least-Squares Parameter Estimation. *J. Electrochem. Soc.* **2012**, *159* (5), B514–B523. https://doi.org/10.1149/2.041205jes.

(123) Peron, J.; Mani, A.; Zhao, X.; Edwards, D.; Adachi, M.; Soboleva, T.; Shi, Z.; Xie, Z.; Navessin, T.; Holdcroft, S. Properties of Nafion® NR-211 Membranes for PEMFCs. *J. Membr. Sci.* **2010**, *356* (1–2), 44–51. https://doi.org/10.1016/j.memsci.2010.03.025.

(124) Motupally, S.; Becker, A. J.; Weidner, J. W. Diffusion of Water in Nafion 115 Membranes. *J. Electrochem. Soc.* **2000**, *147* (9), 3171–3177. https://doi.org/10.1149/1.1393879.

(125) Springer, T. E. Polymer Electrolyte Fuel Cell Model. *J. Electrochem. Soc.* **1991**, *138* (8), 2334. https://doi.org/10.1149/1.2085971.

(126) Kim, S.; Mench, M. M. Investigation of Temperature-Driven Water Transport in Polymer

Electrolyte Fuel Cell: Thermo-Osmosis in Membranes. *J. Membr. Sci.* **2009**, *328* (1–2), 113–120. https://doi.org/10.1016/j.memsci.2008.11.043.

(127) Khandelwal, M.; Mench, M. M. Direct Measurement of Through-Plane Thermal Conductivity and Contact Resistance in Fuel Cell Materials. *J. Power Sources* **2006**, *161* (2), 1106–1115. https://doi.org/10.1016/j.jpowsour.2006.06.092.

(128) Burheim, O.; Vie, P. J. S.; Pharoah, J. G.; Kjelstrup, S. Ex Situ Measurements of Through-Plane Thermal Conductivities in a Polymer Electrolyte Fuel Cell. *J. Power Sources* **2010**, *195* (1), 249–256. https://doi.org/10.1016/j.jpowsour.2009.06.077.

(129) Liu, Y.; Murphy, M. W.; Baker, D. R.; Gu, W.; Ji, C.; Jorne, J.; Gasteiger, H. A. Proton Conduction and Oxygen Reduction Kinetics in PEM Fuel Cell Cathodes: Effects of Ionomer-to-Carbon Ratio and Relative Humidity. *J. Electrochem. Soc.* **2009**, *156* (8), B970. https://doi.org/10.1149/1.3143965.

(130) Pharoah, J. G.; Karan, K.; Sun, W. On Effective Transport Coefficients in PEM Fuel Cell Electrodes: Anisotropy of the Porous Transport Layers. *J. Power Sources* **2006**, *161* (1), 214–224. https://doi.org/10.1016/j.jpowsour.2006.03.093.

(131) Zhang, L.; Bi, H. T.; Wilkinson, D. P.; Stumper, J.; Wang, H. Gas-Liquid Two-Phase Flow Patterns in Parallel Channels for Fuel Cells. *J. Power Sources* **2008**, *183* (2), 643–650. https://doi.org/10.1016/j.jpowsour.2008.05.080.

(132) Anderson, R.; Zhang, L.; Ding, Y.; Blanco, M.; Bi, X.; Wilkinson, D. P. A Critical Review of Two-Phase Flow in Gas Flow Channels of Proton Exchange Membrane Fuel Cells. *J. Power Sources* **2010**, *195* (15), 4531–4553. https://doi.org/10.1016/j.jpowsour.2009.12.123.

(133) Zarrin, H.; Higgins, D.; Jun, Y.; Chen, Z.; Fowler, M. Functionalized Graphene Oxide Nanocomposite Membrane for Low Humidity and High Temperature Proton Exchange Membrane Fuel Cells. *J. Phys. Chem. C* **2011**, *115* (42), 20774–20781. https://doi.org/10.1021/jp204610j.

(134) Cheng, F.; Chen, J. Metal-Air Batteries: From Oxygen Reduction Electrochemistry to Cathode Catalysts. *Chem. Soc. Rev.* **2012**, *41* (6), 2172–2192. https://doi.org/10.1039/c1cs15228a.

(135) Smith, K. C. Theoretical Evaluation of Electrochemical Cell Architectures Using Cation Intercalation Electrodes for Desalination. *Electrochimica Acta* **2017**, *230*, 333–341. https://doi.org/10.1016/j.electacta.2017.02.006.

(136) Liu, S.; Smith, K. C. Quantifying the Trade-Offs between Energy Consumption and Salt Removal Rate in Membrane-Free Cation Intercalation Desalination. *Electrochimica Acta* **2018**, *271*, 652–665. https://doi.org/10.1016/j.electacta.2018.03.065.

(137) Koros, W. J.; Mahajan, R. Pushing the Limits on Possibilities for Large Scale Gas Separation: Which Strategies? *J. Membr. Sci.* **2001**, *181* (1), 141. https://doi.org/10.1016/S0376-7388(00)00676-1.

(138) Cabot, A.; Arbiol, J.; Cornet, A.; Morante, J. R.; Chen, F.; Liu, M. Mesoporous Catalytic Filters for Semiconductor Gas Sensors. *Thin Solid Films* **2003**, *436* (1), 64–69. https://doi.org/10.1016/S0040-6090(03)00510-8.

(139) Sakai, G.; Matsunaga, N.; Shimanoe, K.; Yamazoe, N. Theory of Gas-Diffusion Controlled Sensitivity for Thin Film Semiconductor Gas Sensor. *Sens. Actuators B Chem.* **2001**, *80* (2), 125–131. https://doi.org/10.1016/S0925-4005(01)00890-5.

(140) Anderson, A. M. *Experimental Methods for Engineers*; 1994; Vol. 9. https://doi.org/10.1016/0894-1777(94)90118-X.

(141) Astrath, N. G. C.; Shen, J.; Song, D.; Rohling, J. H.; Astrath, F. B. G.; Zhou, J.; Navessin, T.; Liu, Z. S. S.; Gu, C. E.; Zhao, X. The Effect of Relative Humidity on Binary Gas Diffusion. *J. Phys. Chem. B* **2009**, *113* (6), 8369–8374. https://doi.org/10.1021/jp900796w.

(142) Zhao, J.; Shahgaldi, S.; Alaefour, I.; Xu, Q.; Li, X. Gas Permeability of Catalyzed Electrodes in Polymer Electrolyte Membrane Fuel Cells. *Appl. Energy* **2018**, *209*, 203–210. https://doi.org/10.1016/j.apenergy.2017.10.087.

(143) Wicke, E.; Kallenbach, R. Die Oberflächendiffusion von Kohlendioxyd in Aktiven Kohlen. *Kolloid-Z.* **1941**, *97* (2), 135–151. https://doi.org/10.1007/BF01502640.

(144) Li, X.; Forouzandeh, F.; Kakanat, A. J.; Feng, F.; Banham, D. W. H.; Ye, S.; Kwok, D. Y.; Birss, V. Surface Characteristics of Microporous and Mesoporous Carbons Functionalized with Pentafluorophenyl Groups. *ACS Appl. Mater. Interfaces* **2018**, *10* (2), 2130–2142. https://doi.org/10.1021/acsami.7b13880.

(145) Crank, J. *The Mathematics of Diffusion*, 2nd ed.; Oxford University Press, 1975. https://doi.org/10.1016/0306-4549(77)90072-X.

(146) Shen, L.; Chen, Z. Critical Review of the Impact of Tortuosity on Diffusion. *Chem. Eng. Sci.* **2007**, *62* (14), 3748–3755. https://doi.org/10.1016/j.ces.2007.03.041.

(147) Rashapov, R. R.; Unno, J.; Gostick, J. T. Characterization of PEMFC Gas Diffusion Layer Porosity. *J. Electrochem. Soc.* **2015**, *162* (6), F603–F612. https://doi.org/10.1149/2.0921506jes.

(148) Bruggeman, D. A. G. Berechnung Verschiedener Physikalischer Konstanten von Heterogenen Substanzen. I. Dielektrizitätskonstanten Und Leitfähigkeiten Der Mischkörper Aus Isotropen Substanzen. *Ann. Phys.* **1935**, *416* (7), 636–664. https://doi.org/10.1002/andp.19354160705.

(149) Neale, G. H.; Nader, W. K. Prediction of Transport Processes within Porous Media: Diffusive Flow Processes within an Homogeneous Swarm of Spherical Particles. *AIChE J.* **1973**, *19* (1), 112–119. https://doi.org/10.1002/aic.690190116.

(150) Weber, A. Z.; Newman, J. *Modeling Transport in Polymer-Electrolyte Fuel Cells*; 2004; Vol. 104. https://doi.org/10.1021/cr020729l.

(151) Tjaden, B.; Cooper, S. J.; Brett, D. J.; Kramer, D.; Shearing, P. R. On the Origin and Application of the Bruggeman Correlation for Analysing Transport Phenomena in Electrochemical Systems. *Curr. Opin. Chem. Eng.* **2016**, *12*, 44–51. https://doi.org/10.1016/j.coche.2016.02.006.

(152) Hoogschagen, J. Diffusion in Porous Catalysts and Adsorbents. *Ind. Eng. Chem.* **1955**, *47* (5), 906–912. https://doi.org/10.1021/ie50545a016.

(153) Currie, J. A. Gaseous Diffusion in Porous Media .2. Dry Granular Materials. *Br. J. Appl. Phys.* **1960**, *11* (8), 318–324. https://doi.org/Doi 10.1088/0508-3443/11/8/303.

(154) Ebner, M.; Chung, D. W.; García, R. E.; Wood, V. Tortuosity Anisotropy in Lithium-Ion Battery Electrodes. *Adv. Energy Mater.* **2014**, *4* (5), 1–6. https://doi.org/10.1002/aenm.201301278.

(155) Penman, H. L. Gas and Vapour Movements in the Soil: I. The Diffusion of Vapours through Porous Solids. *J. Agric. Sci.* **1940**, *30* (03), 437. https://doi.org/10.1017/S0021859600048164.

(156) Wilson, A.; Kleen, G.; Papageorgopoulo, D. DOE Hydrogen and Fuel Cells Program Record (2017) - Record # 17007. Department of Energy (DOE) September 30, 2017.

(157) Jahnke, H.; Schönborn, M.; Zimmermann, G. Organic Dyestuffs as Catalysts for Fuel

Cells. In *Physical and Chemical Applications of Dyestuffs*; Schäfer, F. P., Gerischer, H., Willig, F., Meier, H., Jahnke, H., Schönborn, M., Zimmermann, G., Eds.; Topics in Current Chemistry; Springer-Verlag: Berlin/Heidelberg, 1976; Vol. 61, pp 133–181. https://doi.org/10.1007/BFb0046059.

(158) Serov, A.; Shum, A. D.; Xiao, X.; De Andrade, V.; Artyushkova, K.; Zenyuk, I. V.; Atanassov, P. Nano-Structured Platinum Group Metal-Free Catalysts and Their Integration in Fuel Cell Electrode Architectures. *Appl. Catal. B Environ.* **2018**, *237*, 1139–1147. https://doi.org/10.1016/j.apcatb.2017.08.067.

(159) Li, J.; Brüller, S.; Sabarirajan, D. C.; Ranjbar-Sahraie, N.; Sougrati, M. T.; Cavaliere, S.; Jones, D.; Zenyuk, I. V.; Zitolo, A.; Jaouen, F. Designing the 3D Architecture of PGM-Free Cathodes for H_2/Air Proton Exchange Membrane Fuel Cells. *ACS Appl. Energy Mater.* **2019**, *2* (10), 7211–7222. https://doi.org/10.1021/acsaem.9b01181.

(160) Shukla, S.; Wei, F.; Mandal, M.; Zhou, J.; Saha, M. S.; Stumper, J.; Secanell, M. Determination of PEFC Gas Diffusion Layer and Catalyst Layer Porosity Utilizing Archimedes Principle. *J. Electrochem. Soc.* **2019**, *166* (15), F1142–F1147. https://doi.org/10.1149/2.0251915jes.

(161) Yu, Z.; Carter, R. N.; Zhang, J. Measurements of Pore Size Distribution, Porosity, Effective Oxygen Diffusivity, and Tortuosity of PEM Fuel Cell Electrodes. *Fuel Cells* **2012**, *12* (4), 557–565. https://doi.org/10.1002/fuce.201200017.

(162) Rashapov, R.; Imami, F.; Gostick, J. T. A Method for Measuring In-Plane Effective Diffusivity in Thin Porous Media. *Int. J. Heat Mass Transf.* **2015**, *85*, 367–374. https://doi.org/10.1016/j.ijheatmasstransfer.2015.01.101.

(163) Tranter, T. G.; Stogornyuk, P.; Gostick, J. T.; Burns, A. D.; Gale, W. F. A Method for Measuring Relative In-Plane Diffusivity of Thin and Partially Saturated Porous Media: An Application to Fuel Cell Gas Diffusion Layers. *Int. J. Heat Mass Transf.* **2017**, *110*, 132–141. https://doi.org/10.1016/j.ijheatmasstransfer.2017.02.096.

(164) Baricci, A.; Bisello, A.; Serov, A.; Odgaard, M.; Atanassov, P.; Casalegno, A. Analysis of the Effect of Catalyst Layer Thickness on the Performance and Durability of Platinum Group Metal-Free Catalysts for Polymer Electrolyte Membrane Fuel Cells. *Sustain. Energy Fuels* **2019**, *3* (12), 3375–3386. https://doi.org/10.1039/C9SE00252A.

(165) Yu, Z.; Carter, R. N. Measurement of Effective Oxygen Diffusivity in Electrodes for Proton Exchange Membrane Fuel Cells. *J. Power Sources* **2010**, *195* (4), 1079–1084. https://doi.org/10.1016/j.jpowsour.2009.08.065.

(166) Zook, L. A.; Leddy, J. Density and Solubility of Nafion: Recast, Annealed, and Commercial Films. *Anal. Chem.* **1996**, *68* (21), 3793–3796. https://doi.org/10.1021/ac960604e.

(167) Weber, A. Z.; Borup, R. L.; Darling, R. M.; Das, P. K.; Dursch, T. J.; Gu, W.; Harvey, D.; Kusoglu, A.; Litster, S.; Mench, M. M.; Mukundan, R.; Owejan, J. P.; Pharoah, J. G.; Secanell, M.; Zenyuk, I. V. A Critical Review of Modeling Transport Phenomena in Polymer-Electrolyte Fuel Cells. *J. Electrochem. Soc.* **2014**, *161* (12), F1254–F1299. https://doi.org/10.1149/2.0751412jes.

(168) Zhao, J.; Shahgaldi, S.; Alaefour, I.; Yang, S.; Li, X. Pore Structure and Effective Diffusion Coefficient of Catalyzed Electrodes in Polymer Electrolyte Membrane Fuel Cells. *Int. J. Hydrog. Energy* **2018**, *43* (7), 3776–3785. https://doi.org/10.1016/j.ijhydene.2018.01.019.

(169) Soboleva, T.; Zhao, X.; Malek, K.; Xie, Z.; Navessin, T.; Holdcroft, S. On the Micro-,

Meso-, and Macroporous Structures of Polymer Electrolyte Membrane Fuel Cell Catalyst Layers. *ACS Appl. Mater. Interfaces* **2010**, *2* (2), 375–384. https://doi.org/10.1021/am900600y.

(170) Pant, L. M.; Mitra, S. K.; Secanell, M. Absolute Permeability and Knudsen Diffusivity Measurements in PEMFC Gas Diffusion Layers and Micro Porous Layers. *J. Power Sources* **2012**, *206*, 153–160. https://doi.org/10.1016/j.jpowsour.2012.01.099.

(171) Carrigy, N. B.; Pant, L. M.; Mitra, S.; Secanell, M. Knudsen Diffusivity and Permeability of PEMFC Microporous Coated Gas Diffusion Layers for Different Polytetrafluoroethylene Loadings. *J. Electrochem. Soc.* **2013**, *160* (2), F81–F89. https://doi.org/10.1149/2.036302jes.

(172) Mangal, P.; Pant, L. M.; Carrigy, N.; Dumontier, M.; Zingan, V.; Mitra, S.; Secanell, M. Experimental Study of Mass Transport in PEMFCs: Through Plane Permeability and Molecular Diffusivity in GDLs. *Electrochimica Acta* **2015**, *167*, 160–171. https://doi.org/10.1016/j.electacta.2015.03.100.

(173) Komini Babu, S.; Spernjak, D.; Mukundan, R.; Hussey, D. S.; Jacobson, D. L.; Chung, H. T.; Wu, G.; Steinbach, A. J.; Litster, S.; Borup, R. L.; Zelenay, P. Understanding Water Management in Platinum Group Metal-Free Electrodes Using Neutron Imaging. *J. Power Sources* **2020**, *472*, 228442. https://doi.org/10.1016/j.jpowsour.2020.228442.

(174) Choi, J.-Y.; Yang, L.; Kishimoto, T.; Fu, X.; Ye, S.; Chen, Z.; Banham, D. Is the Rapid Initial Performance Loss of Fe/N/C Non Precious Metal Catalysts Due to Micropore Flooding? *Energy Environ. Sci.* **2017**, *10* (1), 296–305. https://doi.org/10.1039/C6EE03005J.

(175) Martinez, U.; Komini Babu, S.; Holby, E. F.; Zelenay, P. Durability Challenges and Perspective in the Development of PGM-Free Electrocatalysts for the Oxygen Reduction Reaction. *Curr. Opin. Electrochem.* **2018**, *9*, 224–232. https://doi.org/10.1016/j.coelec.2018.04.010.

Appendix

Table A-1 Model parameters for gas diffusion layers (SGL25BC)

Parameter	Correlation/Value
Structural properties	
Thickness[59,115] $[\mu\mathrm{m}]$	190 (compressed) or 109 (uncompressed)
Porosity[59,116] $[-]$	0.882 (compressed) or 0.81 (uncompressed)
Gas transport	
Molecular diffusivity[65] $[\mathrm{cm}^2/\mathrm{s}]$	Chapman-Enskog
Effective diffusivity (through-plane)[117,118] $[\mathrm{cm}^2/\mathrm{s}]$	Tomadakis-Sotirchos correlation $\varepsilon_{v,TP}^{th} = 0.11$ (fixed) $\mu = 3.479$ (fitted)
Effective diffusivity (in-plane)[117,119] $[\mathrm{cm}^2/\mathrm{s}]$	Tomadakis-Sotirchos correlation $\varepsilon_{v,TP}^{th} = 0.11$ (fixed) $\mu = 2.579$ (fitted)
Electron transport	
Effective electrical conductivity (through-plane)[115] $[\mathrm{S/cm}]$	180
Effective electrical conductivity (in-plane)[115] $[\mathrm{S/cm}]$	3.75
Thermal transport	
Effective thermal conductivity (through-plane)[120,a,b] $[\mathrm{W/(cm \cdot K)}]$	$k_{TP}^{eff} = M(T_c)k_y^{eff}$ $M(T_c) = -1.495 \times 10^{-11}T_c^5 + 2.601 \times 10^{-9}T_c^4 - 6.116 \times 10^{-8}T_c^3 - 9.829 \times 10^{-6}T_c^2 + 8.754 \times 10^{-4}T_c + 0.0664$
Effective thermal conductivity (in-plane)[121,a,b] $[\mathrm{W/(cm \cdot K)}]$	$k_{IP}^{eff} = -7.166 \times 10^{-6}T_c^3 + 2.24 \times 10^{-3}T_c^2 - 0.237T_c + 20.1$

[a] $T_c[℃] = T[\mathrm{K}] - 273$

[b] $-50℃ \leq T_c \leq 120℃$ (through-plane), $-20℃ \leq T_c \leq 120℃$ (in-plane)

Table A-2 Model parameters for microporous layers (SGL25BC)

Parameter	Correlation/Value
Structural properties	
Thickness[115] [μm]	45
Porosity[115] [$-$]	0.40
Average pore radius[59] [nm]	56
Gas transport	
Molecular diffusivity[65] [$\mathrm{cm^2/s}$]	Chapman-Enskog
Knudsen diffusivity [$\mathrm{cm^2/s}$]	$D_{i,k} = \frac{d_p}{3}\sqrt{\frac{8RT}{\pi M_i}}$
Bulk diffusivity [$\mathrm{cm^2/s}$]	$\frac{1}{D_i} = \frac{1}{D_{i,j}} + \frac{1}{D_{i,k}}$
Effective diffusivity[122] [$\mathrm{cm^2/s}$]	Percolation equation $\varepsilon_v^{th} = 0.118$ $\mu = 2$
Electron transport	
Effective electron conductivity[115] [$\mathrm{S/cm}$]	0.823
Thermal transport	
Effective thermal conductivity[115] [$\mathrm{W/(cm \cdot K)}$]	0.005

Table A-3 Model parameters for polymer electrolyte membrane (NR-211)

Parameter	Correlation/Value
Thickness[123] [μm]	25
EW [$\mathrm{g/mol}$]	1100
Back-diffusion coefficient for water[124] [$\mathrm{cm^2/s}$]	$D_\lambda = \begin{cases} 3.10 \times 10^{-3}\lambda\left(-1 + e^{0.28\lambda}\right)e^{-2436/T} & \text{for } 0 < \lambda \leq 3 \\ 4.17 \times 10^{-3}\lambda\left(1 + 161e^{-\lambda}\right)e^{-2436/T} & \text{for } 3 < \lambda \leq 17 \end{cases}$
Electro-osmotic drag coefficient[125] [$\mathrm{mol_{H_2O}/mol_{H^+}}$]	$n_d = \frac{2.5\lambda}{22}$
Diffusion coefficient for thermal osmosis[126] [$\mathrm{g/(cm \cdot s \cdot K)}$]	$D_T = -1.04 \times 10^{-4} \exp\left(-\frac{2362}{T}\right)$
Proton conductivity[122] [$\mathrm{S/cm}$]	$\sigma_m = (-1.0125 \times 10^{-4}\lambda^2 + 0.01052\lambda - 0.020634)e^{\frac{6248}{R}\left(\frac{1}{303}-\frac{1}{T}\right)}$
Thermal conductivity[127,128] [$\mathrm{W/(cm \cdot K)}$]	0.0015

Table A-4 Model parameters for catalyst layer (anode = Pt/C, cathode = non-PGM)

Parameter	Correlation/Value	
	Anode	**Cathode**
Physical Constants		
Density of platinum[73], ρ_{Pt} [g/cm^3]	21.5	-
Density of carbon[59], ρ_C [g/cm^3]	1.25	-
Density of Fe-N/C, ρ_{FeNC} [g/cm^3]	-	2.326
Density of Nafion™[73], ρ_N [g/cm^3]	2.0	2.0
Primary particle radius[59], r_p [nm]	39.5	-
%Pt supported on carbon, y_{Pt} [$\%wt$]	0.46	-
Ionomer loading, y_N [$\%wt$]	0.30	Variable (0.10 – 0.90)
Structural properties		
Thickness, δ [μm]	4	Variable ($10-120\,\mu$m)
Solid phase fraction, ε_s [$-$]	$\varepsilon_s = \frac{m_{Pt}}{\delta}\left(\frac{1}{\rho_{Pt}} + \frac{1-y_{Pt}}{y_{Pt}\rho_C}\right)$	$\varepsilon_s = \frac{m_{FeNC}}{\delta}\frac{1}{\rho_{FeNC}}$
Ionomer phase fraction, ε_n [$-$]	$\varepsilon_n = \frac{m_{Pt}}{\delta}\frac{y_n}{(1-y_n)y_{Pt}\rho_n}$	$\varepsilon_N = \frac{m_{FeNC}}{\delta}\frac{y_N}{(1-y_n)\rho_n}$
Porosity, ε_v [$-$]	$\varepsilon_v = 1 - \varepsilon_s - \varepsilon_n$	
Average pore radius[59], r_k [nm]	$r_k = r_p(1.66\varepsilon_v^{1.65} + 0.289)$	300
Gas transport		
Molecular diffusivity, $D_{i,j}$ [cm^2/s]	Chapman-Enskog	
Knudsen diffusivity, $D_{i,k}$ [cm^2/s]	$D_{i,k} = \frac{d_p}{3}\sqrt{\frac{8RT}{\pi M_i}}$	
Bulk diffusivity, D_i [cm^2/s]	$\frac{1}{D_i} = \frac{1}{D_{i,j}} + \frac{1}{D_{i,k}}$	
Effective diffusivity[122], D_i^{eff} [cm^2/s]	Percolation equation $\varepsilon_v^{th} = 0.25884$ $\mu = 2$	Archie's law $m = 2.714$
Dissolved water transport		
Sorption isotherm[129], λ_{eq} $[\mathrm{mol}_{H_2O}/\mathrm{mol}_{SO}]$	$\lambda_{eq} = \left[1 + 0.2352a_w^2\left(\frac{T-303}{30}\right)\right](14.22a_w^3 - 18.92a_w^2 + 13.41a_w)$	
Effective diffusion coefficient of water through Nafion™[106,124] [cm^2/s]	$D_\lambda^{eff} = \varepsilon_n^{1.6}D_\lambda$	
Electro-osmotic drag coefficient[125] $[\mathrm{mol}_{\mathrm{H_2O}}/\mathrm{mol}_{H^+}]$	$n_d = \frac{2.5\lambda}{22}$	
Effective diffusion coefficient for thermal osmosis[106,126] [g/(cm · s · K)]	$D_T^{eff} = \varepsilon_n^{1.6}D_T$	
Proton transport		

Proton conductivity through Nafion™ thin film, [S/cm]	$\sigma_{m,thin} = (1.931 \times 10^{-7} a_w^3 - 6.735 \times 10^{-6} a_w^2 + 0.00075 a_w - 0.008) e^{\frac{6248}{R}\left(\frac{1}{353}-\frac{1}{T}\right)}$ where $a_w = \begin{cases} 100(0.000094\lambda^3 - 0.00865\lambda^2 + 0.1832\lambda - 0.1254) & \text{if } \lambda < 13 \\ 100 & \text{else} \end{cases}$	
Effective proton conductivity[106], [S/cm]	$\sigma_m^{eff} = \varepsilon_N^{1.6} \sigma_{m,thin}$	
Electron transport		
Electron conductivity[59], σ_s [S/cm]	88.84	
Effective electron conductivity, σ_s^{eff} [S/cm]	Percolation equation $\varepsilon_s^{th} = 0.118$ $\alpha = 2$	Percolation equation $\varepsilon_s^{th} = 0.05$ $\alpha = 2$
Thermal transport		
Effective thermal conductivity, k^{eff} [W/cm]	0.00334	
Kinetic parameters		
Thermodynamic potential, E [V]	0	1.20 (Nernst Equation)
Overpotential, η [V]	$\phi_s - \phi_m - E$	
α	-	0.6
n	-	4
γ[73]	1.2	1
Volumetric catalyst loading, V_{cat} [mg/cm^3]	400	Variable
Volume specific surface area of the catalyst layer, A_v [cm^2/cm^3]	1.2×10^5	Variable
j_{0T} [A/cm^2]	0.47[32,73]	-
j_{0H} [A/cm^2]	0.01[32,73]	-
i_0^{ref} [A/cm^2][109]	-	2.707×10^{-8}
c^{ref} [mol/cm^3] H_2 (anode)[108], O_2 (cathode)	0.59×10^{-6}	0.836×10^{-5}